January 28, 2021

STATUS REPORT OF THE ASACUSA EXPERIMENT

Progress in 2020 and plans for 2021

ASACUSA collaboration

C. Amsler[a], D. Barna[b], H. Breuker[c], S. Chesnevskaya[a], G. Costantini[d], R. Ferragut[e], M. Giammarchi[f], A. Gligorova[a], H. Higaki[g], M. Hori[h*], E. D. Hunter[a], Y. Kanai[i], V. Kletzl[a], V. Kraxberger[a], N. Kuroda[j], A. Lanz[a], M. Leali[d], V. Mäckel[a,c], G. Maero[k], C. Malbrunot[l], V. Mascagna[m], Y. Matsuda[j], S. Migliorati[d], D. J. Murtagh[a], Y. Nagata[n], A. Nanda[a], L. Nowak[l], E. Pasino[k], W. Pirkl[h], M. Romé[k], M. C. Simon[a], M. Tajima[i], V. Toso[e], S. Ulmer[c], U. Uggerhøj[o], L. Venturelli[d], A. Weiser[a], E. Widmann[a*], T. Wolz[l], Y. Yamazaki[c], J. Zmeskal[a]

[a]Stefan Meyer Institute, [b]Wigner Research Centre for Physics, [c]Ulmer Fundamental Symmetries Laboratory, RIKEN, [d]Dipartimento di Ingegneria dell'Informazione, Università degli Studi di Brescia, and INFN, [e]Politechnico di Milano, [f]INFN Milano, [g]Graduate School of Advanced Sciences of Matter, Hiroshima University, [h]Max-Planck-Institut für Quantenoptik, [i]Nishina Center for Accelerator-Based Science, RIKEN, [j]Institute of Physics, the University of Tokyo, [k]Dipartimento di Fisica, Università degli Studi di Milano and INFN Milano, [l]Experimental Physics Department, CERN, [m]Dipartimento di Scienza e Alta Tecnologia, Università degli Studi dell'Insubria and INFN, [n]Department of Physics, Tokyo University of Science, [o]Department of Physics and Astronomy, Aarhus University

* Co-spokespersons

CERN-SPSC-2021-003 / SPSC-SR-283
28/01/2021

Executive summary

In 2020 the ASACUSA antiprotonic helium group continued preparations for the upcoming 2021 beamtime. The equipment for two-photon laser spectroscopy of $\overline{p}$He which will be used for the initial phase of measurements is onsite and will be installed in the ASACUSA-1 beamline in the next months. The electron-cooled antiproton beam of ELENA is expected to allow an order of magnitude higher data accumulation rates and an improved signal-to-noise ratio compared to past experiments using the radiofrequency quadrupole decelerator. This together with a pump-probe detection method and advanced laser techniques should ultimately allow measurements of some weak $\overline{p}\mathrm{He}^+$ transitions with natural widths that are two orders of magnitude narrower than those studied previously. This would allow a similar level of improvement in the experimental precision. Our 2021 efforts will concentrate on tuning the new ELENA beamline and experiment to optimize the spectroscopic signals related to two-photon transitions of large amplitude.

The experiment compares the two-photon transition frequencies of $\overline{p}\mathrm{He}^+$ with the results of three-body QED calculations to determine the antiproton-to-electron mass ratio, limits on CPT-symmetry, and limits on any exotic forces that may arise in a hadron-antihadron bound system. This is complementary to antihydrogen experiments which probe an antilepton-antihadron system. The precision and sensitivity to exotic phenomena that may eventually be reached critically depend on three issues, i) achievement of high data accumulation rates and signal-to-noise ratios using the ELENA beam, ii) three-body QED calculations that are commensurate with the 10^{-11}-scale precision, and iii) the development of new laser and frequency reference techniques used to interrogate $\overline{p}\mathrm{He}^+$ which has a microsecond-scale lifetime.

One highlight of 2020 for our collaboration was the publication of the experimental results of laser spectroscopy of metastable pionic helium ($\pi\mathrm{He}^+$) which is the pionic analogue of $\overline{p}\mathrm{He}^+$. This measurement carried out at the 590 MeV Ring Cyclotron facility of Paul Scherrer Institute constitutes the first laser excitation and spectroscopy of an atom containing a meson. By further improving the precision in future experiments, the three-body QED calculation for an atom consisting of spin-0 particles that has no hyperfine structure and obeys the Klein-Gordon equation (instead of the Dirac equation as in the $\overline{p}\mathrm{He}^+$ atom) can be studied. The experiment will allow the determination of the negative pion mass and upper limits on exotic forces involving a meson. The experiment relied on technical support in terms of magnets and cryogenics provided by CERN between 2013 and 2014 which has been appreciated by PSI scientific groups.

In 2020, two experimental groups carried out spectroscopy of the three-body hydrogen deuteride molecular ion (HD^+). They compared the results with QED calculations that were similar to those of $\overline{p}\mathrm{He}^+$, and determined the proton-to-electron mass ratio M_p/m_e to a fractional precision of 2×10^{-11}. The results agree with the M_p/m_e value determined previously in Penning trap experiments. This implies that the same QED calculations used to evaluate HD^+ can be adapted to $\overline{p}\mathrm{He}^+$ to reach a similar level of precision. The M_p/m_e determination depended on several physical constants including the deuteron mass, and the charge radii of the constituent proton and deuteron which were used as input parameters in the QED calculations. Interestingly, a Penning trap group determined the deuteron mass in 2020 and found a 4.8 standard-deviation difference with the prior accepted value used in the HD^+ calculations. Measurements of the $\overline{p}\mathrm{He}^+$ transition frequencies may now be particularly important since they are sensitive to a separate set of physical constants including the mass of the helium nucleus, but not the deuteron mass. The sensitivity

of the $\overline{p}\mathrm{He}^+$ frequencies to nuclear charge radii-related effects is smaller than for HD^+ or atomic hydrogen.

Some external groups developed laser systems that are similar to the one used by ASACUSA and achieved precision in terms of an Allan deviation of at least 5×10^{-11}. This makes us confident that our experimental goals will be achieved, though many years of step-by-step efforts are necessary both at CERN and by external experimental and theoretical groups. The collaboration is also examining the possibilities of transmitting an ultrastable optical reference signal from the Swiss meteorological institute METAS located in Bern over the existing fiber infrastructure of SWITCHnet to CERN. We are eager to work with other AD collaborations regarding this exciting possibility.

For the antihydrogen group with a large number of collaborators from many different countries the pandemic presented an enormous challenge. CERN was shut down for some time, travel to CERN was not possible at all for collaborators from some countries, for others it was largely accompanied by 2-week quarantine periods before entering CERN. Some of the development was done at home institutions, although they also partly suffered from restrictions of laboratory occupancy and phases of home office. Nevertheless, this report shows substantial progress achieved in a difficult year.

For the antihydrogen hyperfine structure experiment the re-analysis of previous data on the principal quantum number distribution of antihydrogen formed showed slightly higher n-values than previously, reinforcing the need to increase the ground-state population at the formation stage by going to colder and denser positron plasmas, and to work on schemes to deexcite antihydrogen after formation.

Significant progress has been achieved towards the creation of colder plasmas of reproducible properties, development of an accurate technique to measure plasma temperatures has led to implementation of the SDREVC technique developed by ALPHA in the Cusp field with electrons, and evaporative cooling of positrons. The Cusp trap Multi Ring Electrode stack has been redesigned and rebuilt and is ready for installation, a new cold bore for the Cusp trap is under construction to lower the temperature of the electrodes, new electronics and filters are used to reduce the noise entering the electrodes. A proton source has been built and commissioned and will be transported to CERN in January, enabling matter mixing studies prior to the availability of antiproton beams. A new positron trap and accumulator are being built in order to remove a superconducting magnet with large consumption of liquid helium.

Collisional deexcitation of formed hydrogen will be tried during the matter mixing studies as it is easy to implement. Work is going on studying stimulated deexcitation using THz radiation and lasers with excited caesium and hydrogen beams, aiming at reaching a state where the technique can be tried with antihydrogen during the 2022 beam time. The polarized hydrogen beam at CERN could not be operated in 2020 and is restarting after several hardware problems were solved, measurements are planned in 2021 to further develop the in-beam hyperfine spectroscopy techniques and to perform some measurements of SME coefficients, an analogous experiment to measure the deuterium hyperfine structure is being prepared in Vienna.

Analysis of data taken of antiproton annihilations in several target foils with the aim of providing benchmark data for Monte Carlo codes is close to being finalized and will be submitted for publication soon.

Contents

I Antiprotonic Helium **1**

1 Introduction and summary of 2021 outlook **1**

2 Laser spectroscopy of pionic helium atoms published in 2020 **2**

3 Experimental and theoretical progress regarding spectroscopy of three-body systems to determine fundamental constants in 2020 **7**
3.1 HD^+ spectroscopy and Penning trap experiments . . . 7
3.2 High-precision theoretical calculations of $\overline{p}He^+$ . . . 9
3.3 Limits on exotic beyond-the-Standard Model forces . . . 10

4 ASACUSA publications **11**

5 Preparations for the 2021 beamtime **11**
5.1 Overview and candidate two-photon transitions in the first phase of ELENA experiments . . 11
5.2 Beam profile monitors for ELENA . . . 13
5.3 Simulation and layout of the beamline in the $\overline{p}He^+$ spectroscopy experiment . . . 15
5.4 Energy loss calculations of ELENA beam through BoPET foils . . . 16
5.5 Laser systems . . . 17
5.6 Optical reference signals from metrological institutions to CERN . . . 18

II Antihydrogen **21**

6 Introduction **21**

7 Principal quantum number distribution of formed antihydrogen **22**

8 Towards in-beam hyperfine spectroscopy of antihydrogen **22**
8.1 Experimental Results and hardware upgrades in 2020 . . . 23
8.1.1 Plasma Temperature . . . 23
8.1.2 SDREVC . . . 25
8.1.3 Positron Results . . . 28
8.1.4 Experiments with Positive Ions . . . 30
8.1.5 Development of a low energy proton source . . . 33
8.2 Future upgrades and work in progress . . . 36
8.2.1 New Cusp Multiringed Electrode Trap . . . 36
8.2.2 Double Internal Field Ionizer . . . 37
8.2.3 Plasma detector upgrade . . . 37
8.2.4 Cold Bore Replacement . . . 39
8.2.5 Positron Trap Upgrades . . . 41
8.2.6 Upgrades to the MUSASHI antiproton trap and preparations for beam from ELENA . 44
8.2.7 Upgrade of the scintillating bar detector . . . 45
8.2.8 Schedule for 2021 . . . 45
8.3 Antihydrogen beam deexcitation schemes . . . 47
8.3.1 Collisional deexcitation of Rydberg states . . . 47
8.3.2 Stimulated deexcitation of Rydberg states . . . 47

9 Experiments with hydrogen and deuterium beams **48**
9.1 Progress at the excited hydrogen experiment 48
9.2 Progress at the hydrogen HFS-experiment 51
9.3 Progress at the deuterium HFS-experiments and Ramsey spectroscopy 53
9.4 Timeline for the hydrogen and deuterium experiments in 2021 55

10 Fragmentation studies of antiproton-nucleus annihilation at rest **56**
10.1 Preliminary results 56

References **59**

Part I
Antiprotonic Helium

1 Introduction and summary of 2021 outlook

The antiprotonic helium ($\overline{p}\mathrm{He}^+$) atom is a three-body system composed of a helium nucleus, an electron in the 1s state, and an antiproton in a Rydberg state with large principle and angular momentum quantum numbers ($n \approx \ell + 1 \approx 38$). It is a hadron-antihadron quantum bound system having the longest known lifetime. The collaboration proposed in 2019 to use the electron-cooled beam provided by ELENA [1] to carry out sub-Doppler two photon laser spectroscopy [2, 3] of $\overline{p}\mathrm{He}^+$ resonances with small natural widths [4–15]. The experimental precision may ultimately, after many years of iterative efforts, reach a level that is two orders of magnitude higher than the experiments carried out previously by ASACUSA using the radiofrequency quadrupole decelerator (RFQD) to slow down the antiprotons [3, 16, 17]. Such a measurement would provide,

1. A test of three-body quantum electrodynamics (QED) calculations at $\approx 10^{-11}$ scale precision which may be compared with experiments on hydrogen molecular ions (H_2^+) or hydrogen deuteride molecular ions (HD^+). In 2020, two experimental groups published measurements on the HD^+ rotational and rovibrational transition frequencies with greatly improved precision compared to before [18, 19]. Intensive theoretical work on $\overline{p}\mathrm{He}^+$ and HD^+ was continued in 2019–2020 [10, 20] that would allow comparisons with experiments at relative precision of $\approx 10^{-11}$. Laser systems have recently been developed by several groups [21–26], some of which are commensurate with the precision required to improve the $\overline{p}\mathrm{He}^+$ experiment.

2. A determination of the antiproton-to-electron mass ratio to $\approx 10^{-11}$-scale precision [3, 16] which would improve the current value published by the collaboration,

$$M_{\overline{p}}/m_e = 1836.1526734(15). \tag{1}$$

   This result can then be compared with the proton-to-electron mass ratio determined by laser spectroscopy of HD^+ ions in 2020 [18, 19, 27] and by recent Penning trap experiments [28, 29]. The HD^+ experiments are sensitive to different physical quantities compared to $\overline{p}\mathrm{He}^+$, such as the deuteron mass [30, 31] and the proton and deuteron charge radii [32–36]. Several experimental results regarding these quantities were published in 2019–2020.

3. A consistency test of CPT symmetry in a bound hadron-antihadron system which is complementary to the studies carried out by other AD experiments regarding a antilepton-antihadron system (i.e., antihydrogen) or a single antiproton [37–42].

4. Upper limits on fifth forces at Angstrom-length scales [43–45] for which several groups have published new experimental and theoretical studies in 2019–2020 [18, 46, 47].

5. Limits on beyond-the-Standard-Model velocity and spin-dependent, semi-leptonic forces that may arise between antihadrons and electrons [7, 48, 49] due to axions or other undiscovered spin-0 or spin-1 bosons such as familons, Majorons, or arions.

6. Studies on the electromagnetic cascade of $\overline{p}\mathrm{He}^+$ [15, 50–58]. Several exotic effects in antiprotonic helium have been theoretically studied and published in 2019–2020 [8, 9, 11, 12].

7. Comparisons with the results of laser spectroscopy experiments on metastable pionic helium ($\pi^4\mathrm{He}^+ \equiv \pi^- + {}^4\mathrm{He}^{2+} + e^-$) atoms [59–66] which were published by the collaboration in 2020 [67]. The $\pi^4\mathrm{He}^+$ constitutes a pionic analogue of $\overline{p}^4\mathrm{He}^+$ and allows us to study the applicability and precision of the QED calculations on atoms that contain spin-0 particles that have a larger coupling to the electronic continuum compared to $\overline{p}^4\mathrm{He}^+$.

The collaboration benefits from the above-mentioned works of U.S., Chinese, European, and Russian theoretical and experimental groups in advancing the physics goals of our 2018 proposal. We have also submitted several experimental results to scientific journals.

In 2021, the collaboration intends to concentrate on the observation of intense two-photon resonances using the ELENA beam. The equipment is prepared and will be installed in the DE1 beam area in the coming months. A critical issue which determines the quality of the experimental data is the focusing of the beam into our experimental target in a way that best exploits its small energy spread and emittance. The beam profile monitors of the ELENA beamlines which were provided by our collaboration and installed and operated by CERN, are crucial for these efforts. Some recent measurements of H^- ions recorded by the ELENA operation team using the monitors are described in later sections of this report.

2019–2020 saw much theoretical progress towards calculating the $\overline{p}\mathrm{He}^+$ transition frequencies to higher precision, as well as experimental results regarding the related metastable $\pi^4\mathrm{He}^+$ atom and HD^+ ion. In this report we first highlight these new physics results, as the experimental setup which will be used for the 2021 measurements has been described in previous reports.

2 Laser spectroscopy of pionic helium atoms published in 2020

In 2020 the collaboration published the results of laser spectroscopy of metastable pionic helium atoms [64,67]. This work carried out at the PiE5 beamline of the 590 MeV Ring Cyclotron facility of Paul Scherrer Institute constituted the first laser excitation and spectroscopy of an atom containing a meson. The $\pi^4\mathrm{He}^+$ atom is the pionic analogue of $\overline{p}\mathrm{He}^+$, being a three-body atom composed of a helium nucleus, an ground-state electron, and a negatively-charged pion occupying a state of $n \approx \ell + 1 \approx 17$. Laser spectroscopy of $\pi^4\mathrm{He}^+$ is far more difficult than for the antiprotonic counterpart because of the extremely short lifetime of the exotic atom which provides little time to interact with the resonant laser beam, the lack of cooled and slow π^- beams, and the high levels of electron and muon contamination in the beam. The experiment was based on techniques developed over many years as reported in previous annual reports, and the technical assistance of the CERN magnet, cryogenic, and scintillator workshop specialists. The cryogenic target and scintillator counter array used in the experiment was developed at CERN within the framework of the ASACUSA collaboration. In this section we briefly review the results published in 2020.

The theoretical features of this three-body atom measured at PSI are significantly different compared to $\overline{p}\mathrm{He}^+$ studied in AD and ELENA. Most notably the atomic structure of $\pi^4\mathrm{He}^+$ contains no hyperfine structure as both the π^- and ${}^4\mathrm{He}$ nucleus are spin-0 particles [68, 69]. By comparing the experimental transition frequencies with the results of three-body QED calculations, the π^- mass [70–72] can be determined with a high precision as in the $\overline{p}\mathrm{He}^+$ case. This can contribute to establishing upper limits on laboratory constraints on the muon antineutrino mass [73]. Some upper limits may also be set on exotic forces involving π^-, as has been done for $\overline{p}\mathrm{He}^+$ mentioned earlier [7, 18, 43–49].

The atoms are produced via the reaction, $\pi^- + \mathrm{He} \rightarrow \pi\mathrm{He}^+ + e^-$ that occurs when π^- are allowed to come to rest in a helium target. The nanosecond-scale lifetime of $\pi\mathrm{He}^+$ arises because the π^- orbitals have negligible overlap with the nucleus, whereas the electromagnetic cascade

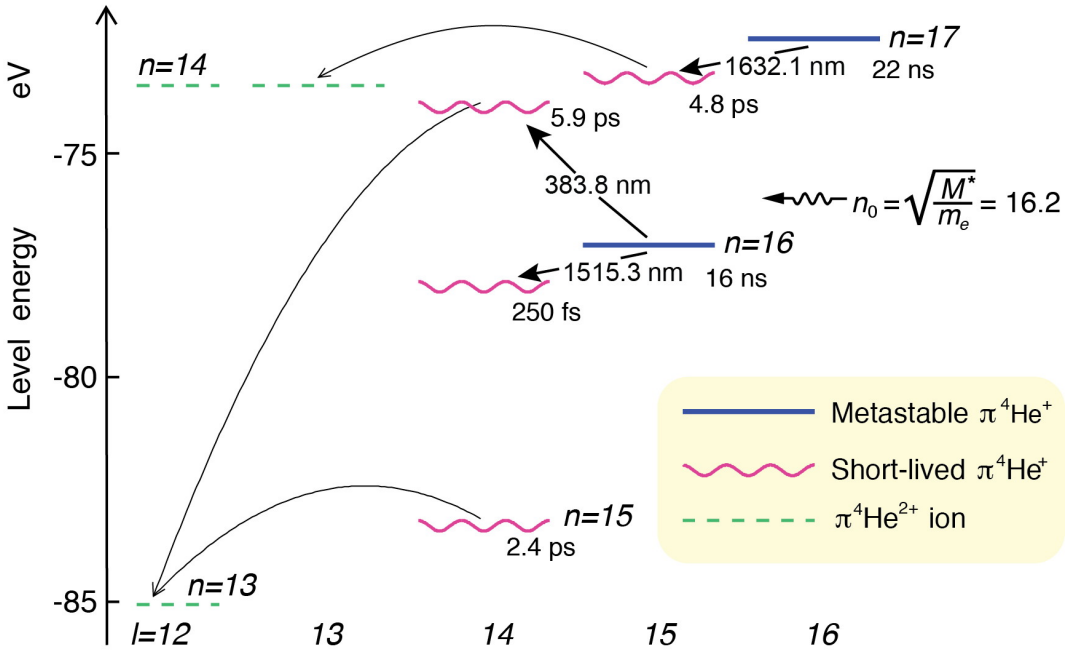

Figure 1 – Energy level diagram of $\pi^4\mathrm{He}^+$ atom. Theoretical absolute energy of the states (n, ℓ) are plotted relative to the three-body-breakup threshold. The wavy lines indicate Auger-dominated states with picosecond-scale lifetimes (indicated), solid lines the metastable levels with > 10 ns lifetimes. The dashed lines show the $\pi^4\mathrm{He}^{2+}$ ionic states formed after Auger electron emission. The curved arrows indicate the Auger transitions with minimum $|\Delta\ell_A|$. The laser transitions that were searched for are indicated by arrows with the resonance wavelengths shown in nanometers. From Ref. [67].

processes that normally deexcite the π^- within a picosecond such as radiative and Auger decays are suppressed. In fact the orbital π^- would typically decay into a π^- and electron much before any fluorescent photon could be emitted. The existence of $\pi\mathrm{He}^+$ has therefore been indirectly inferred from experiments [59–61, 74, 75] that began by using beams produced by synchrocyclotrons [76, 77] and liquid helium bubble chambers [78] which functioned as both the experimental target and detector. The experiments indicated that a fraction of π^- retain a lifetime that was variously estimated to be between 300 ps and 7 ns. Theoretical calculations on the decay rates differed from each other by 1–2 orders of magnitude so that quantitative comparisons with experiment were difficult [63, 64, 79]. Experimental studies instead concentrated on the two-body (rather than three-body) pionic helium ion ($\pi^4\mathrm{He}^{2+} \equiv \pi^- + {}^4\mathrm{He}^{2+}$) [80–82]. In particular the transitions between the short-lived ionic states near the 1s ground state could be studied by X-ray fluorescence spectroscopy despite the picosecond-scale lifetime of the ion.

In the experiment, we used sub-nanosecond laser pulses to excite a transition from a $\pi^4\mathrm{He}^+$ state with a nanosecond-scale lifetime, to a state with a picosecond-scale lifetime against Auger decay [64]. The $\pi^4\mathrm{He}^{2+}$ ion that formed after Auger emission of the 1s electron was promptly destroyed in atomic collisions that caused Stark mixing between the Rydberg and low ℓ orbitals [81, 83]. The resonance condition between the $\pi^4\mathrm{He}^+$ atom and the laser beam was detected as a peak in the rate of neutrons, protons, and deuterons that emerged from the resulting nuclear absorption [64, 75]. The backgrounds caused by prompt nuclear absorption of π^- was up to 10^4 times larger than this

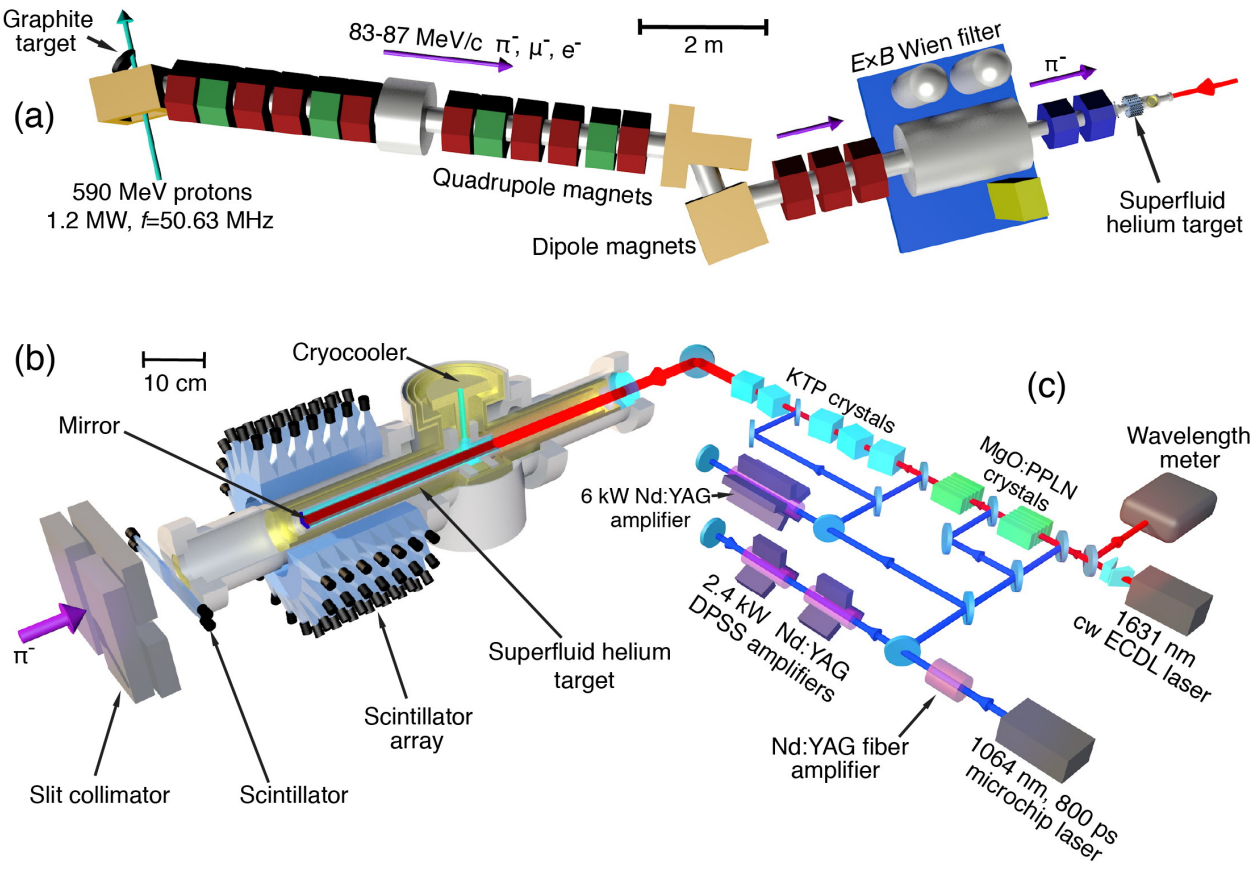

Figure 2 – (a): Layout of the π^- breamline at PSI. A quadrupole magnet was provided by CERN. (b) Layout of the experimental target. The π^- beam traverses a segmented scintillation counter before coming to rest in the helium target. The resulting $\pi^4\mathrm{He}^+$ atoms are irradiated with $\Delta t = 800$ ps long laser pulses with energy $E = 10$ mJ and wavelength $\lambda \approx 1631$ nm. The proton, neutron, and deuteron fragments that emerge from the π^- absorption in the helium nuclei are detected by 140 plastic scintillation counters surrounding the target. (b): Schematic layout of the laser system, see text. From [67].

signal.

This experiment used the πE5 beamline [84] which produced a π^- beam of momentum between 83 and 87 MeV/c and average intensity $N_\pi = (2-3) \times 10^7$ s^{-1}. A Wien filter diverted most of the contaminant e^- of rate $> 3 \times 10^9$ s^{-1} in the beam towards the steel blades of a slit collimator. The CERN magnet group provided a pair of quadrupole magnets from the storage area near the Proton Synchrotron. This device was transported to CERN and used to focus the purified π^- beam into an elliptical spot. The beam traversed a plastic scintillator plate that was segmented into four sections and then entered the helium target.

The contour plot of Fig. 3(a) shows the correlations of arrival times t_a and the energy depositions ΔE of particle traversals on the incident scintillator plates. The π^- arrived in bursts spaced by intervals $\Delta t = 19.75$ ns which arose from the $f_a = 50.63$ MHz radiofrequency of the cyclotron. The π^- events that were located in the rectangular area indicated by broken lines in the contour plot were distinguished from the residual μ^- and e^- by the time-of-flight and ΔE value for π^-.

About 2.3% of the π^- that came to rest in the target (Fig. 2 (a)) were assumed [75] to form

the metastable atoms. This target was developed within the infrastructure of the ASACUSA collaboration at CERN. A laser beam of diameter $d = 25$ mm, energy $E = 10$ mJ, pulse length $\Delta t = 800$ ps, repetition rate $f_r = 80.1$ Hz and wavelength $\lambda \approx 1631$ nm entered the target chamber. The implied production rate of the atoms of $> 3 \times 10^5$ s^{-1} ensured a 10^{-3} scale probability of coincidence for a laser pulse to irradiate a $\pi^4\mathrm{He}^+$ atom in the target.

The neutrons, and protons or deuterons that emerged from a π^- nuclear absorption tended to follow anticollinear [64, 85, 86] trajectories with a kinetic energy of a few tens of MeV. The fission products' arrival times t_a and energy depositions ΔE were measured (Fig. 3 (b)) using an array of 140 plastic scintillation counters, while most of the background e^- that arose from either the particle beam or from μ^- decays were removed as their energy deposition was small. The signal waveform [87–89] was recorded with sampling rates $f = 3.06$ Gs·s^{-1} using a custom readout system using the DRS4 application-specific integrated circuit (ASIC) based on switched capacitor arrays [90, 91].

The electronics developed by us was also used in an experiment to determine upper limits on the annihilation cross sections of antiprotons of kinetic energy $E \approx 125$ keV on thin target foils [88,92]. The results were compared with the cross sections measured at higher antiproton energies $E = 5.3$ MeV [93, 94].

A $t_a - \Delta E$ contour plot of hits on the scintillator array is shown in Fig. 3 (b). We removed most of the background e^- and fission products with low velocities and fission products with low velocities by selecting the events located in the area indicated by broken lines. The time spectrum of Fig. 3 (c) shows the distribution of accepted events measured without laser irradiation. The RF-driven consecutive arrivals of π^- produced peaks at $t = 0$ and 19.75 ns containing the $> 97\%$ of events involving the prompt nuclear absorption of π^-. The remaining $(2.1 \pm 0.7)\%$ fraction of π^- constituted a continuous spectrum that decayed with a lifetime $\tau = 7 \pm 2$ ns in the intervals between the π^- arrival peaks. This roughly agreed with the results of a Monte Carlo simulation [64] as well as with a previous experiment [75] carried out using a liquid helium target.

The laser pulses irradiated the target at a time $t = 9$ ns after the arrival of π^- with a typical timing jitter $\Delta t \leq 1$ ns. The laser pulses were produced by an injection-seeded, optical parameteric generator (indicated as OPG in Fig. 2(b)) and amplifier (OPA) laser system. We constructed a diode-pumped solid state (DPSS) neodymium-doped yttrium aluminium garnet (Nd:YAG) laser of single pass design which was precisely fired in synchronization with the RF of the cyclotron to pump the OPG-OPA laser. The OPG-OPA laser system was based on a continuous-wave (cw) external-cavity diode laser (ECDL) with wavelength $\lambda \approx 1631$ nm, the output of which was amplified by magnesium oxide doped periodically-polled lithium niobate (MgO:PPLN) crystals and potassium titanyl phosphate (KTP) crystals. The linewidth of the narrowband component of the laser beam was of order ≈ 10 GHz.

Besides two other resonances which we did not detect, we searched for the transition $(n, \ell) = (17, 16) \rightarrow (17, 15)$. The time spectrum indicated by filled circles in Fig. 3 (c) represents 2.5×10^7 π^- arrivals with the laser wavelength tuned to $\lambda \sim 1631.4$ nm. We observed a peak at $t = 9$ ns containing 300 events with a signal-to-noise ratio of 4 and a statistical significance of > 7 standard deviations. Our measured detection rate of 3 h^{-1} resonant $\pi^4\mathrm{He}^+$ events is roughly compatible with the production rate $> 3 \times 10^5$ s^{-1} of the atoms and Monte Carlo simulations [64] that assume that most of the metastable population lies in the state $(17, 16)$. When the laser was detuned off the resonance frequency (Fig. 4 (a)-(d)), the signal decreased and disappeared.

The intensity of the resonance signal (Fig. 4(a)–(d)) was determined by taking the difference between normalized time spectra measured with and without laser irradiation, and counting the events under the laser-induced peak at $t = 9$ ns. The resonance profile shown in Fig. 4(e) was obtained by scanning the laser frequency, with each data point representing data collected over a

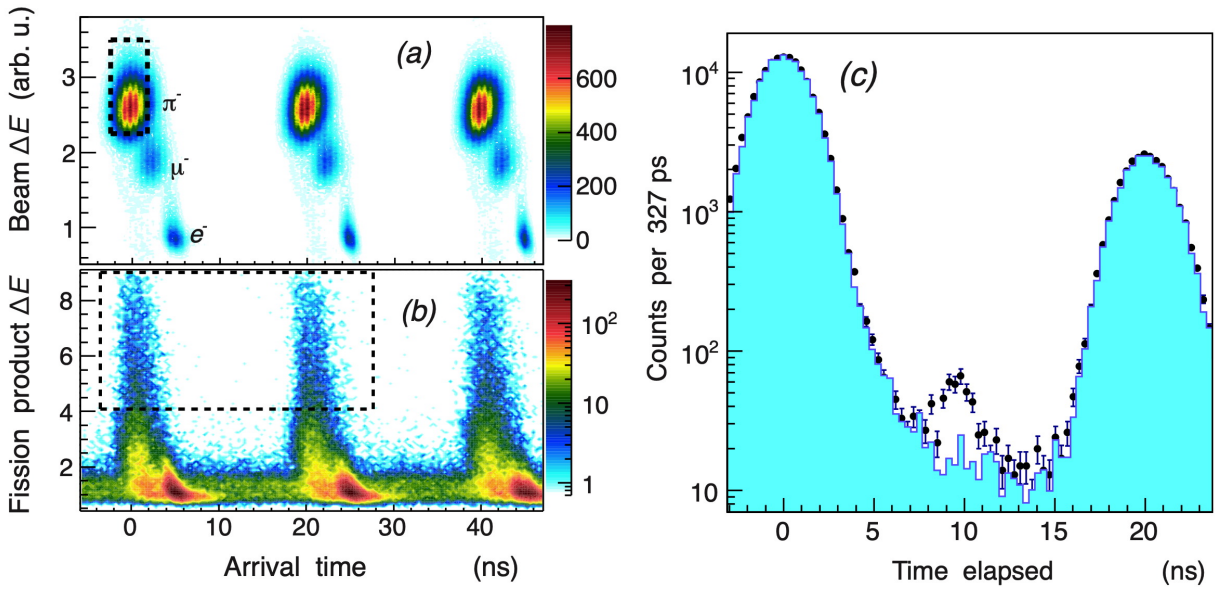

Figure 3 – (a): Contour plot showing the correlation between the arrival times t_a and energy depositions ΔE of particles measured by a scintillation counter placed at the target entrance. The particle type was identified and the π^- events in the rectangular region indicated by broken lines were selected. (b): The $t_a - \Delta E$ plot of fission fragments that strike the scintillator array following π^- absorption. Background e^- of $\Delta E < 20-25$ MeV were removed by accepting the events in the region indicated by the rectangle. (c): Time spectra of nuclear fragments measured with (indicated by filled circles with error bars) and without (blue filled histogram) laser irradiation at $t = 9$ ns. The peak in the former spectrum at $t = 9$ ns corresponds to the resonance signal of $(17, 16) \rightarrow (17, 15)$. From [67].

20–30 h period. The vertical error bars indicate the statistical uncertainty caused by the finite numbers of these resonant $\pi^4\mathrm{He}^+$ events. The ~ 100 GHz resonance width is commensurate with a convolution of the Auger width $\Gamma_A = 33$ GHz [64] of state $(17, 15)$, collisional [66] and power broadening (~ 50 GHz) effects, and the linewidth (~ 10 GHz) of the narrowband component of the laser pulses. Additional broadening may be caused by atomic collisions that shorten [50, 65, 95] the lifetime of the state $(17, 15)$. The 3.0 GHz spacing [14, 64] between the fine structure sublines that arise from the interaction between the electron spin and the orbital angular momentum of π^- cannot be resolved as it is much smaller than the 33 GHz natural width of the resonance. The best fit (see blue curve) of two overlapping Lorentzian functions which take these sublines into account had a reduced χ^2 value of 1.0. The resonance centroid is $\nu_{\mathrm{exp}} = 183760(6)(6)$ GHz. Here the statistical uncertainty (6 GHz) arises from the finite number of detected $\pi^4\mathrm{He}^+$ atoms, whereas the systematic uncertainty (6 GHz) are related to the selection of the fit function (5 GHz) and the calibration of the laser frequency. This ν_{exp} value is larger than the value [64] $\nu_{\mathrm{th}} = (183681.8 \pm 0.5)$ GHz calculated by theory by $\Delta\nu = (78 \pm 8)$ GHz. This is difference is believed to be due to atomic collisions that shift the resonance frequency [66], as similar effects have been observed [50, 96] for some $\overline{p}\mathrm{He}^+$ resonances at CERN. The gradient of this shift at temperature $T = 4$ K was calculated to be $d\nu/d\rho = (4.4 - 6.5) \times 10^{-21}$ GHz·cm^3 using the impact approximation of the binary collision theory of spectral lineshapes [66]. At the superfluid target density $\rho = 2.18 \times 10^{22}$ cm^{-3} used in these experiments, the expected blueshift corresponds to between $\Delta\nu = 96$ and 142 GHz. This roughly agrees with the experimental result.

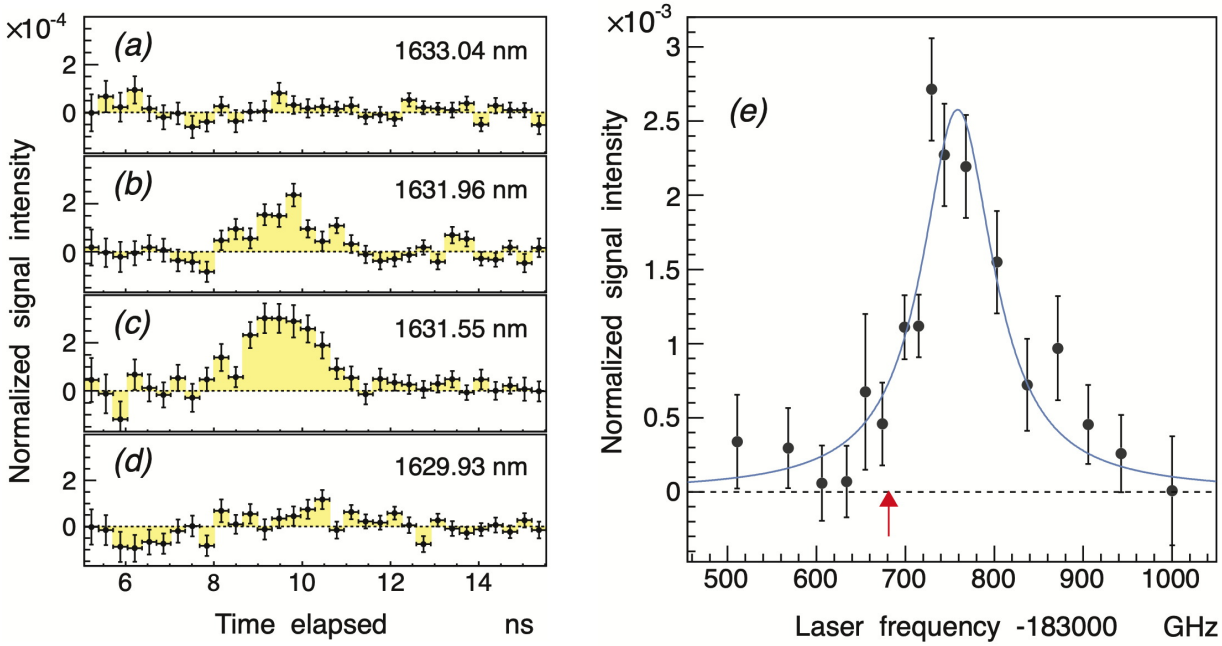

Figure 4 – (a)–(d): Normalized time spectra of the resonance signal of the transition $(n, l) = (17, 16) \rightarrow (17, 15)$ measured at four laser wavelengths obtained by taking the difference between the timing distributions of π^- absorption measured with and without the laser irradiation. (e): Profile of the resonance measured by scanning the laser frequency over a 500 GHz wide region and plotting the normalized counts under the peaks. From [67].

3 Experimental and theoretical progress regarding spectroscopy of three-body systems to determine fundamental constants in 2020

3.1 HD^+ spectroscopy and Penning trap experiments

In our experiment, the measured transition frequencies of $\overline{p}\mathrm{He}^+$ are compared with three-body QED calculations to determine the antiproton-to-electron mass ratio. This derivation critically depends on the precision of the calculations, but until recently there was no independent way of verifying this at a level of $\leq 10^{-10}$.

In 2020 two experimental groups published results on spectroscopy of HD^+ ions that were confined in a radiofrequency Paul trap. The Düsseldorf-based collaboration measured a fundamental rotational transition $(\nu, N) = (0, 0) \rightarrow (\nu, N') = (0, 1)$ in which ν and N denote the vibrational and rotational quantum numbers. The Amsterdam-Paris-Dubna experiment measured the rovibrational two-photon transition $(\nu, L) : (0, 3) \rightarrow (4, 2) \rightarrow (9, 3)$. By comparing the results with the same series of three-body calculations as $\overline{p}\mathrm{He}^+$, the Düsseldorf-based collaboration [18] determined the proton-to-electron mass ratio as,

$$M_p/m_e = 1836.152673449(24)_{\mathrm{exp}}(25)_{\mathrm{theor}}(13)_{\mathrm{CODATA2018,\ Fink-Myers}}. \quad (2)$$

The Amsterdam experiment [19] derived a ratio,

$$M_p/m_e = 1836.152673406(38). \quad (3)$$

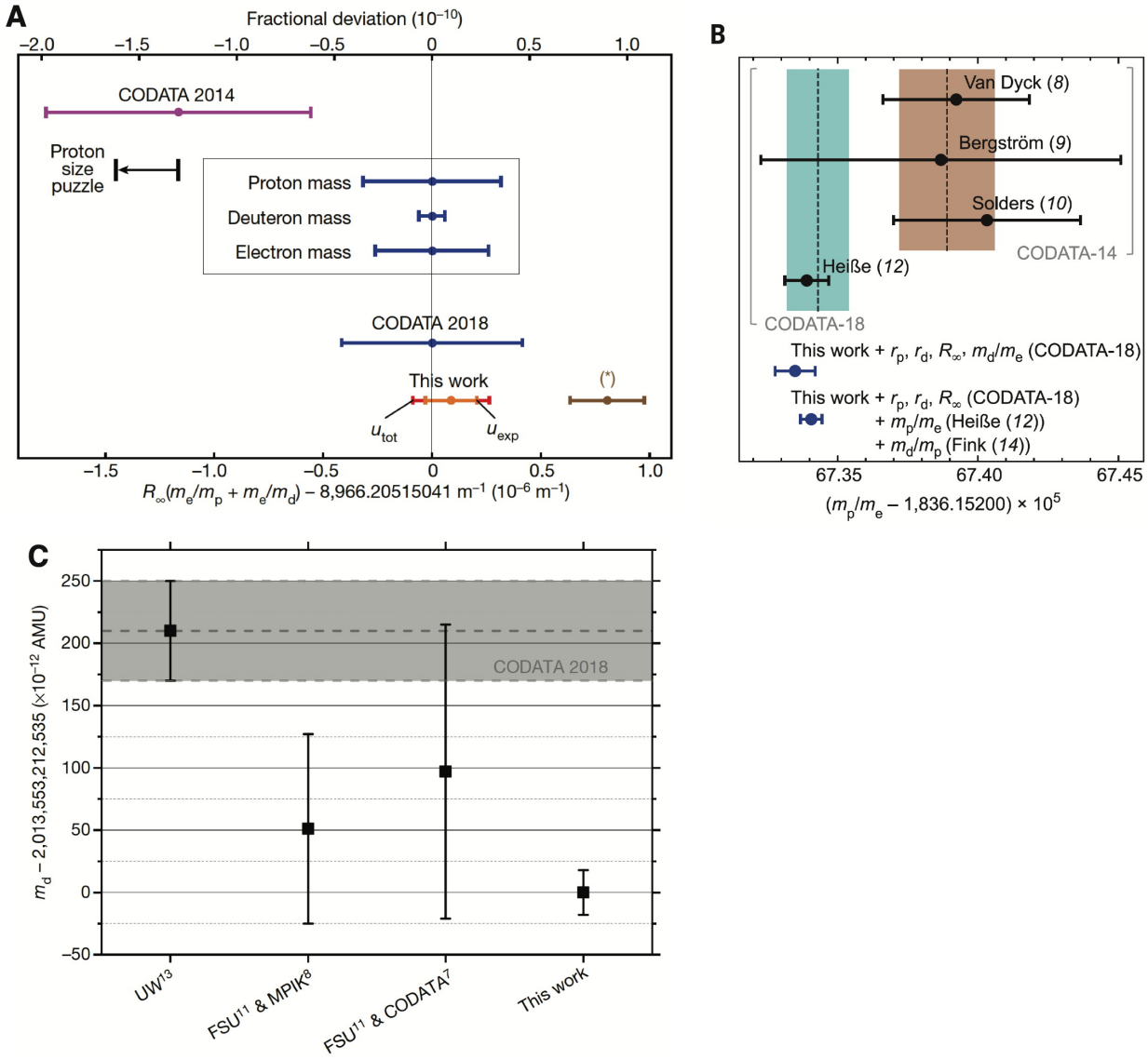

Figure 5 – (A) Comparison of the results of the Düsseldorf-based experiment [18] published in 2020 relative to literature values. In the inner box, the error bars for the CODATA2018 value of $R_\infty(m_e/m_p + m_e/m_d)$ for the hypothetical cases that the uncertainties of all contributing physics constants were zero, except for the named constant (see text of original paper). Black arrow indicates the shift of the CODATA2014 value for the change ΔR_∞ of the Rydberg constant which corresponds to the so-called proton size puzzle [97]. The brown data point shows the result when the CODATA2014 values of the proton and deuteron charge radii determined from muonic hydrogen spectroscopy are used. From Ref. [18]. (B) Results of the Amsterdam-based experiment [19] published in 2020. The proton-to-electron mass ratio m_p/m_e compared with measured m_p values from other sources, which were converted to values of m_p/m_e through division by m_e (CODATA-2018). From Ref. [19]. (C) Deuteron mass determined by a Penning trap experiment in 2020 compared with previous values and the CODATA-2018 value, see Ref. [30] for details.

These results with a relative precision of $\approx 2 \times 10^{-11}$ critically depend on several physical constants including the proton and deuteron charge radii and the deuteron mass in atomic units. The latest physical constants compiled by the Committee on Data for Science and Technology (CODATA) in 2018 were used in the determination. The proton charge radius puzzle (see Fig. 5) introduces a particularly significant shift to the m_p/m_e value.

Meanwhile last year the Heidelberg-Darmstadt-Mainz collaboration determined the deuteron mass as,

$$m_d = 2.013553212535(11)_{\mathrm{stat}}(13)_{\mathrm{sys}}(17)_{\mathrm{tot}}\mathrm{AMU}, \tag{4}$$

in an experiment involving a Penning trap [30]. This result differed from the CODATA-2018 value used in the above determination of M_p/m_e based on HD^+ laser spectroscopy by 4.8 standard deviations. This would consequently also shift the proton-to-electron mass ratio compared to the above-mentioned values. Generally the most precise determinations of many other fundamental constants similarly rely on both theoretical calculations and other constants in a complex way.

The antiproton-to-electron mass ratio determined by laser spectroscopy of $\overline{p}He^+$ is sensitive to a different set of physical constants compared to the HD^+ case and therefore provides important complementary data in addition to the fact that we are studying the antiproton. These constants include the masses of the constituent ^{3}He and ^{4}He nuclei but not the deuteron mass. The corrections to the $\overline{p}He^+$ transition frequencies due to the finite charge radii of the helium nucleus (4–7 MHz) and the antiproton (< 1 MHz) are much smaller than the corresponding contributions in HD^+ or the 1s–2s transition in atomic (anti)hydrogen because the Rydberg antiproton orbitals studied here have negligible overlap with the nucleus. The antiproton is polarized away from the 1s electron by the repulsive Coulomb interaction. For this reason, laser spectroscopy of $\overline{p}He^+$ can provide another important constraint by which the (anti)proton-to-electron mass ratio and the above physical constants can be disentangled and independently determined.

3.2 High-precision theoretical calculations of $\overline{p}He^+$

In 2020 the theoretical collaboration including the Laboratoire Kastler Brossel Paris, JNIR Dubna, and the Wuhan Institute of Physics and Mathematics published some results [20, 98] regarding the calculations of the hyperfine structure of H_2^+ and HD^+. The complete effective Hamiltonian for these ions at the $m_e\alpha^6$ and $m_e\alpha^6(m_e/M)$ orders were derived following the nonrelativistic QED method. The Hamiltonian was then used to numerically calcuate the corrections to the electron spin-orbit interactions for some transitions studied in the above experiments. The theoretical uncertainty was reduced by a factor > 3 compared to before. In the case of $\overline{p}He^+$ a hyperfine structure arises due to the spin-spin interaction between the orbital antiproton and electron. The authors note that the same methods to derive the effective Hamiltonian of HD^+ can be used to improve the hyperfine structure calculations of $\overline{p}He^+$ as well. Efforts in that direction are ongoing.

In a second recent work [98], the electron-proton and electron-deuteron spin-spin scalar interactions in HD^+ were calculated with an uncertainty of less than 1 part per million. A deviation of 4 standard deviations between the theroretical value and the 2020 experimental result for the hyperfine structure of the two-photon transition $(\nu, L) = (0, 3) \rightarrow (9, 3)$ [19] was found. The reason for this deviation is not understood. On the other hand, a good agreement between experiment and theory was found for the H_2^+ ion. It is planned to possibly recalculate this contribution using other theoretical methods.

Some future goals of the theoretical groups include calculating the $m_e\alpha^6$- and $m_e\alpha^7$-order corrections for the three-body system in terms of the spin-averaged energy and the effective spin Hamiltonian. Longer-term goals stated by the Dubna group include the development of an effective method for the two-center Dirac equation and calculations of the one-loop self-energy in all orders

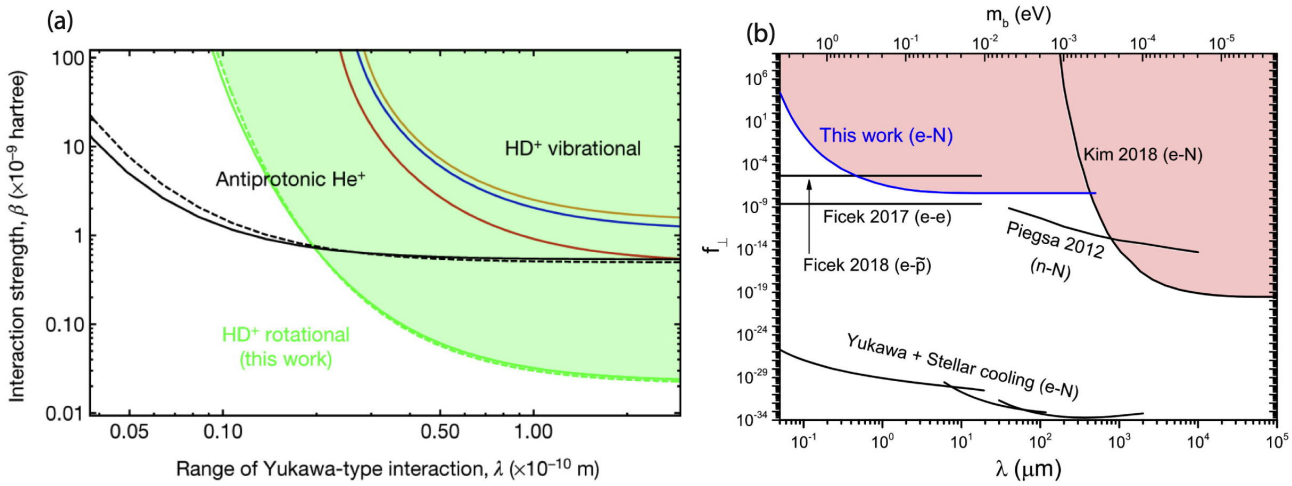

Figure 6 – (a): Exclusion plot of 95% confidence limit for a Yukawa-type interaction between a proton and a deuteron deduced by spectroscopy of HD^+ carried out by the Düsseldorf collaboration compared with the corresponding plot between an antiproton and ^{4}He nucleus determined by laser spectroscopy of $\overline{p}He^+$ measured by ASACUSA. From Ref [18]. (b): Limits on the coupling constant for velocity and spin-dependent exotic forces between a gold sphere and a microfabricated magnetic structure using a cantilever as a function of distance λ between the two objects published in 2020. The result is compared with the limit for the electron-antiproton interaction determined by $\overline{p}He^+$ spectroscopy (indicated by the horizontal line labelled "Ficek 2018"). From Ref. [47].

of $Z\alpha$. Both are challenging tasks but would ultimately allow the precision of the calculation to reach $\approx 6 \times 10^{-12}$ or better.

3.3 Limits on exotic beyond-the-Standard Model forces

The good agreement between the experimental and calculated rotational transition frequencies of HD^+ was used to set limits to the hypothetical existence of a spin-averaged fifth force that may arise between a proton and a deuteron. The corresponding potential was parameterized in the form of a Yukawa-type interaction,

$$V_5(R) = \beta N_1 N_2 \exp\left(-R/\lambda\right)/R, \tag{5}$$

where R denotes the distance between the proton and deuteron, λ the interaction range, $N_1 = 1$ and $N_2 = 2$ the nuclear mass numbers, and β the interaction strength. Fig. 6 (a) shows the limits derived from the HD^+ spectroscopy experiments compared with the corresponding plot between an antiproton and helium nucleus determined by laser spectroscopy of $\overline{p}He^+$ measured by ASACUSA. The sensitivity of $\overline{p}He^+$ becomes greater for small interparticle distances $\lambda < 2 \times 10^{-11}$ m due to the unusually small average distance between the antiproton and helium nucleus within the atom. This motivates us to further improve the experimental precision.

In 2020 a China-United Kingdom-Singapore collaboration published limits [47] on the coupling constant $f_\perp$ for velocity and spin-dependent exotic forces that may arise between a gold sphere and a microfabricated magnetic structure using a cantilever. The force was parameterized in the form,

$$V(r) = -f_\perp \frac{\hbar^2}{8\pi m_e c} \left[\hat{\sigma} \cdot (\vec{v} \times \hat{r})\right] \left(\frac{1}{\lambda r} + \frac{1}{r^2}\right) e^{-r/\lambda} \tag{6}$$

in which $\hat{\sigma}$ denotes the spin unit vector of the electron, $\vec{v}$ the relative velocity between an electron and a nucleon, $\hat{r} = \vec{r}/r$ the unit vector in the direction between them, and $\lambda = \hbar/m_b c$ the interaction range mediated by a beyond-the-Standard-Model boson with a mass between $m_b \approx 10^{-5}$ eV and 1 eV. Their result is shown in Fig. 6 (b). Limits on similar interactions that may arise between an electron and antiproton have been determined by $\overline{p}\mathrm{He}^+$ spectroscopy (indicated by the horizontal line labelled "Ficek 2018"). The sensitivity becomes especially high at smaller interparticle distances of a few micrometers or less.

4 ASACUSA publications

In the last year ASACUSA completed the analysis and submitted several experimental publications besides the laser spectroscopy experiment of pionic helium described above. As mentioned previously, one publication concerns the unexpected behavior in the laser resonance spectra of $\overline{p}\mathrm{He}^+$ atoms implanted in condensed helium targets. This may provide information about the microscopic properties of the quantum liquid using antiprotons as probes, which may be compared with conventional experiments that utilize neutrons or muons in the field of materials science.

A second submitted paper concerns limits on the cross sections of antiprotons with kinetic energy $E \approx 125$ keV annihilating in carbon foils of sub-100 nm thickness, and foils with Pd and Pt layers deposited on the surface [87–89, 92–94, 99]. It was found that these measurements are extremely difficult because of a large number of background processes and the pulsed nature of the antiproton beam at the AD facility. The most serious background involves large-angle Rutherford scattering of the antiprotons in the target foils. Some of the antiprotons are scattered into 90-degree angles and come to rest in the foil, and this cannot be distinguished from the signal that arises from in-flight antiproton annihilations. These backgrounds can be reduced by using free-standing target foils of large ($d = 100$ mm scale) diameter which however are extraordinarily difficult to handle. We were nevertheless able to set upper limits on the cross sections which agree with existing theoretical models. Our impression is that the measurements should preferably be carried out at higher antiproton energies of $E = 0.2 - 1$ MeV and a slow-extracted beam. This may become possible in future antiproton facilities. In the meantime, the submitted result may constitute the best measurement that can be achieved in this energy region under the circumstances.

Other publications are also under preparation.

5 Preparations for the 2021 beamtime

5.1 Overview and candidate two-photon transitions in the first phase of ELENA experiments

The thermal motion of $\overline{p}\mathrm{He}^+$ broadens the measured width of the laser resonances by $\nu\sqrt{8k_B T \log 2/Mc^2}$, where ν denotes the transition frequency, T the atomic temperature, k_B the Boltzmann constant, M the atom's mass and c the speed of light. This loss in spectral resolution limits the precision by which the resonance centroid can be determined. Our experiment utilizes two-photon spectroscopy [3] wherein the atom is irradiated with two counter-propagating laser beams of optical frequency ν_1 and ν_2 to drive the two-photon transition $(n, \ell) \rightarrow (n-2, \ell-2)$. The small transition probability related to this process can be enhanced by factor $> 10^5$ if the counter-propagating laser beams are tuned such that the virtual intermediate state ies within $\nu_d \sim 10$ GHz of the real state $(n-1, \ell-1)$.

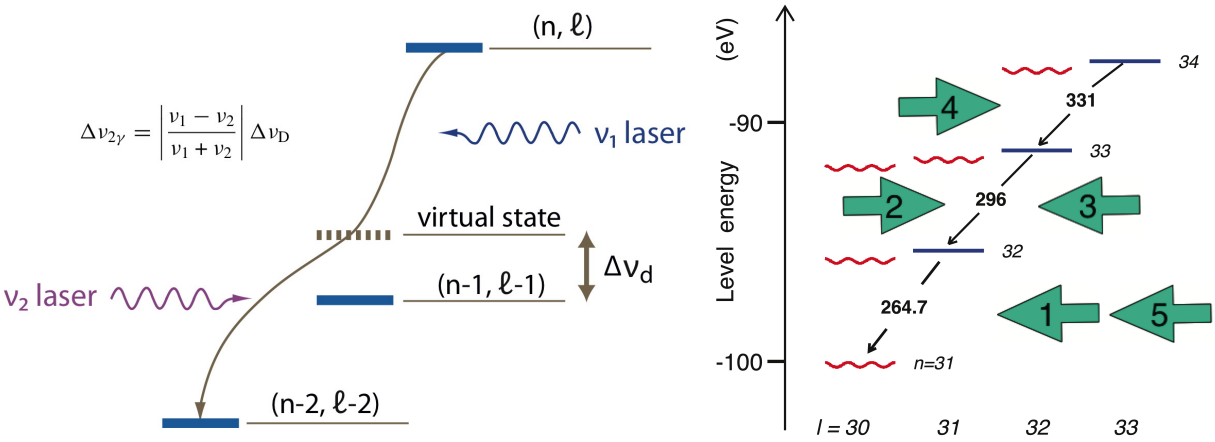

Figure 7 – **Left:** Schematic energy level diagram showing the principle of two-photon laser spectroscopy which will be carried out in 2021. The $\overline{p}\mathrm{He}^+$ are irradiated with two counter-propagating laser beams with their optical frequencies ν_1 and ν_2 adjusted so that the virtual intermediate state lies close to a real state $(n-1, \ell-1)$. This increases the probability of the sub-Doppler two-photon transition where the atom emits two photons simultaneously and deexcites from the state (n, ℓ) to $(n-2, \ell-2)$. **Right:** Energy level diagrams of the $\overline{p}^4\mathrm{He}^+$ isotope indicating an example transition $(n, \ell) = (33, 32) \rightarrow (31, 30)$ relevant for future measurements beyond the second phase of our ELENA experiments. The principal n and angular momentum ℓ quantum numbers, and the level energy relative to the three-body breakup threshold are shown. The transition wavelengths in nanometers are indicated. In a future series of experiments, we will measure the transition $(34, 33) \rightarrow (32, 31)$ using five laser beams 1–5 fired in sequence. This requires that the experiment be first optimized with respect to the ELENA beam.

Table 1 – Candidate two-photon transitions of $\overline{p}^4\mathrm{He}^+$ and $\overline{p}^3\mathrm{He}^+$ isotopes that will be measured in the first phase of experiments using the ELENA beam starting 2021.

Transition $(n, \ell) \rightarrow (n', \ell')$	Transition frequency Theory (MHz)	Natural width (MHz)	Precision limit	Published precision
	$\overline{p}^4\mathrm{He}^+$ atom			
$(36, 34) \rightarrow (34, 32)$	1522107061.07(12)	36	10^{-10}	$< 3 \times 10^{-9}$
$(33, 32) \rightarrow (31, 30)$	2145054858.50(10)	63	10^{-10}	$< 3 \times 10^{-9}$
	$\overline{p}^3\mathrm{He}^+$ atom			
$(35, 33) \rightarrow (33, 31)$	1553643085	109	$< 10^{-9}$	5×10^{-9}
$(33, 32) \rightarrow (31, 30)$	Under evaluation	44	10^{-10}	

A previous series of experiments [3, 16] used a RFQD to slow down the antiprotons, but the inherent limitations of the decelerator design caused $\approx 80\%$ of the antiprotons to miss its longitudinal acceptance and emerge with little or no deceleration. The remaining 20% fraction of slow antiprotons came to rest in a cryogenic helium gas target, thereby producing $\overline{p}\mathrm{He}^+$. The atoms were then irradiated by $\Delta t = 40$ to 100 ns long laser pulses [21] with peak powers $P = 0.5$ to 10 kW. This induced atomic transitions between long-lived $\overline{p}\mathrm{He}^+$ states with microsecond-scale lifetimes, and short-lived states with nanosecond-scale lifetimes against Auger emission of the 1s electron. The two-body $\overline{p}\mathrm{He}^{2+}$ ion [83] formed after Auger decay was destroyed by collisions with normal helium atoms in the experimental target. The resulting peak in the rate of antiproton annihilations [100] signalled the resonance condition between the lasers and atom. The geometrical volume that the

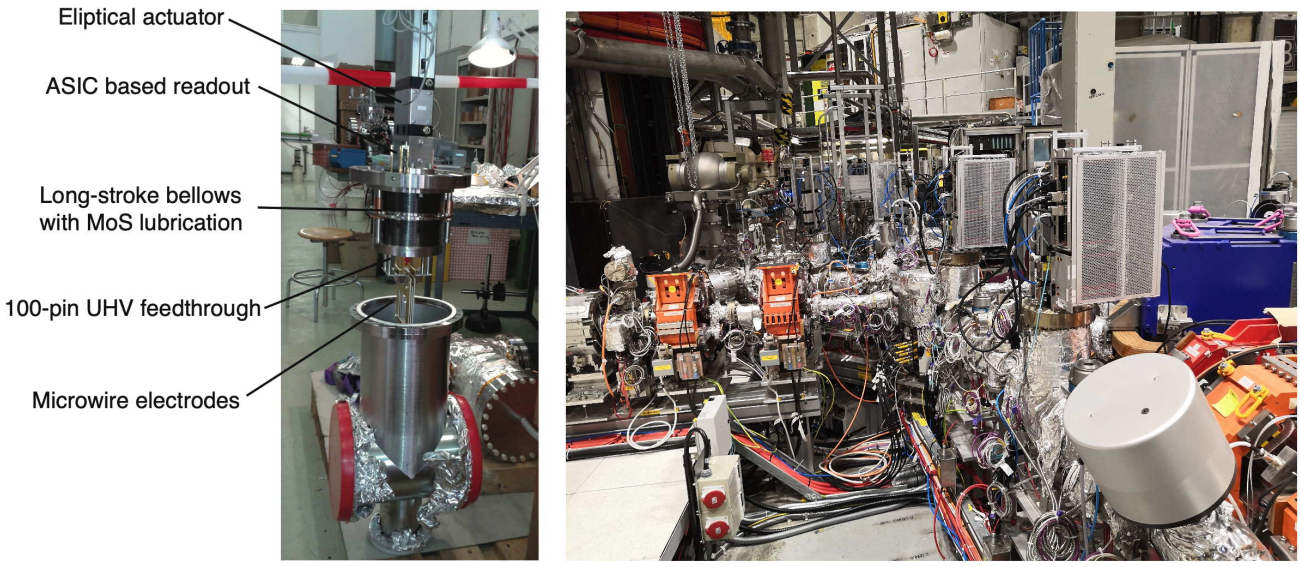

Figure 8 – Left: Photograph of the beam profile monitor (courtesy ELENA development team of CERN). Position-sensitive electrode grids are mounted on a large-stroke bellows unit. The femtocoulomb-scale electric charge induced by the small fraction of antiprotons intercepted by the wires with diameter of $d = 20$ μm are detected by ASICs. The semi-non-destructive nature of the monitor allows the four antiproton beam pulses that circulate in ELENA to be measured and distributed rapidly to the user beamlines. Right: Photograph of several monitors installed on the ejection beamline of ELENA that leads to AEGIS, ALPHA, BASE, and ASACUSA.

sample of $\overline{p}\mathrm{He}^+$ occupied was quite large ($d > 20$ mm diameter) because of the extended size of the RFQD beam and the large energy spread. This necessitated the use of excessively high-power lasers to fully irradiate the volume. Only a fraction of the antiprotons contributed to the $\overline{p}\mathrm{He}^+$ signal whereas the majority produced background.

The cooled antiproton beam of ELENA should allow up to an order-of-magnitude increase in the number of $\overline{p}\mathrm{He}^+$ atoms produced per year, and a factor > 20 increase in the annual data collection rate compared to these earlier RFQD-based experiments. Table 1 shows four of the most intense two-photon transitions [2, 17] $(n, \ell) \rightarrow (n-2, \ell-2)$ of $\overline{p}^3\mathrm{He}^+$ and $\overline{p}^4\mathrm{He}^+$ isotopes which we plan to measure in the first phase of our experiments in 2021 and beyond. The transition frequencies have been calculated to a fractional precision of $(5-6) \times 10^{-11}$ [101, 102], which corresponds to a sensitivity to the antiproton-to-electron mass ratio of less than 4 parts in 10^{-11}.

After we have gained sufficient experience using the ELENA beam to measure the intense resonances, transitions between states with microsecond-scale radiative lifetimes with natural widths of ≈ 0.2 MHz will be searched for [17,95]. These weak resonances are far more difficult to resolve [100], and would ultimately require five laser beams arranged in a pump-probe configuration. The limit of the precision due to the natural width would be increased hundredfold. This would require many years of systematic studies using ELENA and optimizing the beamline optics and the cryogenic target.

5.2 Beam profile monitors for ELENA

Of crucial importance to the $\overline{p}\mathrm{He}^+$ experiment is the efficient transport of the antiproton beam which must be focused into the smallest possible volume in the helium target to take advantage of

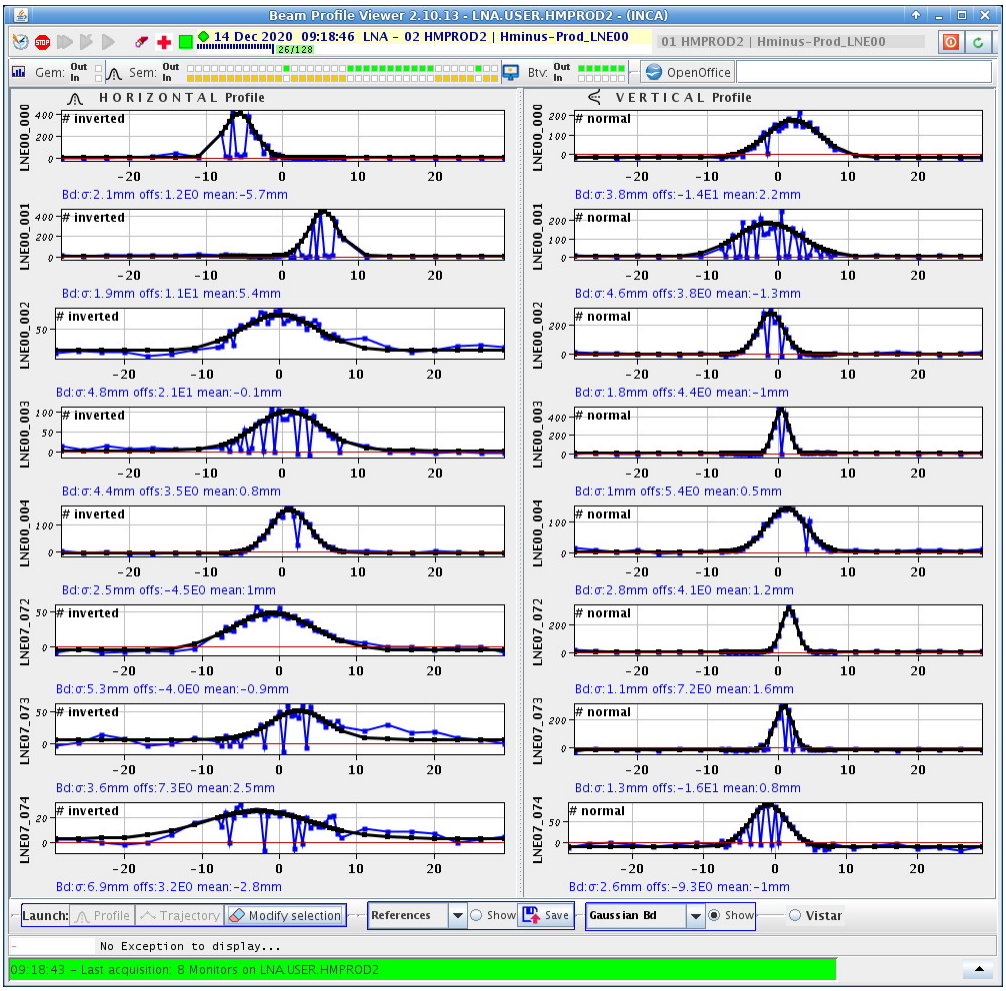

Figure 9 – The horizontal and vertical spatial profiles of the H^- beam measured by the ELENA operations team of CERN and recorded in the ELENA logbook in 2020. The plots indicate the profiles of a single beam pulse measured in a semi-non-destructive way by 8 monitors which are located along the extraction beamline leading to one of the AD experiments. This allows rapid beam steering to be carried out without sequentially inserting and removing each monitor. Some monitors show disconnection of some wires, most of which possibly occurred during the baking process to 200°C. This problem (which to first approximation does not seem to affect the function of the monitors in transporting the beam to the experiments) was reduced in later series of monitors. Devices with a large number of dead wires may be replaced or repaired.

the cold characteristics of the ELENA beam and minimize background. The spatial profile monitors placed in the user beamlines are vital to these priority efforts in 2021.

The ASACUSA $\overline{p}He^+$ collaboration provided 43 monitors to measure the spatial profiles of the antiproton and H^- beams in the injection, ejection, and user beamlines. During 2019–2020 the ELENA construction team took over the responsibility regarding the assembly and installation of the devices, whereas ASACUSA continued to provide electronics, wire electrodes, and vacuum bellows units with signal feedthroughs. The semi-non-destructive nature of the monitor should allow the four antiproton beam pulses that circulate in ELENA to be measured and distributed to four user experiments simultaneously in an efficient and reliable way. As mentioned last year,

the device detects femtocoulomb-scale electric charge induced by the small fraction of antiprotons intercepted by a grid of wires with diameter of $d = 20$ μm [103]. This must be achieved within the high radiofrequency noise environment of the AD hall.

Most of the monitors in the beamlines leading to the AEGIS, BASE, GBAR, and ALPHA experiments have been installed. The ASACUSA-1 beamline was also equipped with monitors, whereas the electrodes needed to implement the missing ASACUSA-2 and two ATRAP beamlines have been delivered at the end of 2020. With technical assistance of CERN experts, a third iteration of preamplifier prototypes were developed and used to measure the H^- beam along the ejection beamlines of ELENA in 2019. Based on the results, the ELENA construction team selected the preamplifier design among the three tested options. The full set of preamplifiers needed to equip the entire facility was delivered by mid 2020, though we encountered some delays due to COVID-19 issues in Japan. Max Planck Institute and University of Tokyo, Komaba campus provided a portion of the funding to cover some of the missing monitor parts.

In autumn 2020, the CERN operations team circulated the H^- beam in ELENA, ejected the beam, and transported it to several experiments. Fig. 9 shows a typical measurement of the horizontal and vertical profiles of a single H^- pulse measured at 8 locations along the beamline. The fact that each monitor intercepts only a small fraction of the beam and allows most of the H^- to traverse the grids allowed comparably rapid beam steering. This is in contrast to previous destructive detectors which required the repetitive insertion and removal of the monitors to sequentially transport the antiproton beam to each experiment.

As shown in Fig. 9, some monitors show that a fraction of the total ≈ 90 wires in the vacuum are disconnected. Some of these disconnections were found to be correlated with the baking of the monitor to $T = 200$ °C at CERN which caused the fluxless soldering on the pins to fail. This issue was discussed in last year's report and has been studied during 2019–2020 in Japan. The problem would be solved if either organic flux or adhesive were allowed to be used as is ususually done in this type of application; however due to very reasonable issues related to possible contamination of the beamline and pumps by sublimation of organic material, the CERN vacuum experts took the decision to continue using fluxless solder which ensures no long-term residue. In the meantime, tests with adhesive are being continued at CERN. This disconnection problem does not seem to adversely affect the main function of the monitors in transporting the beam to the experiments. Devices with a large number of disconnected wires may be replaced or repaired, and efforts toward this goal are being carried out in Japan now. In the medium and longer terms, the intent is to fully transfer all related knowledge to CERN so that operation would not rely on any Japanese support.

We again deeply thank the CERN accelerator groups for their great efforts and support on this project. Most of the expertise to operate and service the monitors have been transferred to CERN experts and it appears everything will be in place to transport the beam to the experiments in 2021.

5.3 Simulation and layout of the beamline in the $\overline{p}He^+$ spectroscopy experiment

There were two principal sources of background in the previous experiments that utilized the RFQD [95]. The first arises from $\pi^+ \to \mu^+ \to e^+$ decay which is proportional to the number of antiprotons that stop in the helium target, the walls of the target chamber, or the upstream beamline [100]. The second background is due to the spontaneous deexcitation and annihilation of $\overline{p}He^+$ which constitute a continuous time spectra. As the RFQD did not cool the antiproton beam during deceleration, its diameter $d \geq 20$ mm, energy spread ≥ 10 keV, and emittance > 50 π mm mrad were large. In the ELENA experiments the signal-to-noise ratio is estimated to increase by a factor > 3 due to the larger geometrical overlap between the antiproton beam and counterpropagating

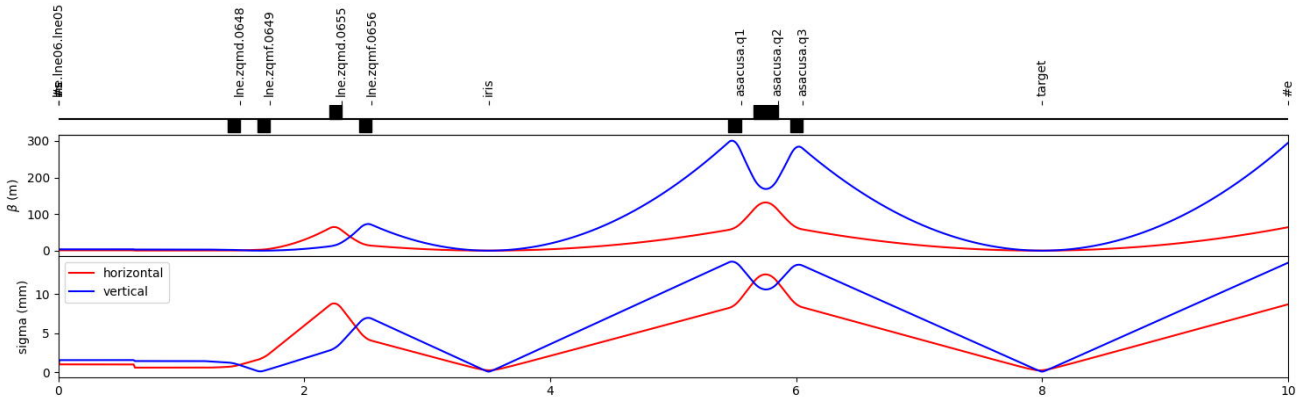

Figure 10 – The horizontal and vertical β-parameters and root-mean-square (RMS) beam size radii of the ELENA antiproton beam in the DE1 beamline simulated by the TE-ABT-BTP group (courtesy, Yann Dutheil). A large focal length is needed to attain a sub-millimeter root-mean-square beam size in the experimental target.

laser beams that irradiate the $\overline{p}\mathrm{He}^+$ atoms. Another factor ≈ 2 improvement is expected from the increase in the efficiency of the antiprotons coming to rest in the experimental target. For achieving these gains it is essential to focus the beam into a small spot in the experimental target.

The CERN TE-ABT-BTP group carried out simulations of the beamline which extends some 5 m downstream of the last gate valve of the DE1 experimental zone. The horizontal and vertical β-parameters and root-mean-square (RMS) beam radii are shown in Fig. 10. A mechanical iris of diameter $d < 10$ mm is positioned at a distance 1 m from the gate valve and serves as a conductance limiter to reduce the flow of helium gas from the experimental target towards the ELENA beamline. This is needed to sustain the vacuum in the upstream beamline to the nominal value of $p \approx 10^{-9}$ mb. An electrostatic quadrupole triplet of diameter $d = 100$ mm developed by ASACUSA then refocuses the beam. A final 2 m long section of beam pipe leads to the experimental target. The simulation indicated that the beam spot in the target would have the required sub-millimeter root mean square (RMS) size.

Fig. 11 shows the layout of the beamline superimposed on the existing DE1 beam area. The positions of the above-mentioned iris, large-aperature quadrupole triplet, and experimental target are shown. Two beam profile monitors are foreseen. Three turbomolecular and ion pumps will provide differential pumping along the beamline. Two gate values help to isolate the various portions of the beamline.

In parallel to this, efforts are being continued to construct the induction decelerator for slowing down the antiprotons to energy $E \leq 50$ keV. The prototype device will be transported to CERN in February 2021. Simulations show that the operation of this device is unnecessary for the initial experiments; it will benefit future phases of the measurement.

5.4 Energy loss calculations of ELENA beam through BoPET foils

ASACUSA is collaborating with a theoretical group of Helsinki university to study the deceleration of antiprotons of kinetic energy $E = 65 - 110$ keV in biaxially-oriented polyethylene terephthalate (BoPET) foils, and determine the correct foil thickness [104] that constitutes the entrance window of the experimental target. Quantum chemical methods were used to determine the nuclear stopping power and the interparticle potentials between antiprotons and the constituent atoms of BoPET.

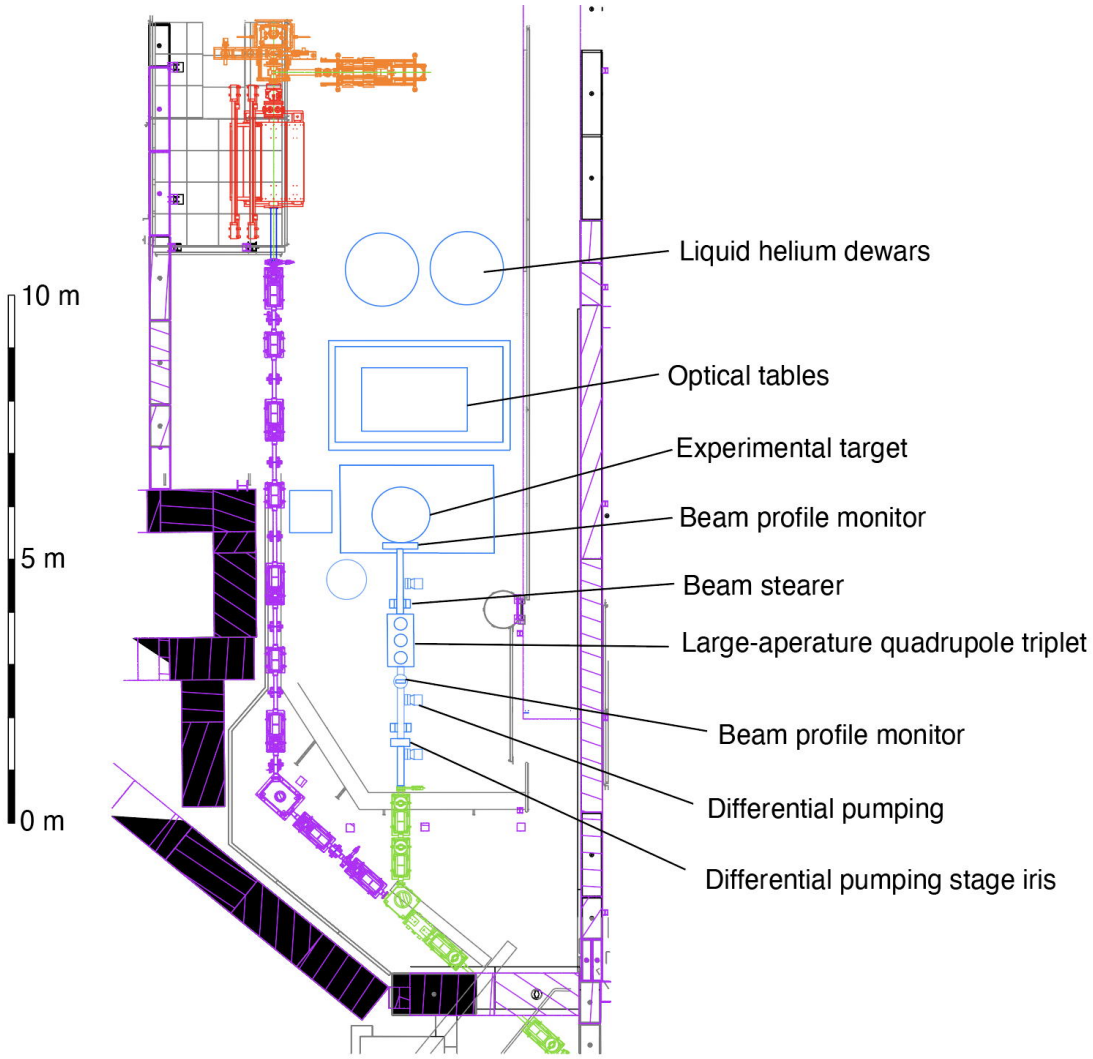

Figure 11 – Layout of the DE1 beamline in 2021 for laser spectroscopy of $\overline{p}\mathrm{He}^+$. The beamline consists of a differential pumping stage, large-aperture electrostatic quadrupole triplet, beam steers, beam profile monitors, and experimental target.

The motions of the antiprotons through the foil were then simulated using the molecular dynamics range calculation method. We compared the results with past experimental data collected by the collaboration regarding the intensity of the laser resonance signal as a function of the incident beam energy $E = 65 - 110$ keV. A good qualitative agreement was found. Cryogenic vacuum flanges which are optimized for the expected beam diameter are being constructed based on the simulations and measurements. They will be tested in April of 2021.

5.5 Laser systems

As described in our 2018–2019 status reports, the ASACUSA laser hut is being modified to provide space for the new collaboration as requested by CERN. It is expected that the modifications will be completed in the next 2 months. The lasers needed for the 2021 run are essentially ready. The data acquisition system for the lasers has been upgraded, and Ti:sapphire crystals and other consumables

are being prepared. The optical tables and optics will be installed in the DE1 beamline starting February 2021.

As described in our proposal of 2019, the laser systems are based on injection-seeded Ti:sapphire ring lasers of circumference $\ell = 800$ mm that produce single-line-mode laser pulses of energy $E = 20$ mJ and wavelength $\lambda = 730-890$ nm. The spurious modulation in the optical frequency of the laser light during the pulsed amplification are corrected by intracavity EOM's. Each pulsed amplifier is seeded by continuous-wave (cw) lasers of linewidth $\Gamma < 10$ kHz which are stabilized against high-finesse cavities isolated in a vacuum chamber. The seed laser frequencies are measured using an erbium optical frequency comb. The Ti:sapphire pulsed lasers are pumped by Nd:YAG lasers with a high pulse-to-pulse stability. For this three Nd:YAG pulsed laser resonators with an intracavity electro-optic modulator (EOM) are being developed in addition to two existing lasers which will be used in the initial experiments.

In 2020 the Amsterdam group [25] demonstrated a similar laser system as the one used by ASACUSA [16]. By comparing the pulsed laser output to a cw laser which was locked to an optical frequency comb, an Allan deviation of 5×10^{-11} at a 10 second integration time was demonstrated. This implies that significant improvements in the experimental precision of the $\overline{p}\mathrm{He}^+$ transition frequencies are possible by improving our laser systems in a step-by-step manner. We have upgraded some MOS-FET drivers that control the intracavity EOM's to improve the linewidth of the lasers. Measurements will be restarted when the above-mentioned modifications to the laser hut are completed.

The interrogating lasers must be referenced to a precise frequency standard. In 2020 the collaboration continued studies aimed at the improvement of the frequency standards to a precision of $\approx 10^{-11}$ when integrated over multiple laser pulses during the microsecond-scale lifetime of the $\overline{p}\mathrm{He}^+$ atom. We hope to take advantage of recent improvements in the technology demonstrated in Max-Planck Institute of Quantum Optics and at the company Menlo Systems GmbH.

5.6 Optical reference signals from metrological institutions to CERN

The frequency reference chain used in the experiment will consist of a global positioning satellite (GPS)→ hydrogen maser →frequency comb→Ti:Sapphire laser. Although this appears sufficient for the needs of our experiment, it is nevertheless highly beneficial to have a means of verifying the operation of the chain and the correctness of the measurement using an independent optical frequency standard.

In 2020 the ASACUSA collaboration continued discussions with the Federal Institute of Metrology (METAS) of Switzerland which is responsible for the realization and dissemination of the Swiss Time scale UTC(CH) according to the Coordinated Universal Time. METAS owns an active hydrogen maser referenced to a two-way satellite time and frequency transfer (TWSTFT). The Swiss Cs continuous primary frequency standard FoCS-2 (Fontaine Continue Suisse) in Bern achieved a relative uncertainty of 1.99×10^{-15} and a short-term stability of 8×10^{-14} at an integration time of 1 second [105].

As mentioned last year, there is an ongoing SNF-Sinergia research project between the University of Basel, ETH Zürich, METAS, and the Swiss national research and education network SWITCH to carry out precision laser spectroscopy of Rydberg H_2 molecules and molecular ions by utilizing an ultrastable optical frequency standard signal of relative precision $\leq 10^{-15}$ which will be transmitted over 100-km scale optical fiber links between METAS in Bern, Basel, and Zürich (see Fig. 12). This utilizes a so-called "dark channel" (ITU CH07) corresponding to a wavelength $\lambda = 1572$ nm. This link is currently being commissioned and progress indicates that it can be used to significantly improve some spectroscopy measurements at the University of Basel.

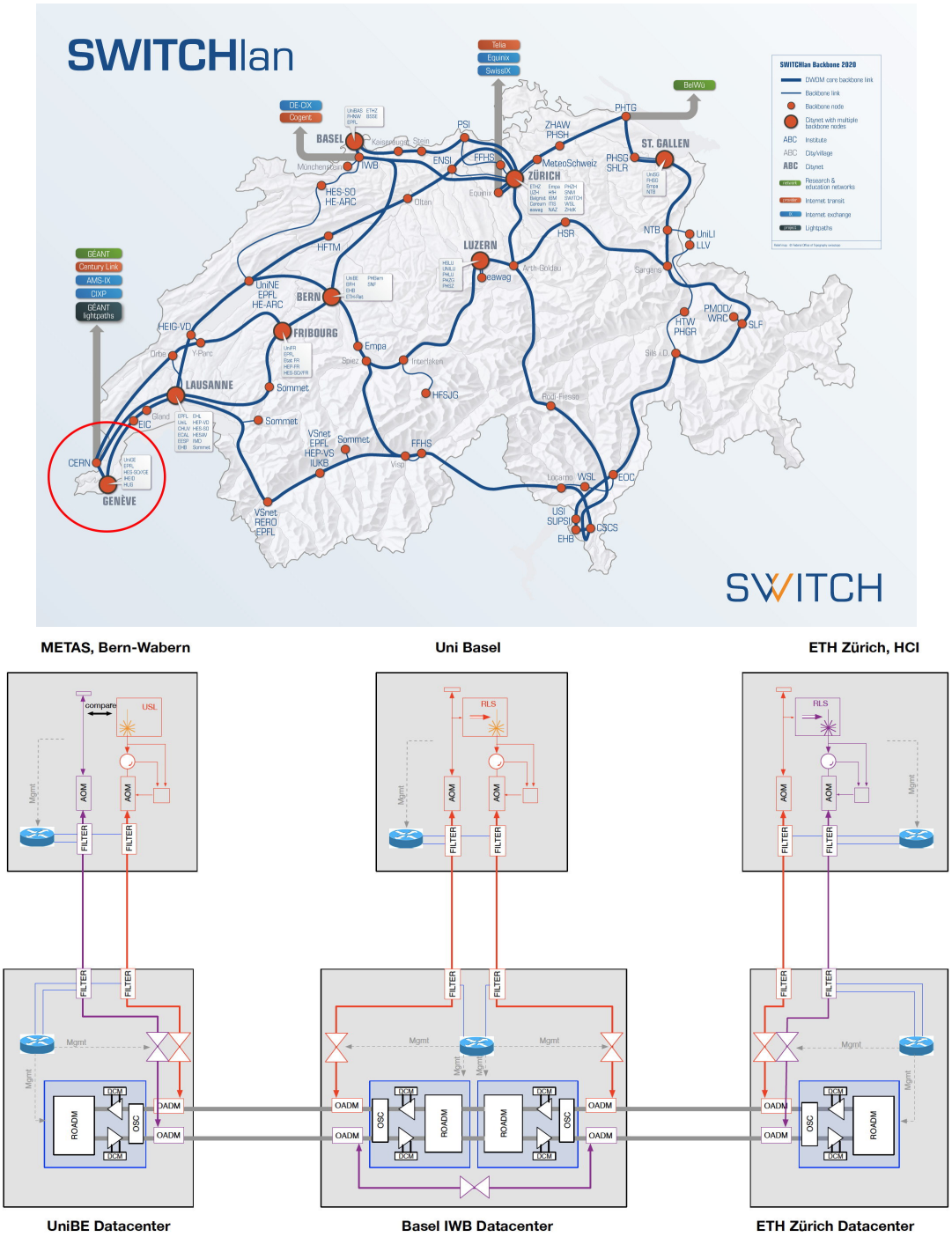

Figure 12 – Top: Geographical layout of the academic and scientific network SWITCHlan. The proposal is to use the existing fiber link between Bern and CERN to transfer the ultrastable optical reference signal which will be used for the $\bar{p}\mathrm{He}^{+}$ experiment. Bottom: Schematic layout of the Bern-Basel-Zürich ultrastable reference signal interconnection which is currently being commissioned. The system is based on a ring structure and bidirectional communication on a single fibre. The signal wavelength is $\lambda = 1572$ nm corresponding to ITU CH 07. A similar transceiver system may be installed in the computer center of CERN in Bat. 513. CERN IT division has tentatively expressed a willingness to administer the system if it can be made blackbox and under the condition that 24h uptime would not be guaranteed. Figures courtesy of SWITCH and METAS.

The dark channel nature of the design allows this reference signal to be transmitted parasitically on existing data fibers administered by SWITCH that connect Bern to CERN. A single fibre may be used in bidirectional communication mode. ASACUSA wishes to collaborate with other AD collaborations, in particular with ALPHA and possibly BASE to utilize such an infrastructure should it become available. The CERN IT department has been supportive and has tentatively and unofficially expressed a willingness to administer the system if it can be made blackbox and under the condition that 24h uptime would not be guaranteed. The data transmission fibers arriving in Bat. 513 will be extended some 200 m to Bat. 193 so that the reference signal to the ASACUSA laser hut and to the other AD collaborations may become available. In 2021 we hope to further the discussions with the Swiss groups and the CERN technical groups.

Part II
Antihydrogen

6 Introduction

The goal of this part of ASACUSA's physics programme is to perform a ppm-scale measurement of the ground-state hyperfine splitting of antihydrogen in a beam. In-beam spectroscopy is complementary to measurements inside a neutral particle trap and is less prone to systematic effects from the large field gradients needed for trapping. Reaching the ppm level is of interest as corrections coming from the finite size of the antiproton become visible below 30 ppm accuracy. The details have been summarized recently elsewhere [106, 107] and in our proposal for ELENA [108].

The layout of the ASACUSA Cusp experiment is shown in Fig.13. Antiprotons from ELENA will be stored in the MUSASHI trap (Sec. 8.2.6) probably with the aid of a drift tube. Positrons are obtained from a ^{22}Na source and a neon moderator then stored in the positron accumulator (Sec. 8.2.5). Together they form antihydrogen in the so-called double-Cusp trap [109, 110]. The double-Cusp trap consists of a multi ringed electrode trap [111] housed within a magnetic field produced by a pair of superconducting coils in an antihelmholtz configuration. A nested penning trap is formed in a region of strong magnetic field before the first of two cusps to mix positrons and antiprotons. The purpose of the cusped field is to focus and polarise cold ground state antihydrogen atoms.

The polarised $\overline{\mathrm{H}}$ atoms escape the trap and enter the spectrometer consisting of a microwave cavity [112] to induce hyperfine transitions, and a state-analysing sextupole magnet. In the Rabi-type resonance method the force from magnetic field gradients exerted on the magnetic moments separates the $\overline{\mathrm{H}}$ atoms according to their spin states (Stern-Gerlach separation): the sextupole magnet focuses the low-field seeking states and defocusses the high-field seekers. A detector records the annihilation signal at the end of the beamline as a function of the microwave frequency applied in the cavity. The challenge lies in producing an intense, focused and polarised source of $\overline{\mathrm{H}}$ atoms in their ground states.

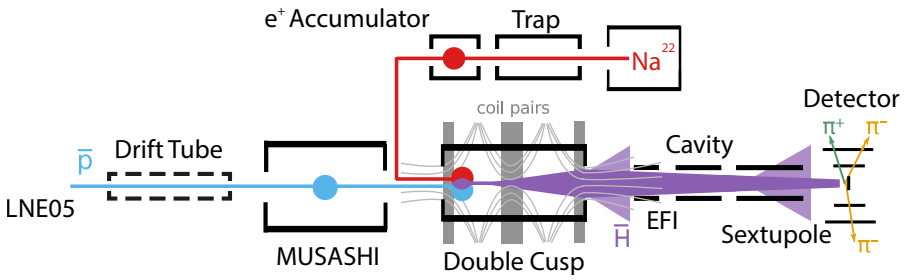

Figure 13 – Sketch of the apparatus to measure the hyperfine structure of antihydrogen. The path for positrons is indicated in red, and for antiprotons in blue. The synthesised antihydrogen beam is marked in purple. Light purple shows high-field seekers (HFS) and dark purple the low-field seeking (LFS) component of the beam. The grey lines represent the magnetic field lines of the Double-Cusp magnet. Possible location of the drift tube is shown as a dashed line.

7 Principal quantum number distribution of formed antihydrogen

Data on the principal quantum number (n)-distribution of antihydrogen atoms previously reported in the annual report for 2018 [113] were reanalyzed and the results are currently in print [114]. Using an external field ionizer (EFI, see Fig. 13) between the $\overline{\mathrm{H}}$ formation region in the Cusp trap and the ASACUSA antihydrogen detector, the number of $\overline{\mathrm{H}}$ atoms arriving at the detector was measured as a function of the EFI voltage (cf. Fig. 14). We found that the previous treatment of the field ionization process was not adequate for the situation of fast moving hydrogen atoms through the EFI and neglected the angular momentum dependence of the field ionization probability. As the distribution of angular momentum states in one n manifold is not known, taking this into account leads to a range of n values to be probed for each EFI setting. For the proper quantum mechanical treatment the transit time during the 10 mm long field ionizer is important, which we can only estimate since the antihydrogen velocity has not been measured. For a very wide range of assumed velocities, the resulting maximum principal quantum number n_{max} ranges of hydrogen atoms passing through the EFI are indicated in Fig. 14. The two n values given for each point are the highest state which can pass the field ioniser region without being ionised and the lowest state which is fully ionised.

The results again show that – as expected for three-body recombination – the antihydrogen atoms occupy primarily high n states. While the value of the lowest observed quantum number has slightly increased from $n < 14$ to $n < 15 \ldots 19$, the primary message is still that efforts are needed to lower the quantum states of antihydrogen atoms formed, and to increase the total production rate. These are the goals of the ongoing improvements described in the following chapters.

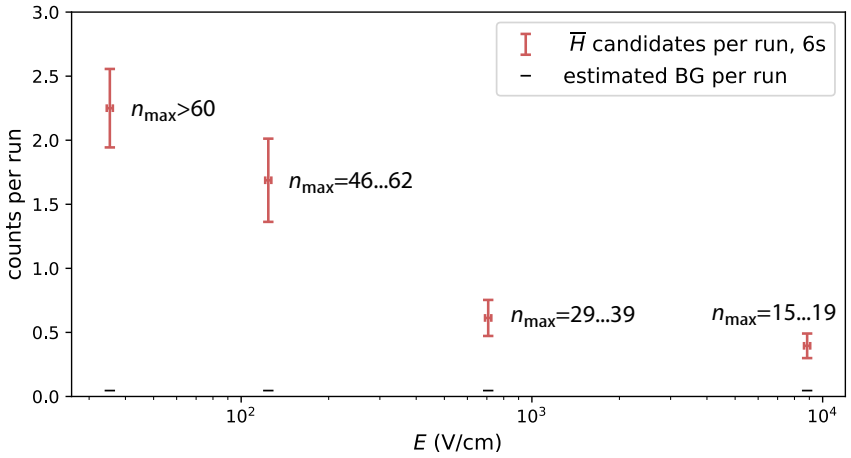

Figure 14 – Number of $\overline{\mathrm{H}}$ candidate events per run for the four field ioniser settings used (red crosses). The corresponding range of principal quantum numbers n_{max} is indicated next to the data points. y-error bars show Poisson errors. The estimated background per run is displayed with horizontal, black bars for each of the four field ioniser settings.

8 Towards in-beam hyperfine spectroscopy of antihydrogen

In the following sections, we will firstly show results from experiments with charged particles taking place during LS2 and we will describe the various upgrades we have made to the experiment this

year. We will then discuss work in progress on future upgrades that we hope to have in place in 2021.

This year has been most unusual due to the ongoing global pandemic, we have had problems with access to laboratories and travel. However, a great deal has been achieved including upgrades to the control system, temperature measurement, plasma manipulation, and ion cyclotron resonance magnetometry. We have succeeded in having a new trap stack for the Cusp constructed and shipped to CERN ready for installation, building and characterising a proton source, and have a new positron accumulator under construction as of the end of 2020.

We have a number of upgrades in progress set to be performed in 2021 which are described below including, a new cold bore for the Cusp trap, upgrades to the MUSASHI trap for compatibility with the new 100 keV ELENA beam, and detector upgrades. All of this work is towards one goal, producing an intense antihydrogen beam with which we can perform our ultimate aim: the precision spectroscopy of antihydrogen.

8.1 Experimental Results and hardware upgrades in 2020

8.1.1 Plasma Temperature

It is impossible to produce a beam of cold $\overline{\mathrm{H}}$ from warm $\overline{\mathrm{p}}$ and e^+ plasmas. The colder these plasmas are, the more low-energy $\overline{\mathrm{H}}$ will be formed when the plasmas are combined. Such plasmas are easily heated by small amounts of RF (few MHz) noise on the trap electrodes [115]. Optimization of the $\overline{\mathrm{H}}$ beam ultimately requires careful RF design and filtering for any cable entering the UHV, the ability to reliably diagnose plasma temperatures $T < 40\,\mathrm{K}$, and systematic characterization of plasma heating in the trap.

Most plasma manipulations, such as moving the plasma, EVC, and slow extraction, may be done with low frequency perturbations ($\tau \sim 10\,\mathrm{ms}$). The strategy adopted in 2020 was to exclude all higher frequencies from the trap using lowpass filters. These filters are mounted in a fully enclosed filterbox which mounts directly to the vacuum feedthrough flange. Low frequency signals are supplied by quiet ($< 0.2\,\mathrm{mV_{rms}}$ from 0 to 20 MHz) amplifiers having 4 ms rise time and $\pm 140\,\mathrm{V}$ range (similar amplifiers were used for the work in Ref. [115]; the design for these amps was generously provided by J. Fajans of the ALPHA collaboration). The lowpass circuitry is selectively bypassed for electrodes U11 (catching, fast dump, ion heating), U10 (rotating wall), and U5 (rotating wall) using normally-open RF relays (COTO-2900) and $50\,\Omega$ termination (see Fig. 19 for electrode names).

Accurate measurement of very low plasma temperatures is challenging. Nondestructive techniques are typically limited to temperatures $T \gtrsim 100\,\mathrm{K}$ and depend on plasma length and radial profiles in a complicated way [116, 117]. The slow extraction procedure (Tdiag) also involves numerous effects such as space charge depletion, radial variation in the confinement potential, and adiabatic expansion cooling during extraction [118]. The worse of these technical challenges is probably the dependence on Debye length $\lambda_D = \sqrt{\epsilon_0 k_B T/\rho e^2}$, where ρ is the plasma density. As the confining potential is slowly lowered, particles at a radius $r \lesssim \lambda_D$ escape first. The arrival rate of these particles, for a voltage ramp $V(t)$, is roughly proportional to $\exp[q(dV/dt)/k_B T]$ [119]. The arrival rate for particles coming from higher radius is more complicated, so that part of the signal is normally discarded. The useful part of the signal therefore scales as $\lambda_D^2 \propto T$. Plasmas with $T \lesssim 10\,\mathrm{K}$ may require single particle resolution to be diagnosed accurately [120].

The upgrades planned for 2021 include a Tdiag system similar to that described in Ref. [120]. In the mean time the standard "charge pickoff" system has been improved to the extent possible. As can be seen in Fig. 15, the resolution is satisfactory for the plasma temperatures obtained this year in the 70 K Cusp Trap (see Section 8.1.4 for further discussion of trap temperature). These

measurements benefit from a two-stage microchannel plate (MCP), a new HV filtering system, and a dedicated IC instrumentation amp (AD8421) which takes the difference of charge flowing to the phosphor screen and the back of the MCP.

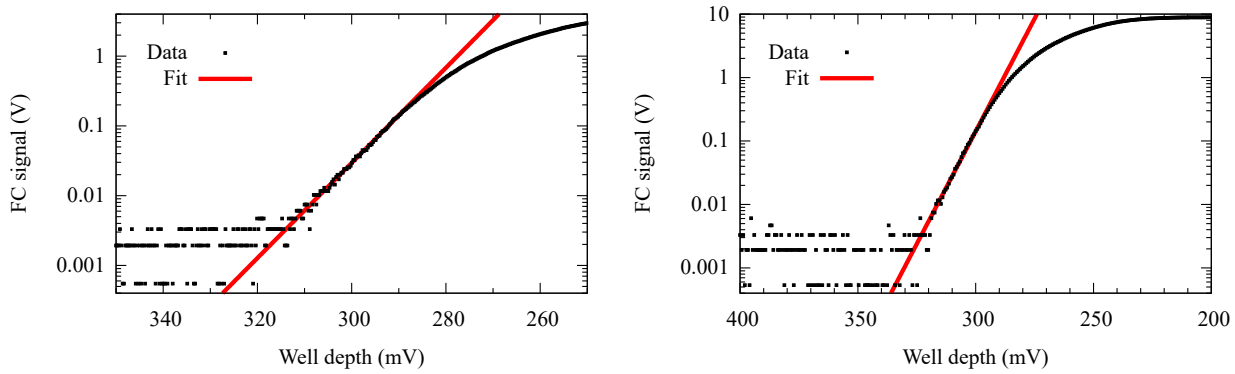

Figure 15 – Temperature diagnosis of evaporatively cooled positron plasmas with varying dump protocol. Protocol A (left side) is to restore only a few volts of confinement prior to dumping at a rate 1.4 V/ ms. Protocol B (right side) is to restore full confinement prior to dumping at a rate 3.4 V/ ms. Protocol A yields more data points on the log-linear rise and a fitted temperature $T = 74\,\mathrm{K}$. Protocol B yields a log-linear region which reaches about a factor of two higher out of the noise and a fitted temperature $T = 71\,\mathrm{K}$.

Nonneutral plasmas do not cool to the trap temperature because of steady heating due to expansion (particles moving down a potential gradient as the plasma radius increases) and electrode noise (stimulation and subsequent damping of plasma modes). Both these factors tend to be worse when the number of plasma particles N is higher. Fig. 16 displays the measured expansion rate (time for the plasma radius to double), calculated heating due to expansion, and final temperatures for plasmas containing a wide range of N. In every case an SDR rotating wall perturbation (see next section) was used to initialize the plasma density $\rho \approx 5 \cdot 10^{14}\,\mathrm{m}^{-3}$. Two models for the final temperature are graphed on the right side with the data. Model 1 assumes that the final temperature is the wall temperature plus the ratio of expansion heating, from the left graph, to cyclotron cooling ($0.5\,\mathrm{s}^{-1}$ for the magnetic field at the center of the plasma) [115]. Model 2 is Model 1 with an additional *ad hoc* heating term $\sqrt{N/10^6} \cdot 10\,\mathrm{K\,s}^{-1}$ to account for heating due to noise on the electrodes which contain the plasma.

Successful collisional deexcitation of H^* and $\overline{\mathrm{H}}^*$ (Section 8.3.1) is expected to require a plasma containing at least 100 million electrons, at a comparable density and a much lower temperature ($T \lesssim 50\,\mathrm{K}$) compared to that measured for $N = 115 \cdot 10^6$. Since at least half of the heating appears to come from plasma expansion, this is will be the key parameter to optimize in future experiments. A factor of ten reduction would be consistent with what has been achieved in other Penning traps. This will require careful trap alignment; in particular the Cusp magnetic field is different from a solenoid in that it has only one axis along which $dB/d\theta = 0$. The new cold bore will offer improved control over $x-y$ alignment as well as increased range and the possibility of displacing the electrode stack in the all three dimensions (see Section 8.2.4). The heating due to noise on the electrodes may be reduced by using electrodes with a greater aspect ratio (length/radius)—which reduces the effectiveness of adjacent electrodes at stimulating plasma modes—and by improving the electrode cabling by switching to twisted pair wire with lower resistance than the stainless steel coaxial cable used presently. Both of these changes will be implemented in the coming month (see Section 8.2.1).

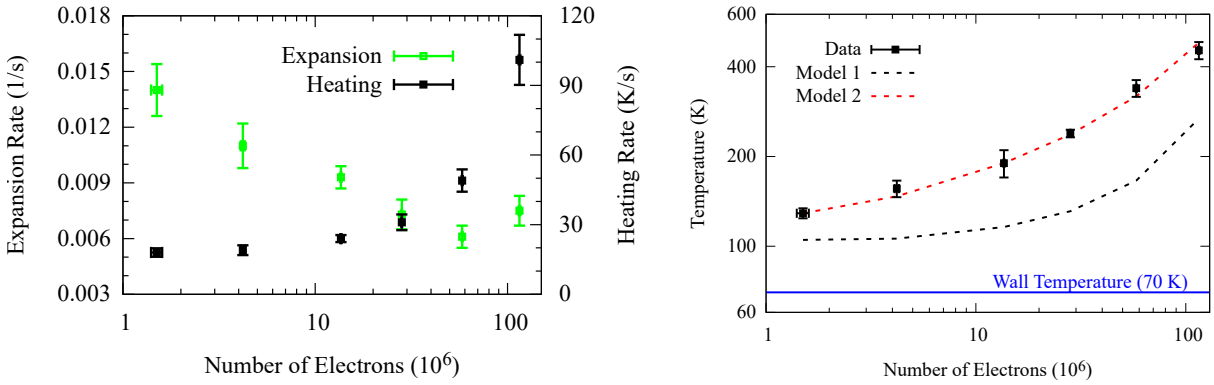

Figure 16 – Expansion rate and heating due to expansion (left) and final temperatures (right) for plasmas containing $1 < N < 120$ million electrons. Data points represent the mean and standard deviation of three trials at each value of N. Heating due to plasma expansion is calculated following Ref. [121]. The temperatures on the right are compared with Model 1, which only accounts for heating due to plasma expansion, and Model 2, which adds a term proportional to $\sqrt{N}$ (see text).

8.1.2 SDREVC

The spin-flip measurement envisaged by the ASACUSA collaboration requires a beam of $\overline{\mathrm{H}}$ having kinetic energy $E \leq k_B \cdot 50\,\mathrm{K}$ [122]. As a point of reference, the ALPHA collaboration routinely produces about 20 trappable $\overline{\mathrm{H}}$ per mixing cycle in a magnetic bottle of trap depth $k_B \cdot 0.5\,\mathrm{K}$. Assuming a thermal $\overline{\mathrm{H}}$ distribution of $T = 40\,\mathrm{K}$ [123], this extrapolates to over 1000 $\overline{\mathrm{H}}$ with $E \leq k_B \cdot 50\,\mathrm{K}$. Thus, a mixing protocol similar to the one described in Ref. [123] could be a viable option for producing the $\overline{\mathrm{H}}$ required by ASACUSA.

Precise and above all reproducible control over plasma parameters is essential for optimizing the mixing protocol. The SDREVC technique developed in 2017 [124] permits control of plasma parameters (such as radius, length, temperature, and density) at the level of 1%. Prior to the development of SDREVC, the number of trappable $\overline{\mathrm{H}}$ produced in a typical ALPHA mixing cycle was not 20 but 1. SDREVC stands for evaporative cooling (EVC) in the Strong Drive Regime (SDR). The SDR rotating wall, developed by Danielson and collaborators [125], fixes the plasma density n at a value which is linear in the applied rotating wall frequency. Simply put, the RF perturbation generates a torque proportional to the difference between the plasma rotation rate $\omega_r \approx \rho e/2\epsilon_0 B$ and the drive frequency, so that these two frequencies match at equilibrium.

From the expression for ω_r one may wonder whether SDR compression is possible in ASACUSA's Cusp Trap, where the magnetic field B typically varies by 50% or more over the length of the plasma. In experiments performed this year with electrons, it was found that the Cusp Trap does in fact support SDR plasma compression, over a broad range of plasma parameters. Fig. 17 reports the estimated density ρ for electron plasmas containing $N = 14 \cdot 10^6$ particles, having length $L_p = 7.5\,\mathrm{cm}$, and spanning a magnetic field range $0.9 < B < 1.6\,\mathrm{T}$. The plasmas were compressed for 30 s using a $3\,\mathrm{V_{pp}}$ perturbation applied to the 4-segment, 3 cm long, 4 cm radius rotating wall electrodes in the Cusp Trap. Similar results are obtained at higher density and higher rotating wall frequency for plasmas containing $N > 10^8$ electrons.

By slowly lowering the electrostatic confinement voltage on one or both sides of the plasma, one may reduce the plasma space charge ϕ_0 and temperature T [126]. This procedure, known as EVC, can result in significant plasma expansion. However, in combination with simultaneous SDR compression, the same procedure yields a plasma with well defined ρ, ϕ_0, T, and by extension

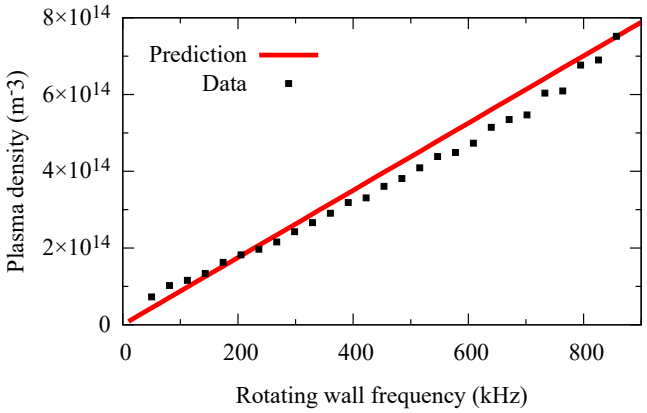

Figure 17 – Linear dependence of plasma density on rotating wall frequency, indicating successful SDR compression for $N = 14 \cdot 10^6$ electrons. The plasma density is calculated assuming the plasma is a right circular cylinder with a constant length $L_p = 7.5\,\mathrm{cm}$. The predicted equilibrium SDR density (see text) is given for $B = 1.26\,\mathrm{T}$, which is the magnetic field value close to the plasma's axial center.

radius and length, r_p and L_p. The resulting plasma is fully defined—independent of variations in initial conditions due, for example, to electron source hysteresis, slowly evolving trap and gas temperatures in the positron accumulator, or instability in the number of antiprotons delivered by the AD.

Figure 18 reports the implementation of the SDREVC technique in the ASACUSA Cusp Trap. The final state of the plasma, summarized in Table 2, is independent of how many electrons are initially loaded, provided that the initial number of particles $N_i > N_f$, the final number of particles. These measurements were taken about 100 ms after restoring plasma confinement and turning off the rotating wall perturbation. If the plasma is left in the trap an additional 10 s before being extracted, the temperature T falls to $227 \pm 4\,\mathrm{K}$ for the entire range of N_i studied. This demonstrates control over r_p, T, and N at the level of 1%, 2%, and 3%, respectively.

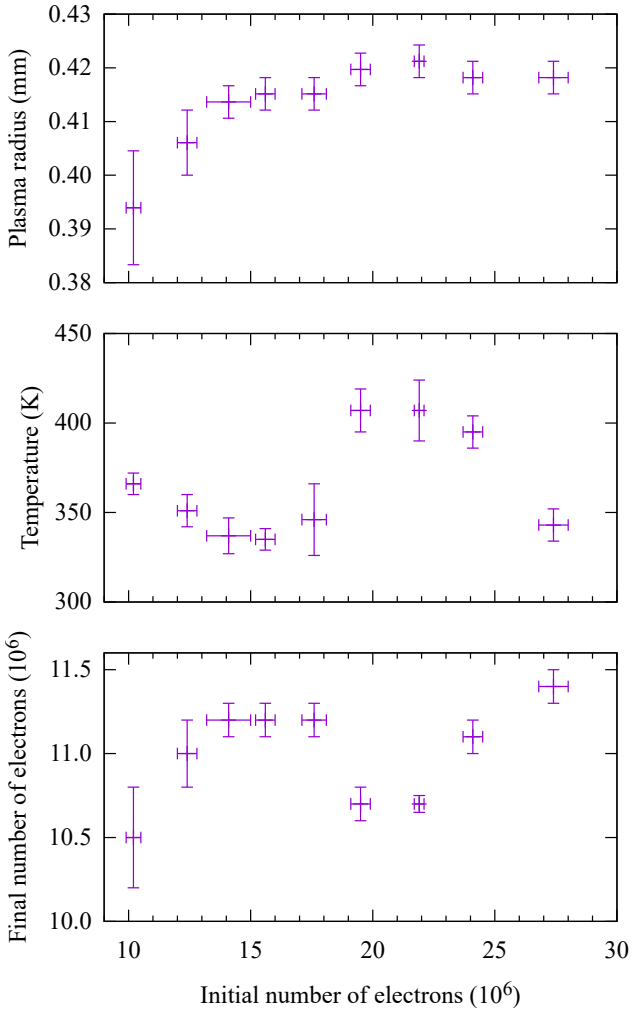

Figure 18 – Plasma properties immediately following SDREVC: radius, temperature, and number of electrons measured using fast dump with charged MCP (imaging mode), slow dump with charged MCP (Tdiag mode), and fast dump with MCP at 0 V (Faraday Cup mode), respectively.

Property	**Mean**	**SD**
r_p (mm)	0.417	0.003
T (K)	360	30
N_f (10^6)	11.0	0.3

Table 2 – Weighted averages and standard deviation, using the subset of data in Fig. 18 for which $N_i > N_f$ (i.e. excluding the first of nine points). If the plasma is allowed to cool for 10 s before proceeding, the standard deviation in T falls from $30/360 = 8.2\%$ to $4/227 = 1.8\%$

To our knowledge this is the only demonstration of SDREVC in a strong magnetic mirror field. The Cusp Trap has two regions where rotating wall compression can be done. For the measurements reported above, the upstream region was used. It is also possible to perform SDREVC in the downstream region, in the well shown in Fig. 19. In this case, particles are pushed out of the well in both directions (this has been confirmed by using an electrode far away on the upstream side to block escape in that direction. Doing so reduces particle loss during EVC by roughly half). This implies that the downstream plasma edge is within a few k_BT of the first magnetic field null of the Cusp Trap. The resulting plasma parameters are, nevertheless, similar to those obtained from performing SDREVC in the upstream region, and quite reproducible. Unfortunately, it was soon demonstrated that a nearby electrode (U3) is not connected. A small (< 10 V) floating potential

on U3 should not compromise the foregoing observations. However, since it adds unnecessary uncertainty, further studies were postponed until February, when the trap will be replaced (and rewired).

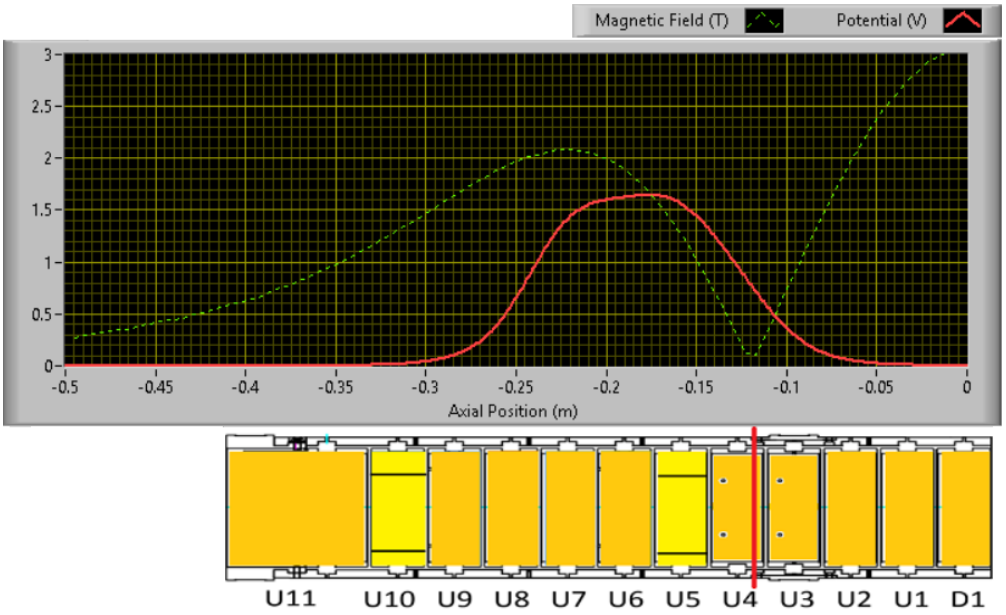

Figure 19 – Magnetic field and final electrostatic potential for electron SDREVC under the downstream rotating wall electrode U5. Electrode names and z-aligned cross sections are also shown for reference. During the EVC procedure, the well bottom starts at about 8 V and is pushed down to 1.6 V as shown. Particles escaping from such a well necessarily have enough energy to reach the field null. Despite the large magnetic field gradient, SDR compression and SDREVC have been achieved in this configuration.

8.1.3 Positron Results

As described in section 8.1.1 and 8.1.2 the temperature as well as a reproducible number, and density for the e^+ plasma are crucial for $\overline{H}$ production. Hence, we are working towards SDREVC for positrons. Although we have not achieved this yet, we have improved the properties of the plasma by optimizing the accumulation, transfer and catching by the Cusp trap.

A lifetime measurement was performed to see how long and how many e^+ we can accumulate in the positron accumulator at different N_2 pressures, shown in fig. 20. One can see that with decreasing pressure the lifetime of the e^+ in the trap increases. The activity of the source was 277 MBq on 2020.05.01. We achieved a maximum of approximately 3.5 million e^+ in this measurement by waiting for roughly 2 minutes, which is a reasonable accumulation time, as it is about the time of one AD cycle.

The CGC instruments AMX500-3 triple analog switch/multiplexer, which pulsed the blocking potential at the accumulator for extraction, was replaced by a homemade HV pulser which is based on the second and third stage of the design in [127]. This pulser has four times lower noise and a faster rise time. Exchanging the pulsers, with no other changes, immediately decreased the bunch length of the e^+ cloud at the Cusp entrance by a factor of 2.7, as shown in Fig. 21. After reducing the beam energy from 150 V to approximately 75 V, the pulse width increased to 160 ns, which we reduced to 50 ns by optimizing the transfer potentials in the accumulator.

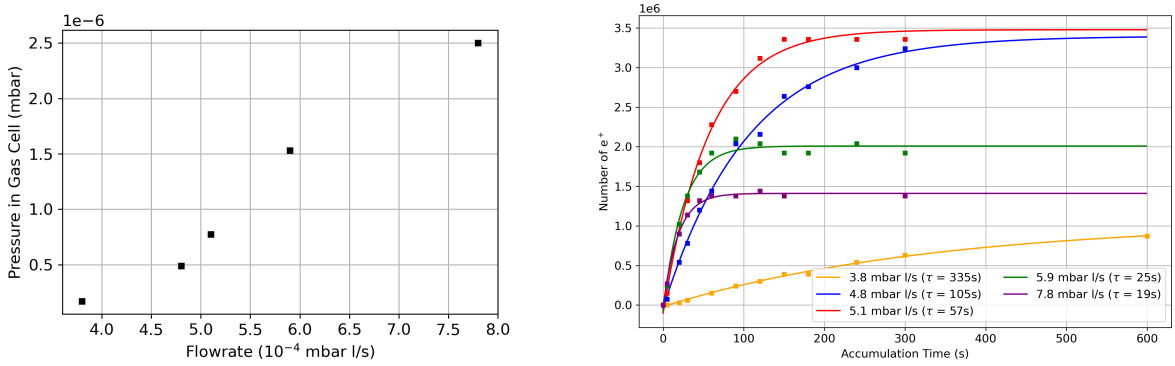

Figure 20 – N_2 pressure in the gas cell of the accumulator dependent on the set flowrate (left). Number of e^+ as a function of accumulation time at different N_2 pressures. The points were fitted (dashed lines) by $a + b(1 - e^{-x/\tau})$ to calculate the lifetime τ at the corresponding pressures.

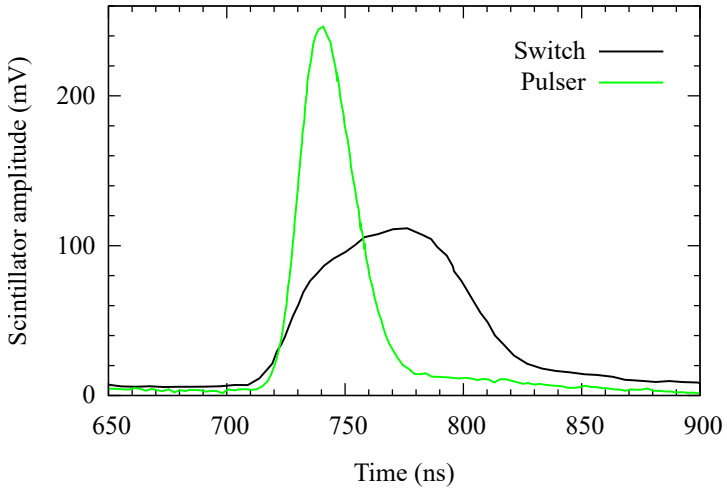

Figure 21 – Scintillator signal due to annihilation of the e^+ cloud on the Cusp MCP, using the old pulser ("switch", black) and the new pulser ("pulser", green). The FWHM was reduced from 80 ns to 30 ns. Time is measured relative to the extraction trigger, which causes the pulser to fire. The black curve has been offset by −500 ns to facilitate comparison. The cause of the extra delay with the old pulser has not been investigated.

In table 3 the catching efficiency of the Cusp trap after 30 s and 60 s accumulation time is listed. We started the run with about 300 thousand e^+ after 30 s accumulation time at the Cusp entrance which we could increase to about 1.4 million e^+.

	30 s	60 s
Accumulator	2.18M e^+	3.82M e^+
Cusp	1.45M e^+	2.16M e^+
Efficiency	65%	56%

Table 3 – Catching efficiency of the Cusp trap.

Due to a problem with the downstream coldhead of the Cusp trap, the temperature was higher

than previously. This lead to a worse vacuum and as a consequence the expansion rate of the e^+ cloud was high. The positron plasma radius increases linearly in time, doubling within 57 s after RW compression. The ability to control the cloud with the RW was therefore limited.

We measured a cooling curve of the plasma after applying RW for 20 s (3 MHz, 4 V) and a heating curve after additionally cool for 8 s and apply EVC for 100 ms, shown in Fig. 22. Equation (7) shows the theoretical change of the temperature in time, where T_i the initial temperature, T_W the wall temperature of the Cusp trap, H the heating rate and G the cyclotron cooling rate (values used are shown in table 4), which fits the measured data points, so the temperature evolves reasonably. Additionally, it is shown in the heating curve in fig. 22 that we can perform EVC with positrons.

$$T(t) = T_W + \frac{H}{G} + \left(T_i - \left(T_W + \frac{H}{G}\right)\right) e^{-Gt} \tag{7}$$

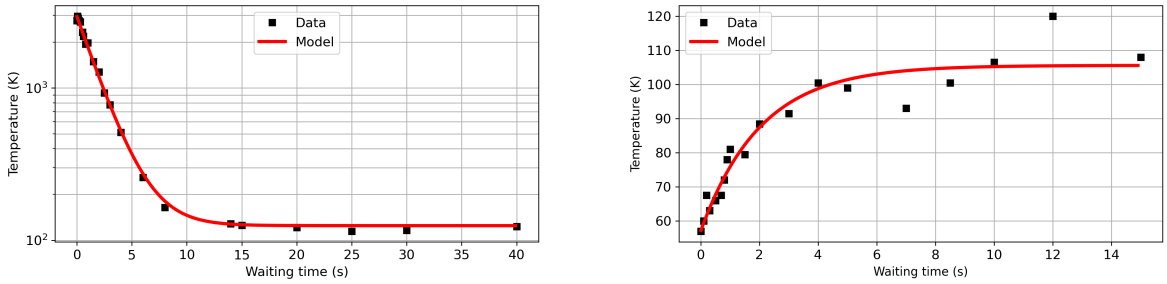

Figure 22 – Cooling curve of the e^+ plasma after applying RW for 20 s (left) and heating curve after applying RW for 20 s, cool for 8 s and EVC for 100 ms (right). The model data were calculated by equation 7. The values used to produce the model curve are shown in table 4

Property	Cooling Curve	Heating Curve
T_W	70 K	70 K
T_i	2960 K	57 K
H	27 Ks^{-1}	17 Ks^{-1}
G	0.49 s^{-1}	0.49 s^{-1}

Table 4 – Values used in the model to calculate the cooling and heating curves of Fig. 22. T_i is the measured initial temperature, T_W the measured wall temperature of the Cusp trap, G the cyclotron cooling rate and H the resulting heating rate.

8.1.4 Experiments with Positive Ions

Normally, the Cusp Trap vacuum is maintained at a negligibly low level ($p < 10^{-10}$ mbar) via cryopumping on the 15–20 K trap walls. During the summer, the downstream coldhead failed and had to be stopped. The upstream coldhead then had to work more than twice as hard because it was fighting an increased heat load. The electrode temperature subsequently rose and stabilized at about 70 K. In this environment it is easy to generate positive ion clouds by running an electron beam over a shallow negative potential well. In 30 s over three million ions could be produced and

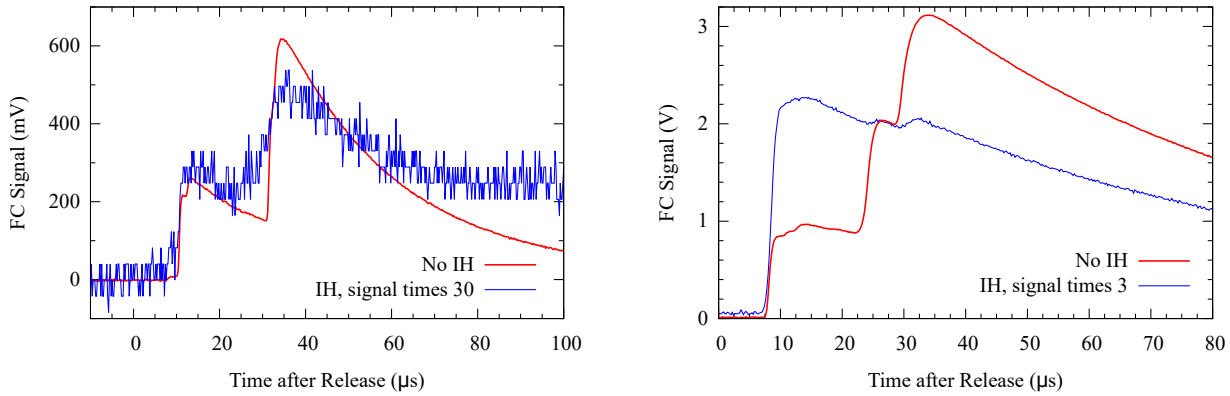

Figure 23 – Reduction of contaminant ions using the autoresonant drive. Left side: 30-fold reduction of ions in the presence of 10^6 positrons. No positrons were lost in this operation; for the data shown, positrons were afterward removed with an e-kick to make it possible to resolve the small ion population. Right side: 300-fold reduction of heavier ion species, leaving 86% of the lightest ion (H_2^+) in the well.

trapped. The ion clouds were used to develop mass-selection routines, diagnose the trap vacuum, and perform ion cyclotron resonance (ICR) magnetometry.

The z-motion of an ion in an electrostatic potential $V(z)$ is periodic at the bounce frequency $\omega_z \approx \sqrt{(q/m)\partial^2 V/\partial z^2}$. Anharmonicity in $V(z)$ produces corrections which typically make ω_z a decreasing function of the bounce amplitude. In this situation autoresonance can be used to remove all ions with mass greater than a threshold $m_{th} \sim 2q\,\partial^2 V/\partial z^2/\omega_{start}$, where ω_{start} is the start frequency of a negative frequency sweep [128]. By applying a 1 V chirp to the upstream confinement electrode, it is possible to remove either all ions (leaving positrons behind) or, if desired, all but the lightest ion species (when no positrons are present). See Fig. 23.

The drive reduces the species fraction of the target ions by at least a factor of 30 compared to the non-targeted particles (continuous generation of ions in the well during and after the heating procedure is not excluded in the present vacuum conditions; this may be reducing the apparent removal efficiency). Such a procedure is necessary for removing contaminants from positron plasmas. It could be useful in future experiments involving the proton source, which generates H_2^+ and H_3^+ along with the H^+ (see Section 8.1.5).

The cyclotron cooling rate for charged particles of mass M is $0.26\,\mathrm{s}^{-1} \cdot B[\mathrm{T}] \cdot (m/M)^3$, where m is the mass of an electron. For ions, such cooling is negligible on any reasonable timescale. Any cooling that does happen is necessarily mediated by collisions, either with positrons or with residual gas (see Fig. 24). The latter measurements were taken after removing all heavy ions, as described in the previous paragraph. The H_2^+ velocities may then be estimated from the measured temperature. Taking the measured cooling rate as equal to the hard-scattering collision rate $n\sigma\langle v\rangle$, with $\sigma \approx 3 \cdot 10^{-19}\,\mathrm{m}^2$ for typical diatomic collisions [129], one can estimate the background gas density as $n \approx 2 \cdot 10^{13}\,\mathrm{m}^{-3}$. The asymptote of the cooling curve indicates that the ions are colliding with something with temperature $T < 200\,\mathrm{K}$; the most reasonable assumption is residual gas in equilibrium with the trap walls at 70 K. The corresponding pressure $p = nk_BT \approx 2 \cdot 10^{-8}\,\mathrm{Pa}$ or $p \approx 2 \cdot 10^{-10}\,\mathrm{mbar}$.

The downstream region of the MRE is currently being redesigned, for installation in May 2021 (Section 8.2.4). The new design includes two field ionizers (FI) (Section 8.2.2), to be located at the two field nulls of the Double Cusp magnet, each with a 2 mm gap between the grids. Since the FI positions are locked to the MRE, a method is required for determining the z position of the MRE

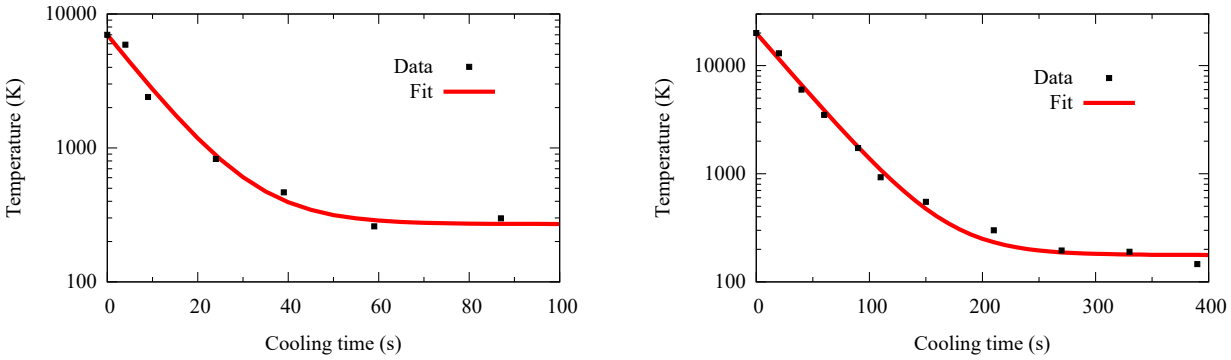

Figure 24 – Cooling curves for positive ions formed from residual gas. The data on the left was obtained for ions generated during the positron catch. These ions are cooling sympathetically via collisions with the positrons, at a rate $0.1\,\mathrm{s}^{-1}$. The data on the right was obtained for ions generated using an electron beam. These ions cool via collisions with the (non-ionized) residual gas in the trap, at a rate $0.03\,\mathrm{s}^{-1}$.

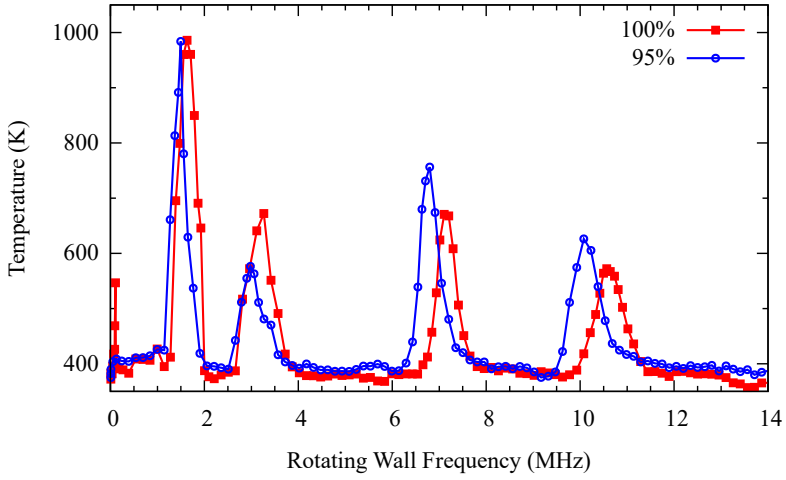

Figure 25 – Ion cloud temperature as a function of the frequency of the applied rotating wall perturbation, for two values of the Cusp magnetic field. Temperature data has been averaged using a 4-point rolling mean. The centers of the four largest peaks match the cyclotron frequencies of N^+, the first harmonic of N^+, H_3^+, and H_2^+ for a magnetic field $B = 1.3\,\mathrm{T}$. These four frequencies shift down by $6.1 \pm 2.3\%$ when the current in the Cusp magnet is reduced by 5%.

with respect to the magnet. To this end, preliminary measurements have been made using positive ions heated at the cyclotron frequency $\omega_c = qB/M$ via $\sim$1 MHz rotating wall perturbations. See Fig. 25. This technique, known as ion cyclotron resonance (ICR) magnetometry, permits *in situ* measurement of the Cusp magnetic field. The accuracy is presently limited to $\sim$1% because the positive ion clouds cover a large spread in B, both radially and axially.

Figure 26 shows a set of lineshapes obtained from ICR scans where the ion cloud was in six different axial locations (z, with $z = 0$ corresponding to the center of the Double Cusp magnet). The scans extend from 10 kHz to approximately 2 MHz. The x-axis of the data shown in Fig. 26 has been rescaled for all but the -25 cm data set such that the heating peaks overlap. These scaling factors should be proportional to the ratio $B(z)/B(z_0 = -25\,\mathrm{cm})$. By comparing the ratios so obtained with the expectations, for different choices of z_0, one can determine a best-fit z_0 and

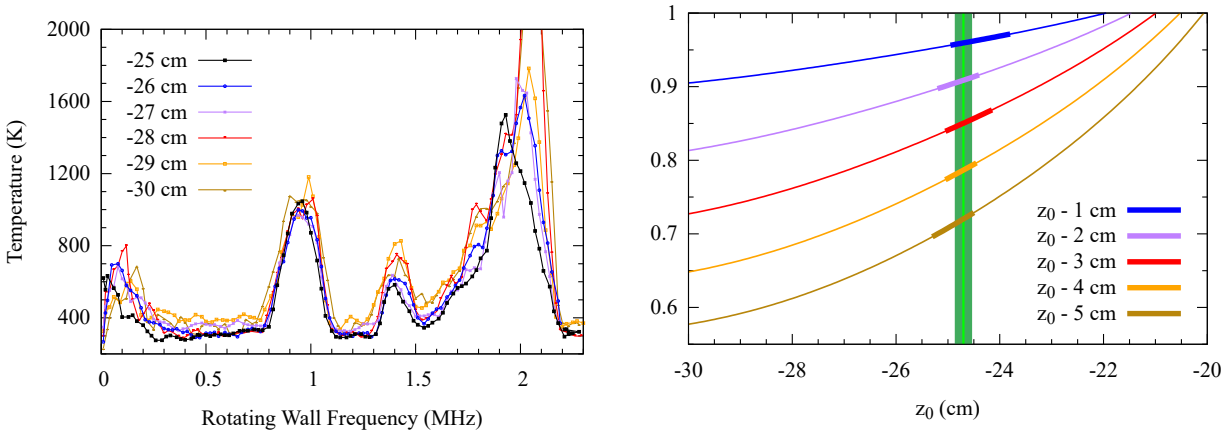

Figure 26 – ICR spectra (left) and determination of trap position (right). The ICR frequencies have been rescaled such that the heating peaks overlap. The scaling factors determine the ratio of the magnetic field at the respective locations, which are given in the legend. Comparing these ratios to the known magnetic field profile of the Cusp trap provides information about the position of the electrodes, which fix the plasma position, with respect to the magnet. The rightmost graph gives the field ratios as a function of z_0, with the lighter lines showing predictions and the darker bands indicating in each case the range of B-ratio values consistent with the data in the left graph. The vertical green bands give the estimated true z for what should be $z = -25\,\text{cm}$, with uncertainties shown in dark green.

thereby determine the relative offset of the Cusp electrodes from their nominal location. The results of this analysis are shown in the right side of the figure. The data is consistent with an axial offset of $3 \pm 1.4\,\text{mm}$ compared to perfect alignment.

The FI's will be sensitive to changes in z position at the level of 1 mm. In fact the dependence of the ionization rate of formed (anti)hydrogen atoms, as a function of FI position, could provide information about the underlying angular momentum distribution of the (anti)atoms. The measurements presented above may be further improved by using a colder, denser ion sample (as is expected from the proton source) or, if necessary, by repeating these measurements with electrons.

8.1.5 Development of a low energy proton source

As described in the 2020 SPSC report [130], a low energy proton source has been developed in order to enable matter mixing experiments within the Cusp trap [131]. Briefly, the source generates protons using electron impact ionisation of H_2-gas. The source consists of three separate modules: the electron gun creates the electrons using a heated tungsten filament which are then focused into the second module, the gas cell trap, using an anode. The gas cell is a mechanically compensated Penning trap. The axial confinement is provided by two flat endcap electrodes and a four-fold segmented ring electrode which allows the application of a RF. Radial confinement is provided by 32 permanent neodymium rod magnets assembled in a stack (16 around the gas cell module, and each 8 around the electron gun, and the ion extraction module). The final module for ion extraction, is used to focus and steer the proton beam into the Cusp trap. It consists of a flat entrance electrode, a four-fold segmented ring electrode (also referred to as deflection plates or steerers), and a cylindrical exit electrode. The source can create either a continuous or a pulsed beam of protons with variable energy.

In order to characterise the source before the installation into the ASACUSA-experiment, a test-setup was built at the Stefan Meyer Institute. It consisted of the source and a MCP delay-line

detector mounted opposite it, this enabled the measurement of the number and position of ions produced. This detector will also be used as part of the matter mixing experiments on the Cusp to detect protons and excited hydrogen produced on the downstream side of the Cusp.

Initially, moving and focusing of the ion beam was tested. For this the source was put into a continuous mode of operation. In this mode as the name would suggest, the ions are continuously extracted after their production by a ramp electrical potential created in the gas cell module. Figure 27a shows that by adjusting the potential of the deflection plates, the beam spot on the

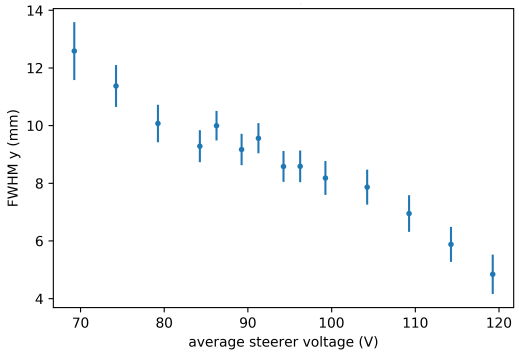

(a) Reduction of the FWHM of the beam spot (in y coordinate) on the detector depending on the potential applied to the deflection plates showing focusing of the spot.

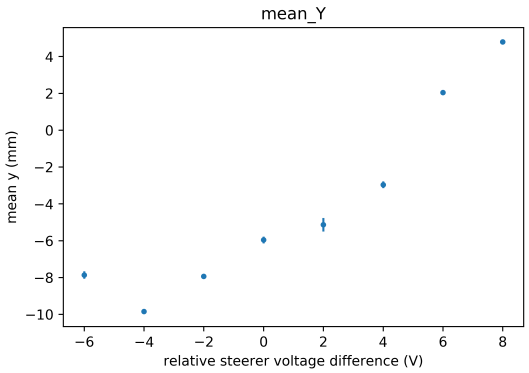

(b) Mean position of the beam spot on the detector (in y coordinate) depending on the voltages applied on two of the deflection plates showing deflection of the beam.

Figure 27 – Focusing and deflection of the proton beam spot

detector can be focused to a smaller point. In order to steer the ion beam, different voltages can be applied to each of the deflection plates. Figure 27b shows the mean position of the beam-spot on the detector in the y-coordinate. By adjusting the potential of one of the electrodes up, and the potential of the opposite electrode down, the beam-spot can be moved across the detector.

As, not only protons can be produced via electron impact ionisation of H_2, but also H_2^+, and later on H_3^+ through collisions of H_2^+ and H_2 [132], identification of the ions leaving the trap is important. This was achieved by operating in a pulsed extraction mode and utilizing time-of-flight ion spectroscopy. For this the the gas cell module is operated in a 'trapping-mode' i.e. an electric potential well is created in the gas cell. For the extraction pulse, the potential on the entrance electrode is increased and on the exit electrode decreased thus, creating a potential ramp and

extracting the ions out of the gas cell.

The three peaks in the time-of-flight spectrum in figure 28 were identified to be H^+ at ≈ 4.1 μs,

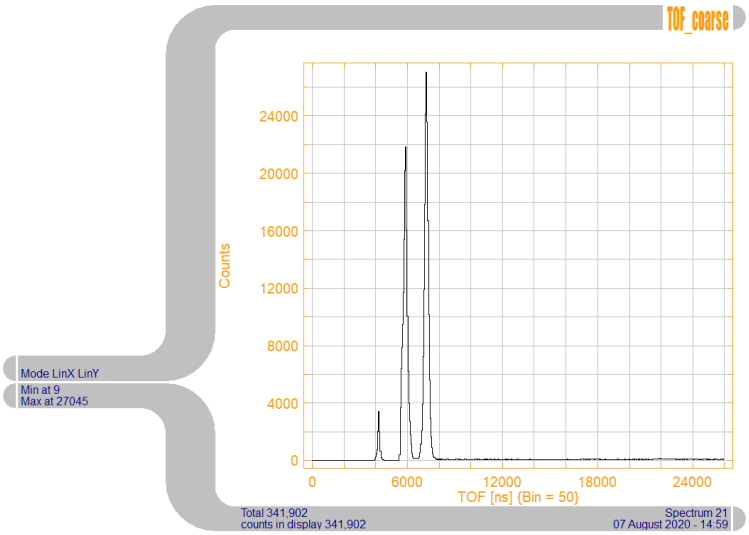

Figure 28 – Time-of-flight spectrum for pulsed operation

H_2^+ at ≈ 5.75 μs and H_3^+ at ≈ 7.05 μs. As can be seen in the time-of-flight spectrum, the number of protons created, is approximately one order of magnitude lower than the number of H_2^+. This is as expected from their respective cross-sections [133].

In order to increase the number of protons produced, both sideband cooling [134] and the rotating wall technique [125] were tested. The application of sideband radio frequency pulses increased both the number of protons leaving the source but also their lifetime in the trap. However, the number of H_2^+ and H_3^+ ions was still significantly higher in this mode. Similar results were obtained for rotating wall pulses in direction (90°, 0°). The maximal lifetime of protons in the trap measured for both these modes was approximately 1.65 ms.

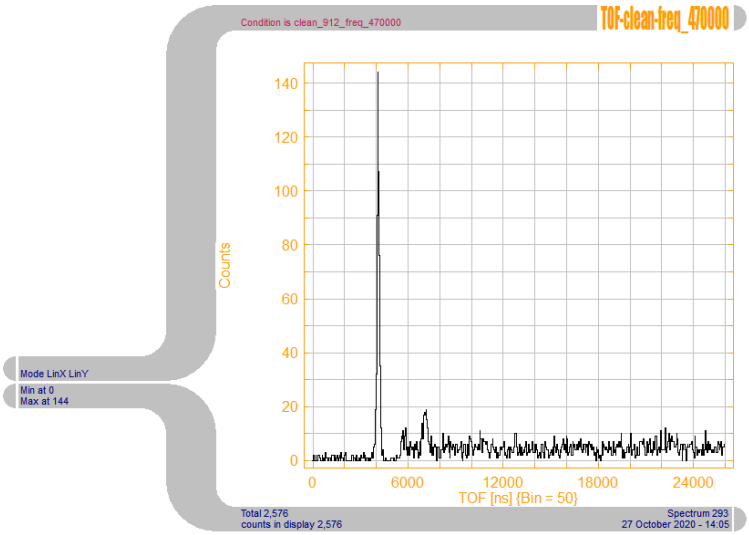

Figure 29 – Cleaned time-of-flight spectrum at 0.47 MHz rotating wall frequency

However, when applying the rotating wall pulses with the opposite phase (0°, 90°), a small proton peak formed at ≈ 0.47 MHz rotating wall frequency, and more importantly, the number of H_2^+ and H_3^+ ions were reduced by two orders of magnitude. This can be seen in the time-of-flight spectrum in figure 29 where the proton peak, although still small, dominates over the H_2^+ and H_3^+ peaks.

As can be seen from the data in figure 29 the number of protons leaving the source per second is very low, this is by design so as not to damage the MCP detector when characterising the proton source. The electron filament was operated at it's 'turn on' current i.e. at the point it started to emit an electron beam. Increasing this to it's operating current, and improving the transport properties from the gas cell by adjusting the ion energies we estimate around 2 million protons per second can be delivered by the source with a contamination level of half a million H_2^+ and H_3^+ ions. The proton source and MCP detector will be shipped to CERN and installed into the ASACUSA experimental area in January 2021. It was hoped that this device would be ready to ship earlier in 2020 however, due to the ongoing global pandemic this was not possible.

8.2 Future upgrades and work in progress

8.2.1 New Cusp Multiringed Electrode Trap

We have designed and built a new CUSP multiring electrode trap, which is more suited for handling plasmas and forming an antihydrogen beam. A schematic cross section of the electrode configuration is shown in figure 30. The trap consists of in total 20 electrodes. Ten electrodes (labeled upstream electrode in in figure 30) define the mixing region, i.e. were the positron and antiproton plasmas will be brought together. These electrodes have an inner diameter of 34 mm. Two of the electrodes are azimutally segmented into four parts, which allow us to apply rotating wall compression [125].

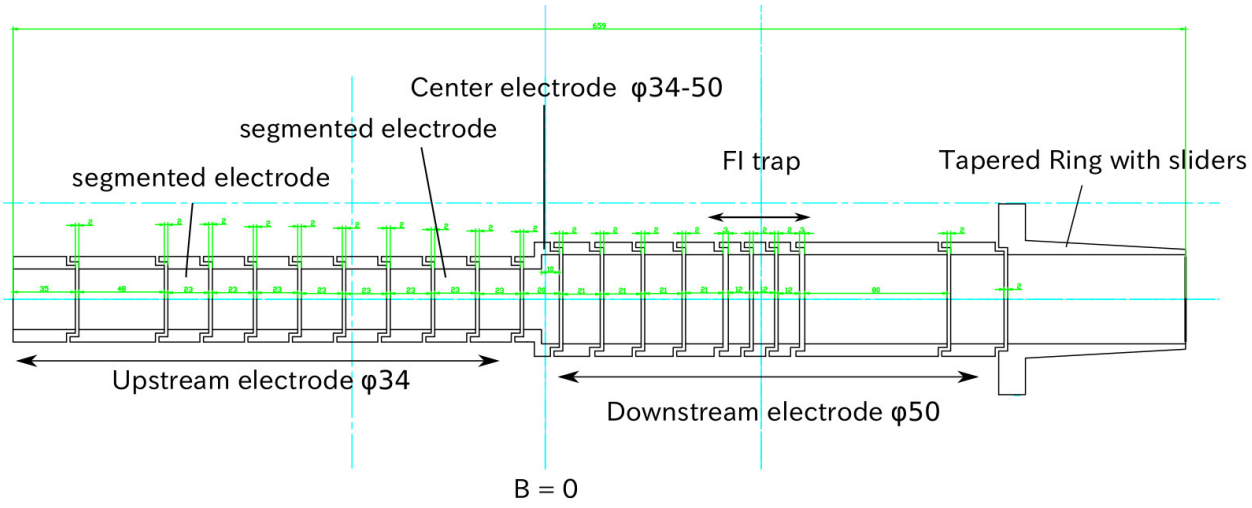

Figure 30 – Schematics of the new CUSP multiring electrode trap

The remaining ten electrodes (labeled downstream electrodes) have an inner diameter of 50 mm. Their higher diameter ensures that they do not obstruct the solid angle of the trap exit for the antihydrogen atoms leaving the mixing region. They include two field ionizers (FI), to be located at the two field nulls of the Double Cusp Magnet, each with a 2 mm gap between the grids.

The electrode stack was built in Japan and is already at CERN. Figure 31 shows a photo of the electrode stack assembly. It is forseen to install the MRE in early 2021.

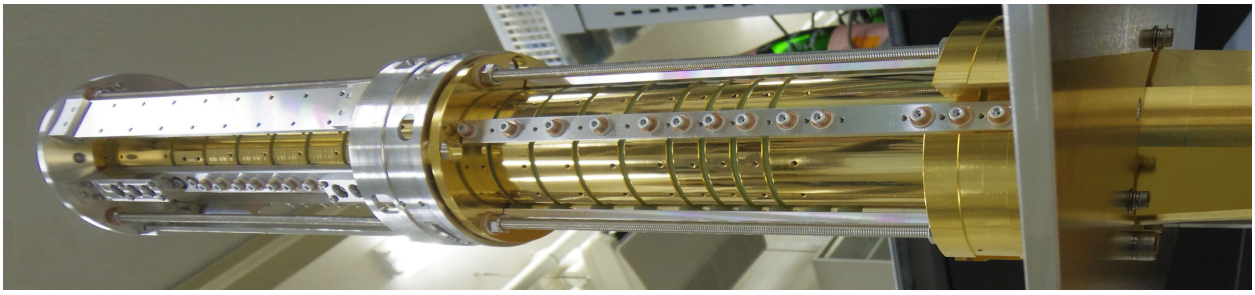

Figure 31 – Photo of the new CUSP multiring electrode trap

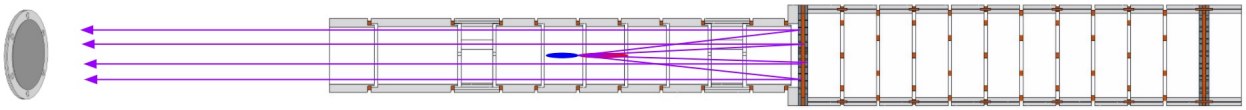

Figure 32 – Cartoon of the mixing process and subsequent ionization in the proposed upstream field ionizer. In general the paths will be curved rather than straight, due to the gradients in the Cusp field. Because ionization occurs at the field null, the resulting (anti)protons should be focused on their way to the MCP detector (left), rather than taking straight line paths as shown. In addition, many high field seekers will be deflected to the trap walls before reaching the ionizer.

8.2.2 Double Internal Field Ionizer

In order to continue improving the mixing routines in the absence of antiprotons, ASACUSA intends to perform mixing experiments using matter, that is, protons and electrons. The mixing of proton and electron plasmas will form excited hydrogen atoms, many of which are relatively easy to ionize. In the coming upgrade (Section 8.2.4), a pair of field ionizers (FI) will be installed immediately downstream of the mixing region, as shown in Fig. 32. The FI's will be located at the two field nulls of the Double Cusp magnet.

Including a full gridded FI close to the trapping region has one major advantage: the solid angle is much greater than for the external FI used previously. As shown in Fig. 33, roughly 1% of lfs (anti)atoms with magnetic moment between 1 and 25 μ_B are expected to reach the upstream FI. Hfs (anti)atoms are deflected by the Cusp field, so that relatively fewer of these are expected to reach the analyzers. Together, the yield for n-state analysis will be increased by at least an order of magnitude with these FI's, permitting much faster optimization of the mixing procedure.

In addition, the use of two ionizers should permit a time of flight measurement, from which the velocity distribution of the formed (anti)atoms may be derived. Briefly, the idea is to maintain the downstream FI constantly at full potential, while pulsing the upstream FI to zero for 0.2 ms out of every 2 ms. These numbers are, approximately, the time that an (anti)atom would take to fly from the upstream FI to the downstream FI if it were moving at 1000 m/s (100 K) or 100 m/s (1 K), respectively. The time of flight distribution may then be reconstructed from the resulting ion signal originating from the downstream FI.

8.2.3 Plasma detector upgrade

As the current plasma detector is not ideal for the plasma imaging and temperature measurement needed to implement SDREVC as described in 8.1.2, we plan to install a new plasma detector. The detection will be achieved by a Hamamazu single stack MCP with an active area of 40 mm. The MCP will be coupled with a phosphor screen with a fast decay time of 80 ns. The light from

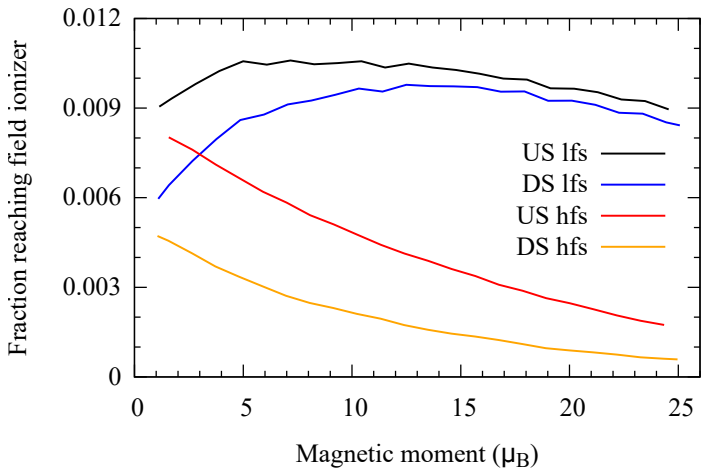

Figure 33 – Fraction of (anti)atoms expected to reach the upstream (US) or downstream (DS) FI following formation at $z = -26\,\mathrm{cm}$, depending whether the atoms are formed in low field seeking (lfs) or high field seeking (hfs) states. This data comes from trajectory calculations in the Cusp magnetic field. The curves represent averages over initial kinetic energy $0.4 < E < 4.4\,\mathrm{meV}$ ($5 < T < 50\,\mathrm{K}$) and emission angle $0 < \theta < 15^o$ with respect to the axis of the Cusp magnet.

the phophor screen will be redirected downwards to an optical port by an mirror installed at a 45 degree angle. Figure 34 shows a rendering of the new detector. The MCP is already acquired and at CERN, while the mirror and the parts for mounting are currently under construction at the workshop of the Stefan Meyer Institute in Vienna.

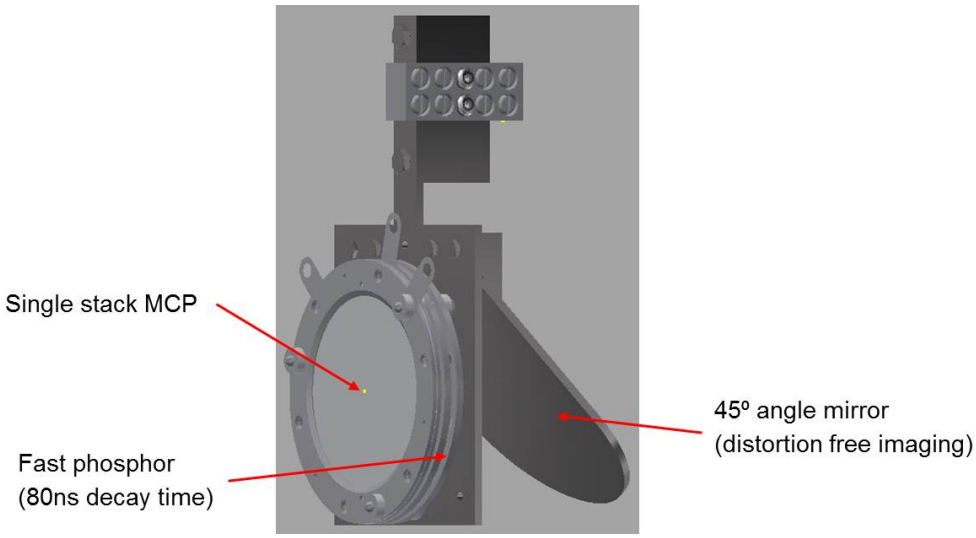

Figure 34 – Outline of the new plasma detector.

8.2.4 Cold Bore Replacement

In addition to the MRE upgrade discussed in section 8.2.1 and in line with section 5.3.1 in the 2019 proposal [108], work is underway to upgrade the cold bore of the Cusp trap. This upgrade was planned with a view to improving the temperature of the electrode stack, which in the present system is at best 15-20 K at the point of measurement. However, as mentioned above in section 8.1.3, due to a malfunctioning cold head the present temperature is closer to 70 K making this upgrade all the more essential. Figure 35 shows a render of the new design, here we will briefly describe the main differences between this new concept and the existing apparatus [135].

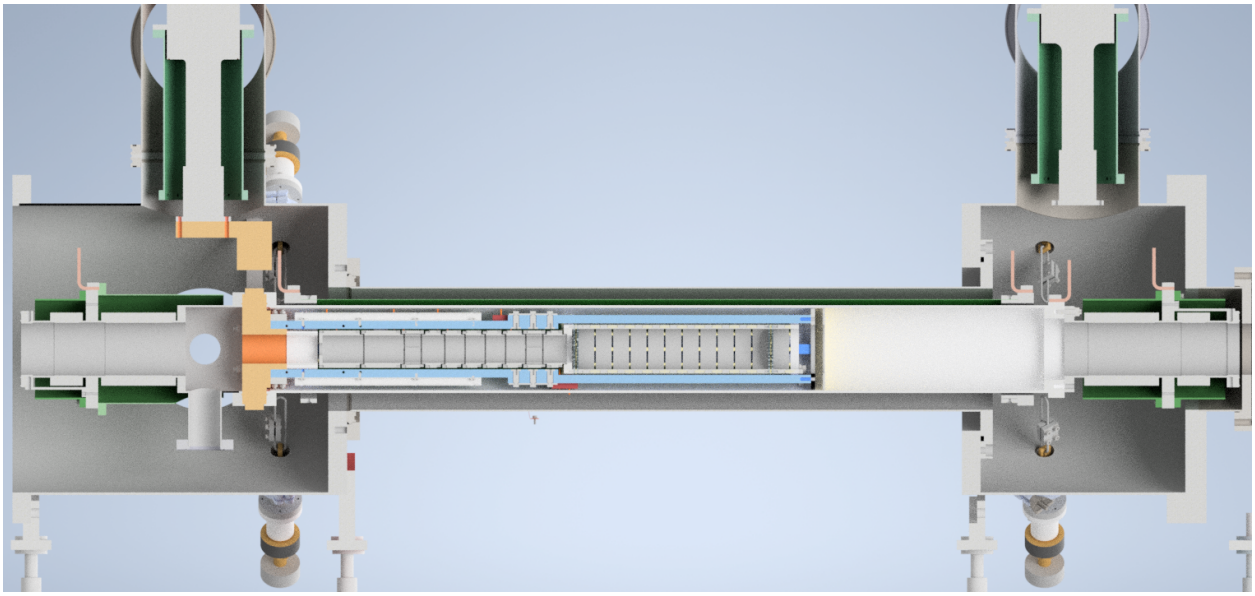

Figure 35 – Render showing 3D drawing of the new cold bore design. Green regions are heat shields connected to the 40K stage of cryocoolers. Blue bars are 5N Al rods connected to the primary copper flange (shown in copper colour). Left hand side (LHS) connects to the antiproton trap MUSASHI and positron trap, right hand side (RHS) connects to spectroscopy beam line.

Cooling will be provided by two Sumitomo Gifford-McMahon (GM) type cryocoolers: on the upstream side (LHS of figure 35) a model RDE-418D4 which provides 1.8 W of cooling at 4 K on the second stage and 42 W of cooling at 50 K on the first stage. On the downstream side (RHS of figure 35) a model RDK-408D2 providing 1 W at 4 K and 40 W at 43 K on the first and second stages respectively. These replace the two Iwatani HE15 GM cryocoolers currently in use.

The present design separates the cold bore from the electrode stack such that to cool the electrodes, a good thermal contact must be made with the inner diameter of the inner vacuum tube at two cold points. Using this method, there is a compromise to be made between the ability to insert the trap into the bore, and making a good thermal contact. The method used at present is a combination of multilam band springs and mechanical wedges which can be put in place after the trap is inserted. The new design incorporates the electrode stack as the heart of the cold bore. A large block of oxygen free copper will connect to the second stage of the upstream cold head. It is on this flange that the entire multi-ringed electrode stack is constructed. In this way, we no longer rely on contacting the electrodes to the correct part of the bore tube, instead the electrodes connect directly to the cold head (see figure 36).

Thermal and electrical connections to the electrodes are made via cryogenic filters that are

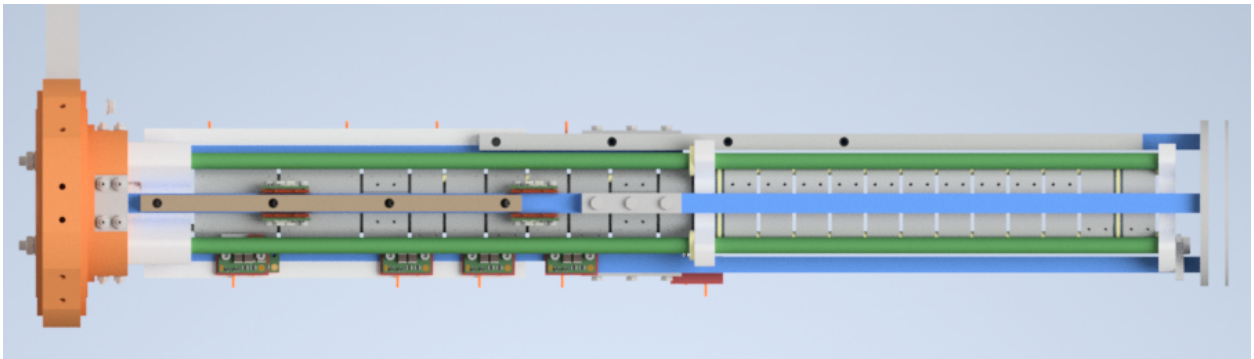

Figure 36 – Render showing 3D drawing of the new electrode stack. Blue parts are 5N aluminium rods which connect directly to the primary copper flange. Green Al rods support the electrodes stack. Conduit for wiring is shown connected on high purity Al bars which connect to the electrodes via the filters.

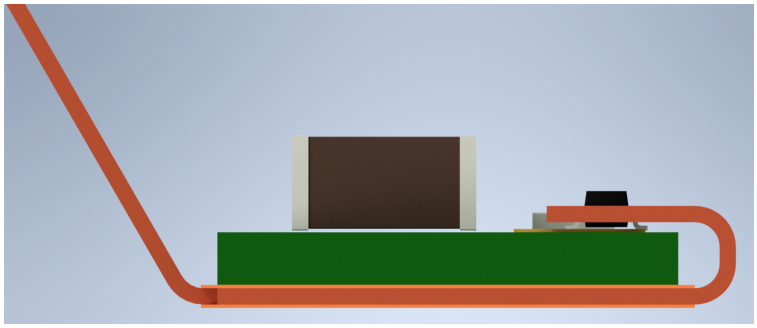

Figure 37 – Render showing 3D drawing of the new cryofilter design. The green layer is the G10 circuit board, the connection to the electrode is insulated from the bottom ground by two kapton sheets shown in the light orange copper colour.

mounted on the 5N purity Al rods which in turn connect directly to the primary copper flange. A side view of the new filter design is shown in figure 37. The filter is connected to the electrode via a thin sheet of oxygen free copper that covers it's entire footprint. The copper sheet is sandwiched between two thin kapton foils which provide electrical insulation from the group plane on the base of the circuit board and the high purity aluminium bar. The copper strip is then securely connected to the electrode providing good thermal contact.

The electrode stack is housed within an inner vacuum chamber (IVC) which is constructed from an aluminium tube (ID=102 mm thickness=3 mm). A challenge with this type of system is the connection to room temperature vacuum tubes at the entrance and exit of the bore. This is necessary to allow in charged particles on the upstream side for mixing, and the antihydrogen beam to exit on the downstream side. The present system makes use of bellows which is also the case here, however instead of one bellow between the 30 K stage and room temperature, a staggered bellow system will be used connected at 4 K, 40 K and finally to 300 K these can be seen on the upstream and downstream sides of the bore in figure 35. In addition to the bellows, on the upstream side there is an extra chamber which will allow cabling to be extracted from the trap through the insulation vacuum to the laboratory. Cabling is fed through conduit to provide shielding from electronic noise with only a short section exposed to connect to the filter (see figure

36).

Like the existing system, there is a heat shield around the IVC and the cold fingers connected to the 40 K stage of the cryocoolers. Further to this, extra heat shielding is added around the connections to the room temperature regions. The IVC is housed within the outer vacuum chamber (OVC) which provides an insulating vacuum and space to wrap super insulation around the 40K heat shield.

Once installed, the trap will need to be aligned with the magnetic field of the Double Cusp magnet, at present movement from manipulators in the laboratory is translated through the insulation vacuum to the cold bore via large blocks of plastic (POM) [135]. In the new design we have chosen to remove these large blocks and replace them with a number of Kevlar ropes which will have a far lower cross-sectional area for thermal conductance, we have also chosen to include manipulation not just in the X and Y plane, but also in Z such that we can align the trap precisely in the field *in situe* using the new magnetometary techniques (see section 8.1.4)

The design phase for this new cold bore has finished, manufacturing and testing will begin at the Stefan Meyer Institute in Vienna in early 2021. It is hoped that it will be installed at CERN no later than June 2021 however due to the uncertainty caused by the ongoing global pandemic this may have to be revised.

8.2.5 Positron Trap Upgrades

As discussed in section 5.3.3 of the ASACUSA proposal [108], the existing positron trap will eventually be replaced with a trap previously located at Aarhus University of the type manufactured by First Point Scientific. This has the advantage that it removes the need for our regular liquid helium deliveries to cool the magnet and bore of the existing trap. It also improves the safety during installation and removal of the source.

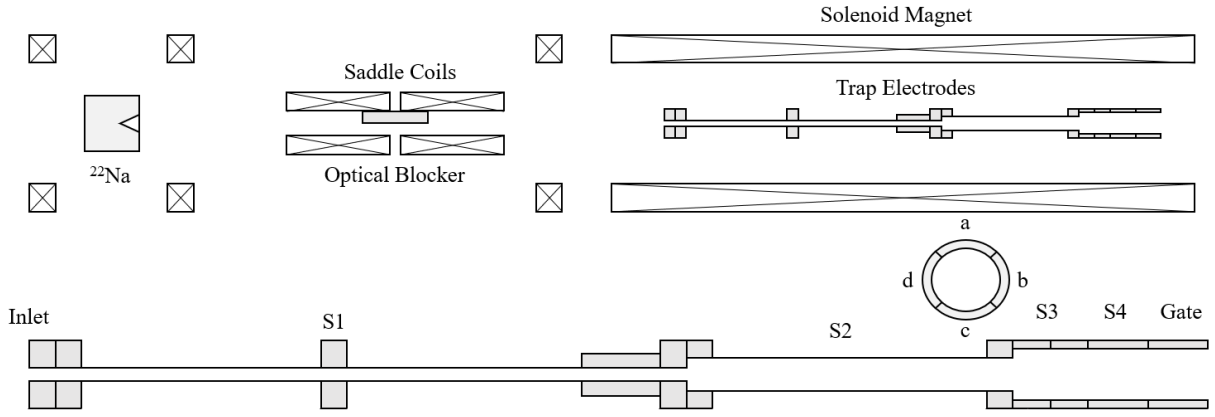

Figure 38 – Schematic diagram showing the layout of the moderator and trap, and a detail view of the trap electrodes. Split rotating wall electrode inset.

A schematic diagram of the trap electrodes and beam layout is shown in figure 38. The operation of this style of trap is described in detail elsewhere [136, 137]. Briefly, positrons from a ^{22}Na source are moderated by a layer of neon ice on a cone structure located in front of the source. Approximately 1% of the positrons that enter the ice are moderated and form the slow beam (upper limit 10 million per second with a 2 eV energy spread). The slow beam then navigates

a optical blocker which serves to remove a direct line of sight between the source and the trap. Positrons then enter the trapping region where a magnetic field of 500 Gauss serves to confine them radially and electrodes provide an electrical potential that confines the particles axially. Trapping of the DC beam is achieved, as is typical for positron trap, by collisions with N_2 gas. Unlike the existing system a rotating wall electric field is used to compress the particles stored in the S3-S4 region, for this an extra cooling gas e.g. SF_6 is used. Approximately 30% of positrons that enter the trap electrodes are confined, the others lost to positronium formation.

In 2020 the trap and source stage were shipped to CERN, the equipment is at present stored away from the AD hall in Bat. 15. As reported in the proposal last year, our plan was to prepare this for operation whilst using the existing trap for continuity. Due to the ongoing global Covid-19 crisis, bringing personnel to CERN to work on this apparatus was impossible. Hence, work has focused on the production of an accumulation stage.

One limitation of the device described above, in comparison with the existing trap, is the short lifetime for positrons. The present design can fill with particles for up to a few 100 s before extraction. Several of these bunches of positrons, consisting of many million particles, are then transferred to the Cusp trap for further manipulation [113]. The First Point Scientific trap has a lifetime of around 2 s in which time it will accumulate roughly a million positrons. As the trap is full of a high pressure of N_2 and CF_4 gases, transferring directly to the Cusp would be extremely detrimental to the vacuum. Hence, a new positron accumulation stage will be inserted between the positron trap, and the Cusp trap.

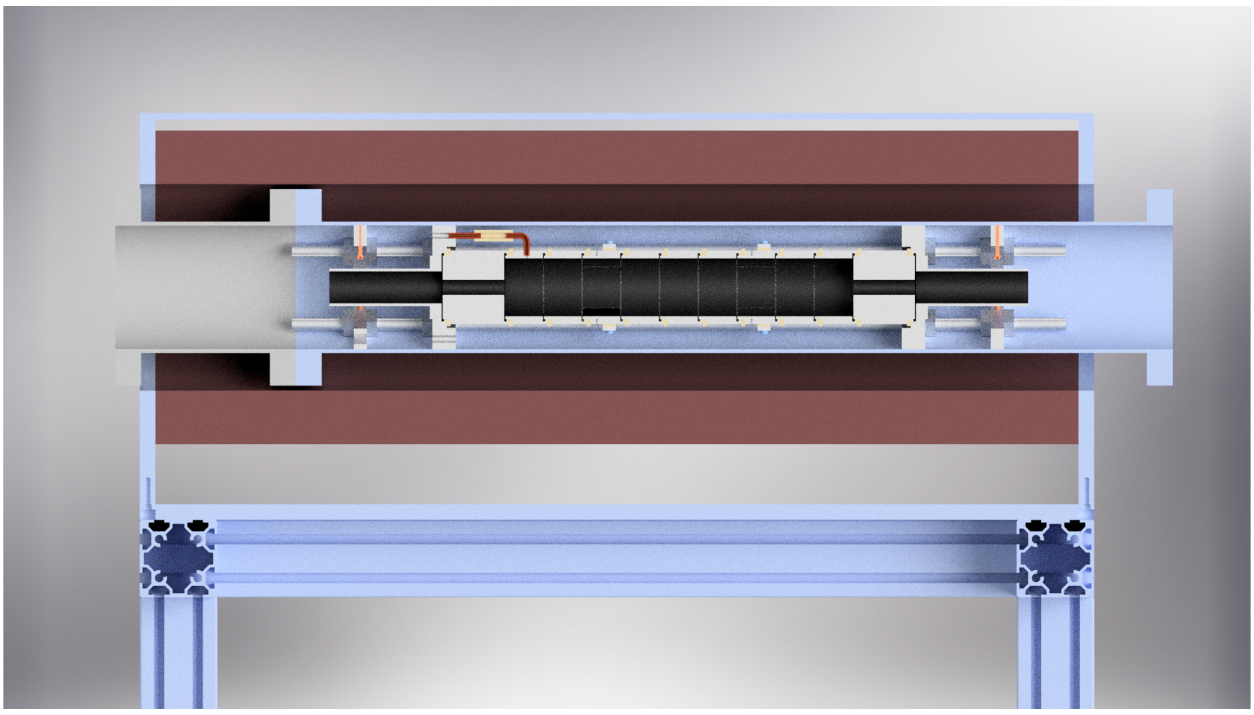

Figure 39 – Render showing 3D drawing of the new positron trap in the first coil of the positron transfer beam line. Positrons enter from the left and are ejected towards the Cusp trap on the right.

The new accumulator will be installed in an existing water cooled solenoid magnet (see figure 39) which is at present used during the positron transfer process, this can provide a field of up to 800 Gauss with a central uniform region ($\Delta B_z/B_z \sim 2.5\%$) of approximately 320 mm.

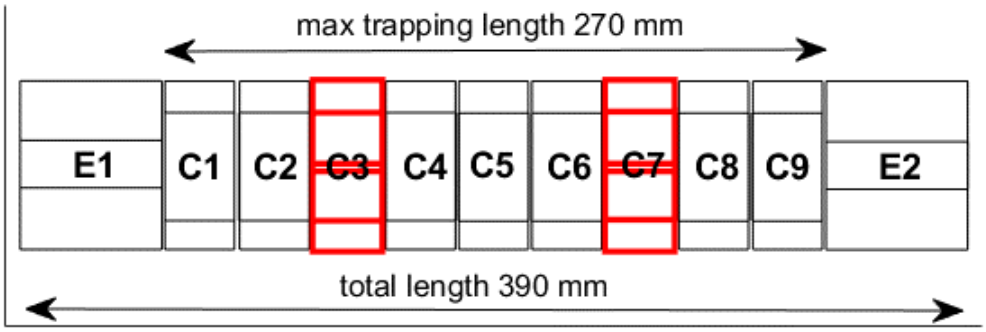

Figure 40 – Schematic diagram showing the electrode layout of the new accumulator. C3 and C7 highlighted in red show the location of split electrodes for applying a rotating wall electric field. E1 and E2 are earth tubes at the entrance and exit of the trap.

Figure 40 shows a schematic diagram of the electrode structure of the new device. Positron bunches from either trap enter via earth tube E1, a pulse is used to catch the bunch confining it between electrodes C1 and C9. The highlighted electrodes C3 and C7 are split to allow the application of a rotation wall electric field [125]. The trap is designed to be flexible such that new pulses can be caught while stacked positrons remain under compression (see figure 41), and to allow the bunching of particles before transfer to the Cusp trap for improved catching efficiency. This stage will store up to 100 million positrons in a single pulse ready to transfer to the Cusp trap when needed for mixing. Aside from improving vacuum conditions in the Cusp trap due to fewer transfers, another major advantage of this extra accumulation stage is that it can constantly be filled with positrons which are ready for transfer to the Cusp trap for mixing experiments. Hence, there is no need for stacking positrons in the Cusp increasing our efficiency of our mixing cycles.

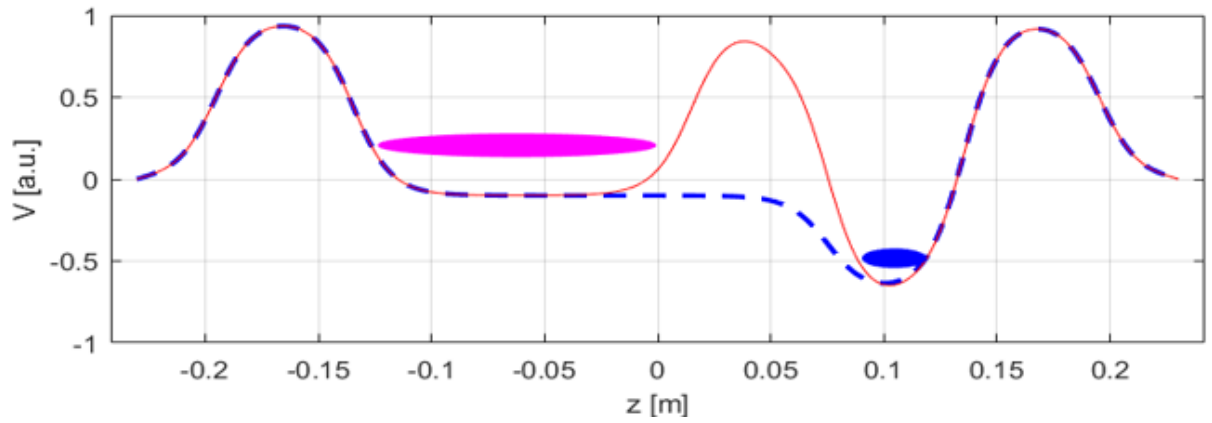

Figure 41 – Example catching (red) and storage (blue dashed line) potential, scale on potential axis is arbitrary.

The electrodes for the accumulator are now under manufacture in Milan and the device will be ready to install and test with the existing trap in spring 2021 when we hope that the conditions due to the global Covid-19 pandemic will have improved enough that travel is possible. Initially, the existing trap will be used to fill the accumulator while the new First Point Scientific trap is

tested. Should the ongoing global crisis cause problems with testing, then the new accumulation stage will be used with the existing trap during beam time in 2021, although this will require LHe to cool the existing magnet.

8.2.6 Upgrades to the MUSASHI antiproton trap and preparations for beam from ELENA

The ELENA ring will provide an intense antiproton beam with 100 keV of kinetic energy. The ASACUSA antihydrogen experiment will be located at the LNE05 transfer line. The ELENA transfer line and our antiproton trap (MUSASHI), are needed to be optimised for efficient capture of 100 keV beams.

The MUSASHI trap previously operated with the sequential combination of the AD, the RFQ decelerator (RFQD), and doubled 90 μgcm^{-2} BoPET degrader foils to capture $\overline{\mathrm{p}}$ beams. Ten Ag strips of 25 nm thickness and 940 μm width were printed onto each foil for the purpose of beam spot diagnosis. The "foil beam profile monitor" [138] was essential to steer and optimise injected beams for the highest $\overline{\mathrm{p}}$ trapping efficiency.

The Aarhus group's series of LEAR experiments and AD ASACUSA experiments [139–142] gives gives details about the thickness of a energy degrader foil required for a 100 keV beam. Our Monte-Carlo simulation suggests an Al foil with 1.1 μm in thickness. Commercially available foils have a 10% tolerance of thickness. An alternative calculation based on a recent theoretical study, including nuclear stopping power [143] suggests a 1.2 μm in thickness with 15% uncertainty may be more efficient. Using this simple foil solution one needs to apply high voltage to the foil to adjust incident beam energy to account for variations in foil thickness.

However, in this case, replacing the BoPET foil and beam profile monitor with a simple foil means that information about the beam spot at the trap entrance is lost.

An alternative solution has been studied which is to develop an accelerating drift tube to adjust the $\overline{\mathrm{p}}$ beam energy to be compatible with the existing BoPET foil beam profile monitor. A preliminary investigation of the design for a drift tube energy adjuster shows a ca. 70 cm long electrode will accept a bunch beam that is twice that of the ELENA design, i.e., 150 ns. A tube of this length fits the drift space after the hand-over point of the LNE05 (1.68 m). Figure 42 shows the simulated profile of a 120 keV beam on the BoPET foil after the drift tube, this energy is optimal for the present BoPET foil in the MUSASHI trap.

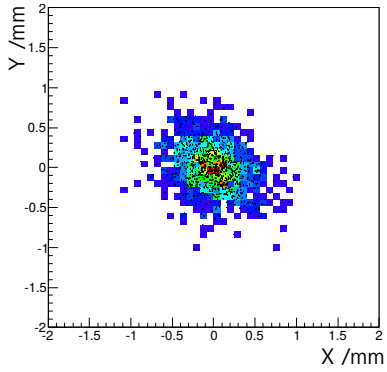

Figure 42 – Simulated profile of the 120 keV $\overline{\mathrm{p}}$ beam after the drift tube.

A new MRE design for the MUSASHI trap has been studied to allow parallel handling of antiprotons for efficient usage of ELENA beams. The trap will have two parts. One is for accumulation

and cooling of antiprotons, and the other for radial compression and extraction.

8.2.7 Upgrade of the scintillating bar detector

The detector consists of scintillating planes with a sensitive area of $\sim$1 m^2 placed along the Cusp trap to detect pions emerging from $\overline{\mathrm{p}}$ annihilations and providing annihilation position and time.

Each plane is composed by 90 cm long extruded scintillating bars with a cross section of 1.5$\times$1.9 cm^2 and a hole in the center to host WLS fibers. Fibers are then bundled and read out by a multi-anode PMT (see Fig. 43 on the left). As described in Sec. 5.5.2 of the ASACUSA proposal for ELENA [108], the light read out system will be upgraded replacing the PMTs with SiPMs. Each fiber will be cut, polished and read out by a single 1$\times$1 mm^2 SiPM with a setup similar to the one used in a previous detector used by the collaboration [87]. The analog signals from the SiPMs will be handled by the existing front-end electronic board based on the MAROC3 chip which presents a charge integrating input stage (for a more detailed description of the electronics see [144]): for this reason, the thermal noise of SiPMs could be an issue and preliminary tests have been performed to assess the feasibility of such a read out system.

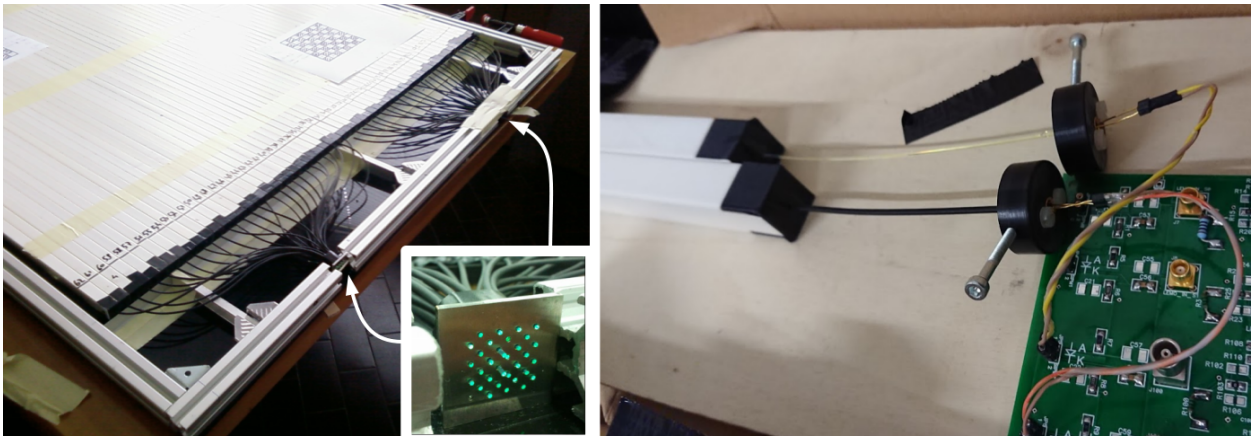

Figure 43 – Left: photo of the current scintillating bar detector internal layout where the WLS fibers are grouped into 2 bundles each one read out by a multi-anode PMT (not shown); right: detail of the experimental setup of the preliminary tests for the read out with SiPMs.

Two bars have been equipped with SiPMs (a detail of the setup is shown on the right of Fig. 43), placed between high resolution silicon microstrip detectors and exposed to cosmic rays to investigate their response. As shown in Fig. 44, the amount of scintillating light detected by the SiPM for a crossing MIP is around 15 times bigger than a single cell pulse of the SiPMs. This result ensures us that a SiPM read out with the present front-end electronics is feasible. The measured light yield has to be considered a conservative lower limit since in this test the polishing technique of the fiber has not been optimized yet and no optical grease has been used. Moreover, the used SiPMs present an older manufacturing technology with respect to the final purchased SiPMs (ASD-RGB1S-P-40 by FBK) for which an even lower dark count rate is expected.

The upgrade of the detector will start at the beginning of 2021 and will last a few months.

8.2.8 Schedule for 2021

Figure 45 shows an outline of the schedule for 2021. The year begins with hardware upgrades, this includes installing the new MRE described in section 8.2.1, proton source and detector described

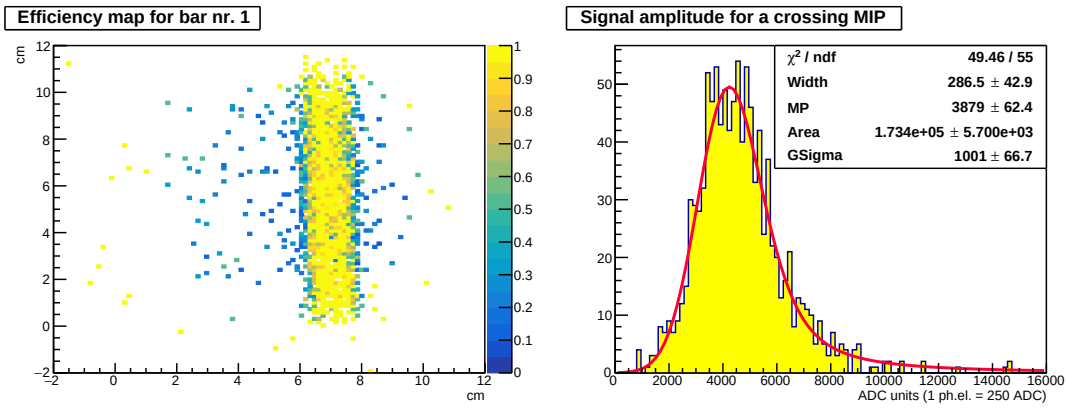

Figure 44 – Preliminary results of the test with cosmic rays and a single bar WLS fiber read out by a SiPM: on the left the obtained efficiency map is shown (only ∼10 cm of the bar length are hit by the particles triggered by the silicon microstrip detectors, see text), on the right the signal amplitude distribution for a crossing cosmic ray in units of ADC. As a comparison, in this condition the SiPM single photo-electron signal is around 250 ADC.

in sec 8.1.5, and the new plasma detector described in section 8.2.3. After this upgrade cycle,

Jan	Feb	Mar	Apr	May	June
Hardware Upgrades • MRE Upgrade • Proton Source Installation		**Matter Mixing** • Proton catching, cooling & compression • Electron cooling and compression • H Yield • n distribution		**Cold bore Upgrade** **Positron Accumulator Installation**	**Positron trap and accumulator optimization**

July	Aug	Sept	Oct	Nov	Dec
Matter Mixing • imaging • n-distribution • velocity distribution • Positron plasma → compression and cooling		**MUSASHI** • $\bar{p}$ catching & conditioning • Transfer of $\bar{p}$ to the Cusp	**Antimatter Mixing** • n-distribution • velocity distribution		
MUSASHI Upgrade for ELENA		**Cusp** • Positron plasma optimisation • $\bar{p}$ plasma optimisation			

Figure 45 – Chart shows schedule for 2021. Colour key– blue: work with hardware, green: offline experiments, orange: beam time.

experimental work will continue in the Cusp trap with electrons and the newly available protons. This will culminate in matter mixing and measurements of the yield and principal quantum number distribution of the hydrogen produced. In May and June the new cold bore (sec 8.2.4) and positron accumulator (sec 8.2.5) will be installed, and optimisation of trapping in the new accumulator will begin. The upgrade to the cold bore also sees the installation of the double field ionizer setup described in section 8.2.2. Experiments on matter mixing will continue in July and August, making

used of the double field ionizers to determine the velocity distribution. As this work is in progress the MUSASHI trap will be upgraded to operate with the 100 keV beams from ELENA (sec 8.2.6). If the present beam time schedule is maintained in late August, we will switch to antimatter operation using September to optimise MUSASHI for catching and conditioning antiprotons, and repeating our work in the Cusp trap. We would expect to spent the remainder of this year reproducing the results obtained during our matter mixing experiments with antimatter.

It's important to note that unlike previous beam times, the Cusp experiment will not be dismantled and moved due to the installation of the LNE05 beamline. This means we will begin 2022 in a much more favourable position than in previous years, with no need for serious realignment work or broken vacuum that needs to be reconditioned. If it is the case that due to unforeseen circumstances, it is not possible to receive antiprotons in 2021, then we will continue with matter mixing experiments for the remainder of the year. We will proceed to our beam time schedule in 2022 as soon as antiprotons are provided.

8.3 Antihydrogen beam deexcitation schemes

8.3.1 Collisional deexcitation of Rydberg states

As described in previous reports [130], we have investigated the use of an additional plasma between the mixing region and first null of the Cusp trap's magnetic field as a method of deexcitation. In this case, the Rydberg antihydrogen collides with an electron or positron resulting in the deexcitation of the atom.

$$\overline{\mathrm{H}}^{*} + \mathrm{e}^{+/-} \rightarrow \overline{\mathrm{H}}^{*'} + \mathrm{e}^{+/-} \tag{8}$$

where the internal energy is transferred to the electron or positron in the collision process. Going forward, as this is *relatively* simple to implement with existing hardware, this will be tested experimentally in 2021 firstly using matter and if successful implemented with antimatter.

8.3.2 Stimulated deexcitation of Rydberg states

As mentioned in section 7, one of the main points which was crucial to be addressed during LS2 is a path to the production of ground-state antihydrogen atoms. We have detailed, in the proposal submitted in October 2019 [108], the different options under investigation to achieve a lower n-state distribution. Since then we have finalized the theoretical investigations published in [145]. Our studies showed that the combination of THz radiation and a single laser at 832 nm has the potential to drastically enhance the ground-state population of an initial distribution of states with $n < 35$ within $\sim 50\,\mu$s. The fact that ground-state can be reached rapidly is important to increase the quality and polarization of the antihydrogen beam [146]. The use of microwave radiation, additionally to or instead of the THz light, can in certain cases improve the results further. The optimal choice depends on the initial state distribution of states which is not known precisely despite first experimental investigations [114]. It is planned to pursue the characterisation of the state population with matter (see section 8.1.5) and then with antihydrogen again as soon as ELENA starts operation. Theoretical work based on CTMC simulations shows that a high positron density ($\sim 10^{15}\,\mathrm{m}^{-3}$) will form antihydrogen atoms in states that are stronger bound so that, in these conditions a high fraction of atoms should have a principal quantum number $n < 35$ [147]. Consequently a large fraction of the formed antihydrogen are in reach of the proposed deexcitation method.

In collaboration with the Laboratoire Aimé Cotton in Paris, we have performed a first proof of principle deexcitation experiment using a beam of cesium atoms excited to Rydberg states. The

effect on the state population of a broadband lamp, emitting in the THz region, and a photomixer to induce a narrowband transition, was observed demonstrating the potential of such deexcitation techniques. The results, together with a review of the available THz light sources in the context of antihydrogen deexcitation, are published in [148], currently in press. Our next goal is to perform an experimental demonstration on hydrogen before application to antihydrogen. We have initiated the construction of a new hydrogen beamline using a second hydrogen source which was tested at CERN in the summer 2019. The details of the progress toward demonstration of fast deexcitation of hydrogen are discussed in the section below. We note that such a controlled formation of ground-state antihydrogen atoms could be used (if pulsed) to obtain information on the velocity distribution of the atoms formed, which is a crucial parameter for the hyperfine splitting measurement. In particular it would enable the velocity characterization of the atoms that are useful for spectroscopy (those in ground-state). Such an approach would be complementary to alternatives via, for example, field ionization in (see section 8.2.1) or at the exit of the CUSP trap.

9 Experiments with hydrogen and deuterium beams

In this section we give a brief summary of the progress with ASACUSA's parallel matter beam experiments in 2020 and on the plans for 2021. We refer to the proposal for the ELENA era [108] for detailed descriptions of the set-ups, previous achievements, and the medium-term program. The main purpose of these experiments are comprehensive characterisations of spectroscopy equipment and methods as well as developing techniques for fast and efficient deexcitation of Rydberg states. Due to the scarce availability of antihydrogen such studies have to use matter. As a side product self-contained precision experiments on hydrogen and deuterium are pursued, which will allow to put constraints on certain SME coefficients.

9.1 Progress at the excited hydrogen experiment

As discussed in the section above (§8.3.2), we plan on testing the envisioned antihydrogen stimulated deexcitation techniques on a beam of excited hydrogen. For this purpose a second discharge source, which was commissioned in 2019 (and has been described in the previous report to the SPSC [130]), has been equipped with its own microwave generator for independent operation from the source of the HFS set-up. Using this source, which was operated frequently and reliably in 2020, several paths were foreseen for the creation of an excited beam of hydrogen:

1. excitation of the hydrogen ground-state atoms to the 2s metastable state via electron collision followed by laser-excitation to Rydberg states
2. laser-excitation to Rydberg states of the 2s atoms formed in the discharge source
3. usage of the Rydberg atoms formed in the discharge source

In parallel to the development of the Ti:Sa laser for Rydberg excitation from the 2s state, necessary for the first two options, we investigated the Rydberg content of the beam produced by the discharge plasma in the source using field-ionization, in order to assess the feasibility of the third option. The upper part of Fig. 46 shows a sketch of the set-up including two metallic meshes connected to a high-voltage supply for electric field-ionization and a MCP to detect the atomic ionization rate (protons are accelerated toward the MCP). The plots show preliminary results obtained with the second source.

A signal at the MCP at low high voltage settings indicates the presence of Rydberg states in the beam. The observed rate is small, but certainly good enough for optimization and interesting from

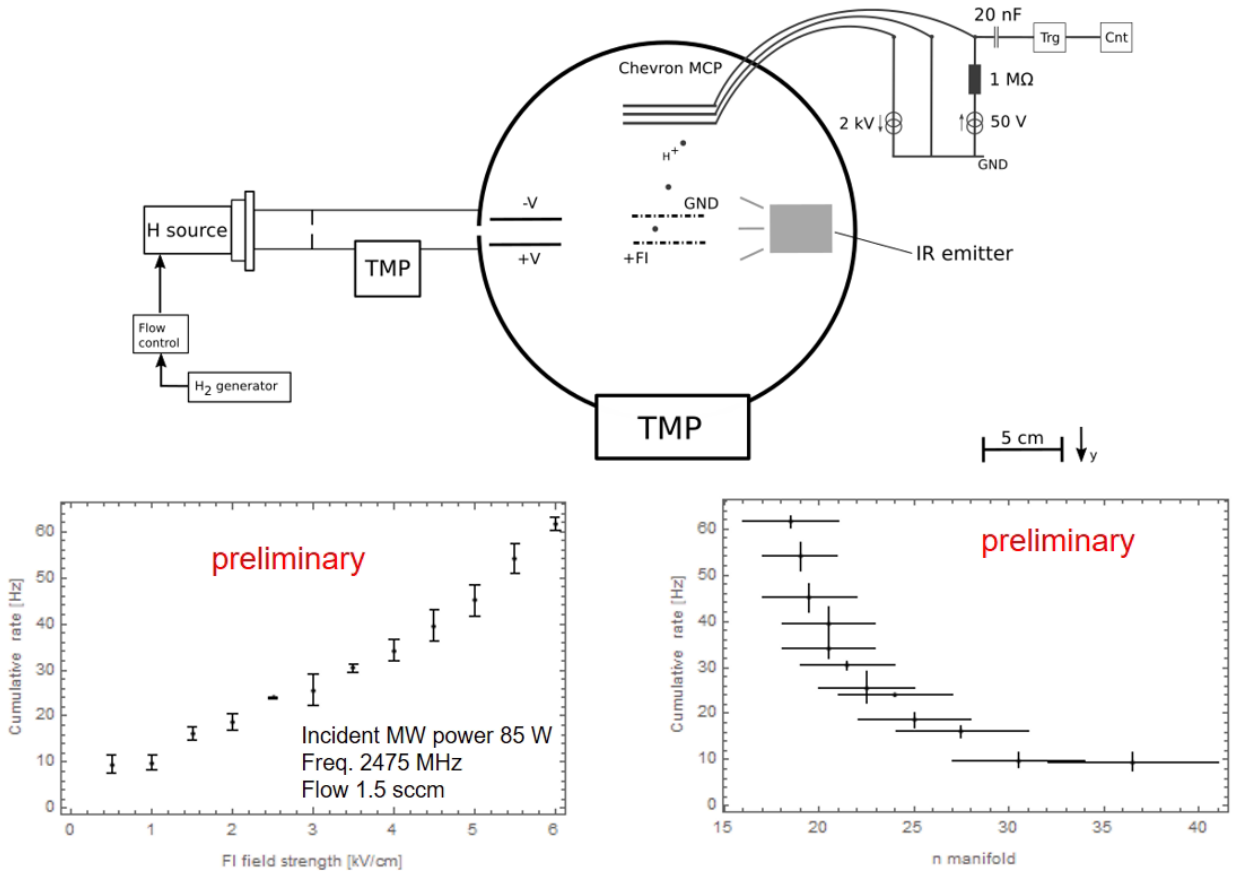

Figure 46 – Molecular hydrogen out of a commercial generator is dissociated within a microwave discharge plasma. The quantum state distribution of the emitted atomic beam is probed in a tunable electric field in the central region of the detection chamber. The ionization products (in this case protons) are detected with a standard MCP chevron stack. The plots show preliminary results indicating a Rydberg state production through electron collision and/or recombination within the plasma. With a gradually increased electric field strength stronger bound electrons ionize from the atomic H beam resulting in an increased proton detection rate at the MCP. The electric field strengths can be related to the ionized range of n-manifolds using standard hydrogenic field ionization theory.

a plasma physics point of view. To this extend a parameter scan of the source (power, frequency, H_2 flow) was performed and, in collaboration with the Laboratoire de Physique des Plasmas in Paris, we are working on determining the most important processes forming Rydberg hydrogen in the source to ultimately find ways to increase the Rydberg content of the beam. For this purpose, we have initiated simulations based on collisional radiative models for hydrogen plasmas [149].
In this optimization process, using a spectrometer as an additional plasma diagnostics tool, we identified that the second source is less efficient in producing hydrogen compared to the HFS source. Therefore it is planned to switch, early 2021, to a commercially available device based on an Evenson cavity design as shown in Fig. 47.

The first option to produce a Rydberg beam of hydrogen involves electron impact excitation in the first stage. The design of the electron beam was initiated in 2019 and reported in [130]. The apparatus, shown in Fig. 48 has been built and is now being commissioned at SMI.
The development of the Ti:Sa laser for Rydberg excitation has been pursued in collaboration with the Laboratoire Aimé Cotton. The laser is expected to arrive at CERN in January 2021. A new

Figure 47 – Evenson cavity that can be installed around a glass tube guiding the molecular hydrogen gas. The tunable cavity is operated at 2.45 GHz.

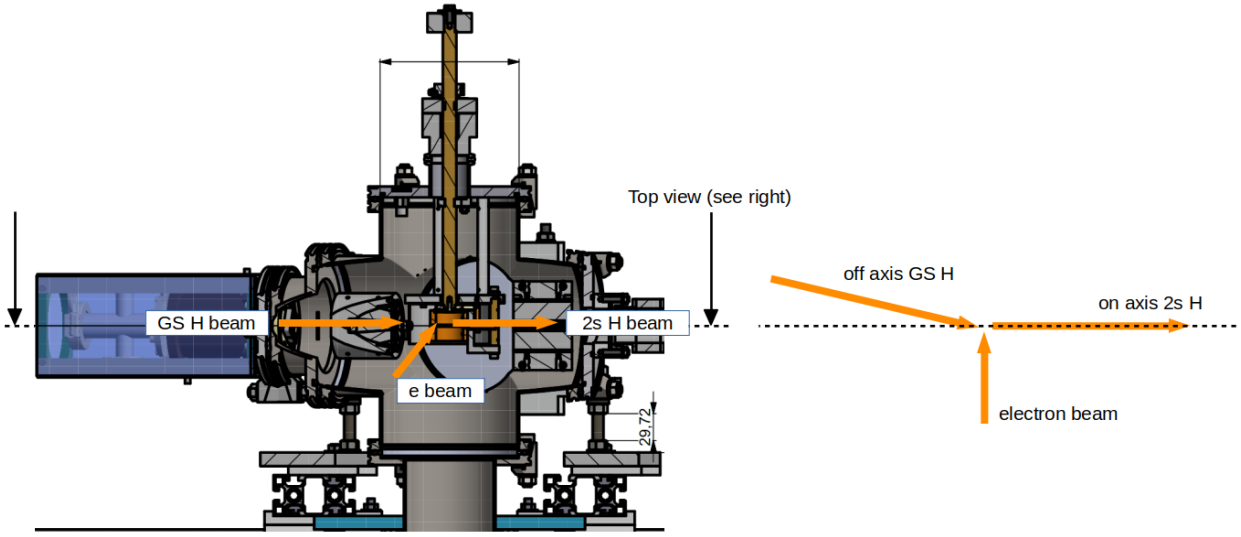

Figure 48 – The off-axis ground state hydrogen beam emitted by the discharge plasma is excited to the metastable 2s level via electron collision. Both the hydrogen and electron impact angle can be varied to optimize the 2s yield as a function of the excitation cross-section, electron and hydrogen kinetic energies, resulting 2s beam divergence and other parameters.

laser lab is currently being prepared in B275 to host the hydrogen deexcitation set-up together with the excitation laser.

The possibility to have both a broad range of Rydberg states populated via the discharge H_2 plasma (which resembles the initial antihydrogen state population via 3-body recombination) and a well defined Rydberg state population via laser excitation (which eases the study of the effect of the deexcitation techniques used) is an advantage for the further demonstration of efficient and fast deexcitation in hydrogen.

In parallel, other developments are being pursued and will be implemented in 2021 including further diagnostics of the hydrogen beam using Doppler spectroscopy and a thermal shielding to minimize the effect of the blackbody photons on the state population emitted by the plasma. Fig. 49 shows the deexcitation set-up to be installed in B275 in the coming weeks.

The first attempts to observe the impact of a broadband lamp and photomixer on the excited hydrogen beam is scheduled for the second half of 2021. In parallel, the deexcitation laser at ~ 832 nm will be developed and tested in combination with the THz sources. Section 9.4 summarizes

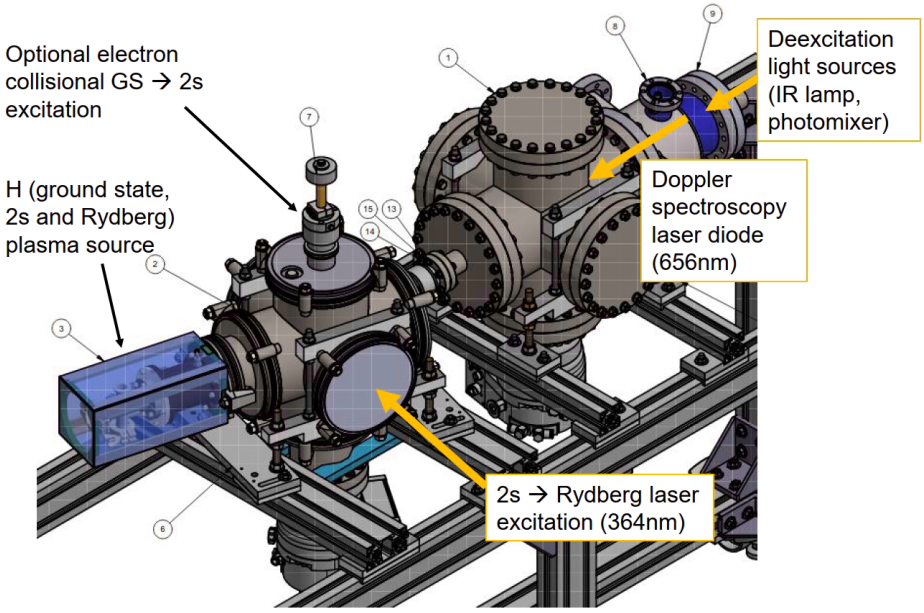

Figure 49 – Technical drawing of the hydrogen deexcitation set-up. The angle between the two chambers can be varied depending on the excitation option used (with or without electron collision excitation). The first chamber will be equipped with a cryo-cooler (not shown here) to minimize the effect of blackbody radiation. Beam diagnostics (Doppler spectroscopy and MCP) as well as the deexcitation devices will be installed in the second chamber.

the foreseen timeline for the deexcitation activities.

9.2 Progress at the hydrogen HFS-experiment

The hydrogen beam set-up is a complete Rabi experiment, where the spectroscopy components and methods for $\overline{\mathrm{H}}$ can be tested. In Fig. 50 a sketch illustrates the essential components above a photograph showing the current status.

After working on several maintenance and upgrade tasks for both hardware and software in 2019 the operation of the set-up restarted in early 2020. Optimization of alignment and operation parameters led to useful rates of atomic hydrogen by early March. Unfortunately, the pandemic situation demanded a complete shutdown before actual experimental runs could be started. In the end the experimental program for 2020 had to be deferred to 2021.

The slow and step-wise reactivation in accordance with allowed presence on site has been accompanied with a few setbacks. In parallel to resolving those problems several further software improvements were performed during the time of reduced presence, which should allow a swift restart of the data taking with the hydrogen beam in 2021.

One issue has been a further deterioration of the coldhead, but this time troubleshooting and several cleaning procedures did not result in acceptable performance anymore. The replacement that could be obtained works reliably thus far, but it required a new set of adapters as it is a different make. A more time consuming task has been tracking down the source of contamination in the hydrogen supply. Originally the microwave driven dissociation plasma could be maintained within the pyrex glass tube for months without observing the deposition of significant amounts of contamination on the glass walls or the subsequent cold PTFE tubing. The purity of the supplied molecular hydrogen seems to have worsened gradually and finally reached a level which prevented

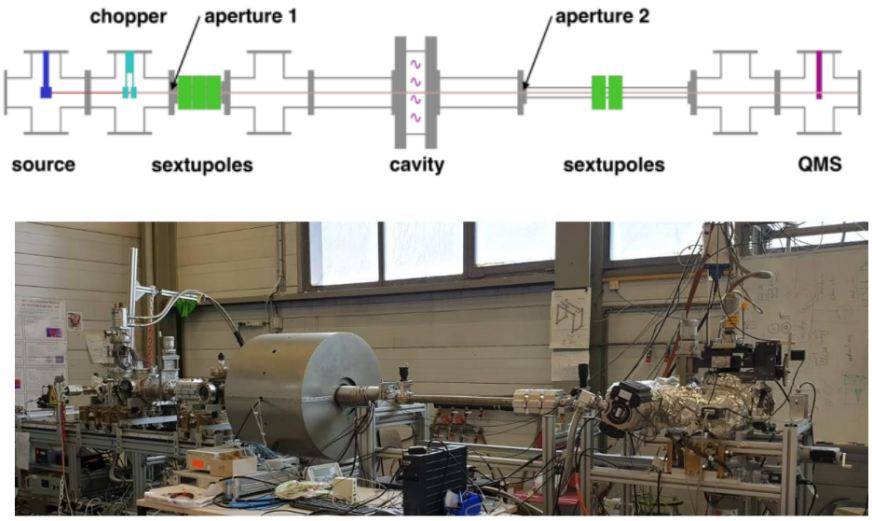

Figure 50 – Sketch and photograph of the hydrogen beam set-up. The atomic beam is formed on the left and gets modulated by a chopper and polarized by a set of permanent sextupole magnets. It then enters the interaction region consisting of a stripline cavity, field coils and a surrounding magnetic shielding. Subsequently another set of permanent sextupole magnets analyses the spin states before the beam is detected using a quadrupole mass spectrometer.

reliable operation of the atomic hydrogen source. Tracing the reason for the increasing level of contamination required more frequent intervention on the source and in this course we also had to deal with concomitant setbacks like glass breakage. The search focused on seals of the supply line and the role of ignition cabling and although no obvious single cause could be identified the situation had improved again by December. In view of the appearing year-end shut down it was decided to defer the complete restart of set-up and subsequent measurement campaigns to 2021.

The most relevant remaining measurement toward $\overline{\mathrm{H}}$ are variations of the hydrogen trajectories. The cavity has an open diameter of 100 mm to accept a large $\overline{\mathrm{H}}$-beam, while the H-beam is certainly less than 40 mm in size. This is a remaining caveat when drawing conclusions from the hydrogen measurements for $\overline{\mathrm{H}}$. Therefore, the cavity-assembly is mounted on a movable stage to allow for sending the beam through different sections of the large open diameter, thereby systematically verifying the level to which the trajectory-independence of the observed transition frequencies holds.

The present cavity-assembly is capable of accessing the σ and π transitions due to a 45° alignment between the static and oscillating magnetic fields. Having access to the π transition as well is advantageous from a practical and theoretical point of view. From a measurement of a single pair of a σ and π transition the zero-field HFS can be calculated. This approach is sensitive to SME coefficients unlike a zero-field extrapolation of many σ transitions obtained at various static fields [150] or taking the difference of the π_1 and π_2 transition [151]. Furthermore, acquisition of only two transitions is sufficient, which reduces the beamtime requirements. Therefore, the present cavity-assembly is going to be used for ASACUSA's Rabi-type $\overline{\mathrm{H}}$ spectroscopy as soon as sufficient rates of ground-state $\overline{\mathrm{H}}$ have been observed. The extensive progress with plasma manipulations in the Cusp trap as outlined in section 8.1.2 gives confidence that a demonstration could succeed during the 2021 run and that spectroscopy can be attempted the year after. Up to that point more measurements can be done with this cavity-assembly at the H-beam experiment. High statistic runs at various static field settings shall be taken distributed over a half-year period to test SME coefficients through annual or sidereal variations and gain more experience with the methods using

both transitions. The regime of very low static fields, where the two transition frequencies are separated by only a few line widths or less, shall be mapped in self-contained measurements. Currently, this regime should be avoided for precision measurements, as systematic shifts have been observed that first need to be fully understood. The development of fitting algorithms based on solving the optical Bloch equations of the complete 4-level (6-level for deuterium) system is ongoing.

The plans and foreseen timelines for experimental measurements with the hydrogen beam are listed in section 9.4. Although the trajectory variation studies are of most direct relevance for $\overline{\mathrm{H}}$ spectroscopy the first campaign will be devoted to precision experiments as here different measurement sets have to be taken at least half a year apart. The operation of the hydrogen HFS experiment as spatially and temporally well correlated reference for $\overline{\mathrm{H}}$ spectroscopy is rather expected for 2022.

9.3 Progress at the deuterium HFS-experiments and Ramsey spectroscopy

The first plan, as presented in the proposal for the ELENA era [108] had been a Ramsey device capable of addressing all hyperfine transitions in hydrogen and deuterium. The latter isotope is of interest since in comparison to hydrogen the proton carries a significantly larger momentum in deuterium, which results into an increased sensitivity to certain coefficients of the SME by 9 to 18 orders of magnitude [152]. Note, that there are now two σ transitions in deuterium and those feature a first order Zeeman shift at zero-field and also potential shifts associated to SME-coefficients [152]. As the deuteron is a spin 1 particle there are six deuterium hyperfine levels [153] in contrast to the four in hydrogen with a proton as a half-spin nucleus.

A versatile Ramsey apparatus requires two separate interaction regions (method of two separated oscillatory fields), where microwaves around 1.42 GHz and 330 MHz for H and D respectively can be applied parallel or orthogonal to the static guiding field. An application called HyDRA (Hydrogen Deuterium Ramsey Apparatus) had been submitted to the innovation funds of the Austrian Academy of Sciences in May 2019 to finance this device. Despite excellent reviews the application got transferred to a different grant for visionary infrastructure with a cut on the proposed budget. As a result we decided to split the scope of the HyDRA project into: (i) a quickly realizable and affordable set-up capable of Rabi spectroscopy on the σ transitions of deuterium, where the applicability to antimatter is not relevant and (ii) a medium-term project on a Ramsey apparatus for 1.42 GHz, which shall be tested with hydrogen and will have a sufficiently large acceptance to be installed at ASACUSA's $\overline{\mathrm{H}}$ beam in run period 4.

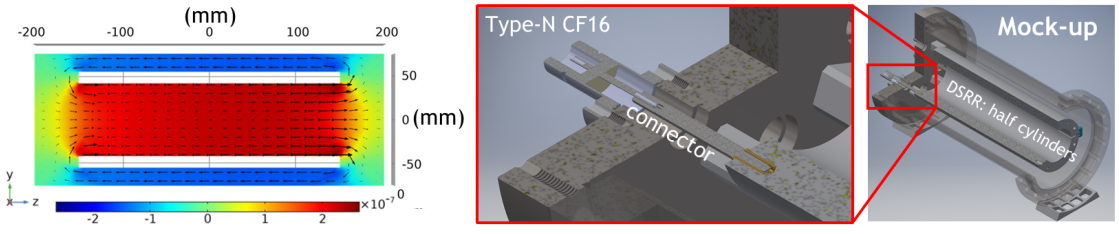

Figure 51 – COMSOL simulations of the oscillating magnetic field (left) and rendering of the DSRR as will be used in the mock-up. The half cylinders have inner and outer diameters of 62 mm and 98 mm and a length of 290 mm. They are housed in a DN150CF pipe. Microwaves will be fed through axial ports as shown in the close-up.

In the deuterium-Rabi experiment the microwave device to provide uniform oscillating fields at around 330 MHz will be a ring resonator. Similar geometries using a single slit are of wide use, however, we are testing a special version with two gaps in order to obtain two separated elements with the shape of an annular half cylinder. This way also electrical fields can be produced between

the two parts, which shall be used in an absolute field calibration based on the electron cyclotron resonance. We refer to this device as double split-ring resonator (DSRR). The resulting field shape has similarities to the field of a solenoid. In Fig. 51 left the expected field as obtained from COMSOL simulations is shown. In order to gain experience with this type of structure a mock-up is currently constructed at SMI in Vienna with the guidance of two microwave experts from CERN, Dr. F. Caspers and Dr. M. Wendt. A CAD image of the test set-up is shown on the right of Fig. 51. Based on the results from the mock-up a final, vacuum-compatible version will be designed with coils and magnetic shielding to provide a sufficiently uniform guiding field. The foreseen timelines for the development of the deuterium-Rabi apparatus and experimental measurements are listed in the next section.

9.4 Timeline for the hydrogen and deuterium experiments in 2021

Fig. 52 shows the foreseen schedule for the activities related to hydrogen and deuterium.

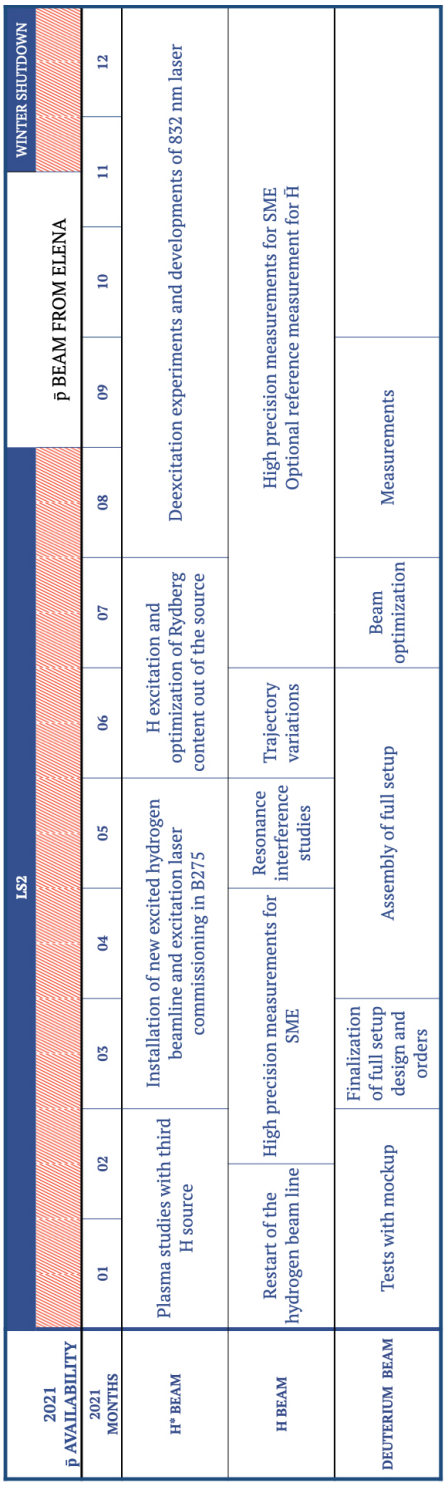

Figure 52 – Foreseen 2021 schedule for the hydrogen and deuterium activities (subject to change depending on the evolution of policies related to the pandemic).

10 Fragmentation studies of antiproton-nucleus annihilation at rest

The main goal of these studies is to validate the different descriptions of the $\overline{\text{p}}$ annihilation at rest in the Geant4 models [154, 155] and FLUKA [156] using very low energy (<1 keV), slow extracted antiprotons. These Monte Carlo simulations are used for every detector optimization and efficiency assessment in the AD experiments. Moreover, the accuracy of the reconstruction algorithms for data analysis is evaluated with simulated annihilation data [157–160].

The measurements were performed using three different target materials: carbon, molybdenum and gold with 99,9% purity. The charged annihilation products were detected with two detectors: minimum ionizing particles (MIPs), in this case pions, and heavily ionizing particles (HIPs), i.e. protons, alphas, etc. with a quad array of Timepix3 [161] placed 1 cm away from the target foil, and MIPs with a hodoscope detector around the target [158]. Details about the experimental set-up and data taking can be found in [113] and [162]. We study the prong multiplicities as detected by the two detectors, and the energy deposit of those recorded by Timepix3.

10.1 Preliminary results

The analysis was performed separately on the data recorded with each detector, but always for the same annihilation events matching the triggers issued by the hodoscope, leading to a total of ∼100,000 events per target foil. A typical signal from a single antiproton annihilation recorded with the Timepix3, containing clusters produced by pions and heavy fragments can be found in [162]. The Timepix3 allows for good discrimination between the emerging pions and nuclear fragments (e.g. p, d, t, α, ^{3}He etc.), based on the energy deposited in the silicon sensor and the morphology of the cluster.

Namely, a pion is a MIP at ∼350 MeV, an energy which is very close to the average kinetic energy of the produced pions in the annihilation, while a proton is a MIP at ∼2,350 MeV, an energy higher than the total energy produced in the annihilation. Typical proton energies emerging from $\overline{\text{p}}$-nucleus annihilations are usually <300 MeV [163, 164], a region where the dE/dx for protons is much larger than that for MIPs. An additional constraint on the length of the MIP tracks arises from the maximum allowed incident angle for particles emerging from the target foil and hitting the Timepix3 (∼70° in our case). Heavier ions produce distinguishable clusters with a "core" part and a "skirt" (or halo) [165]. All of the above features enable the classification of the prongs in one of the two categories, MIPs and HIPs. Even though observed, gamma particles were excluded from the analysis, discriminating their clusters by the size (1-2 pixels for ∼99% of the clusters) and energy [166].

Geant4 simulations were performed including the full geometry of the experimental set-up and the two detectors. For direct comparison with the produced clusters in the pixelated Timepix3, the raw energy depositions were processed (or digitized) to simulate the detector response in a collaborative effort with the developers of AllPix^2 [167], who created a dedicated module for our application in the newest version of the framework. A threshold of 1000 electrons on the signal (or 3.6 keV of deposited energy) was set in the Timepix3 during data taking, and also in the digitization of the simulations.

However, some of the effects that arise due to the large energy deposits from the heavily ionizing particles, such as the halo, the plasma effect [165] or the volcano effect and saturation [168] are not simulated in this detector response model, so the results on the energy deposits are compared both before and after the digitization. The deposited energy in the "raw" simulations is simply the sum of all the steps produced by Geant4, whereas the same clustering algorithm is applied to

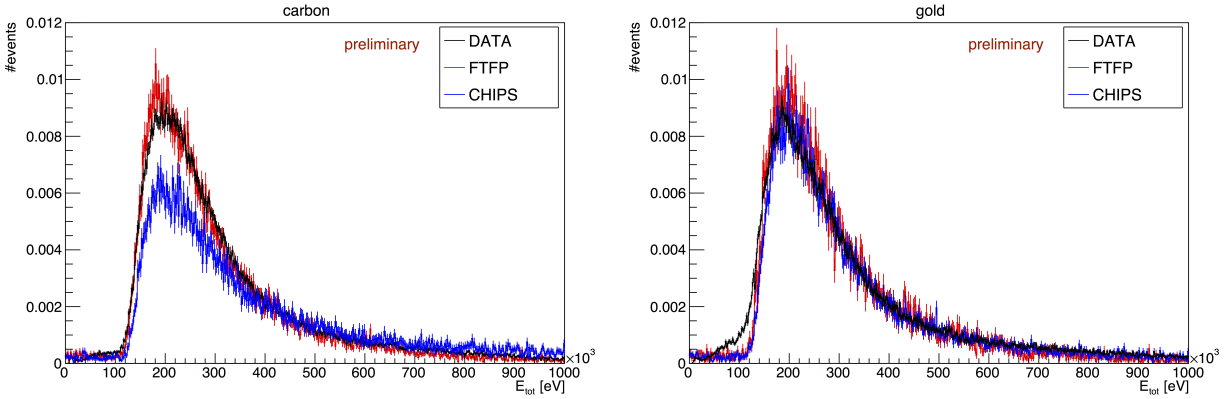

Figure 53 – Distribution of energy deposits for MIPs produced in $\overline{\mathrm{p}}$ annihilation in carbon (left) and in gold (right), recorded with Timepix3, before digitization.

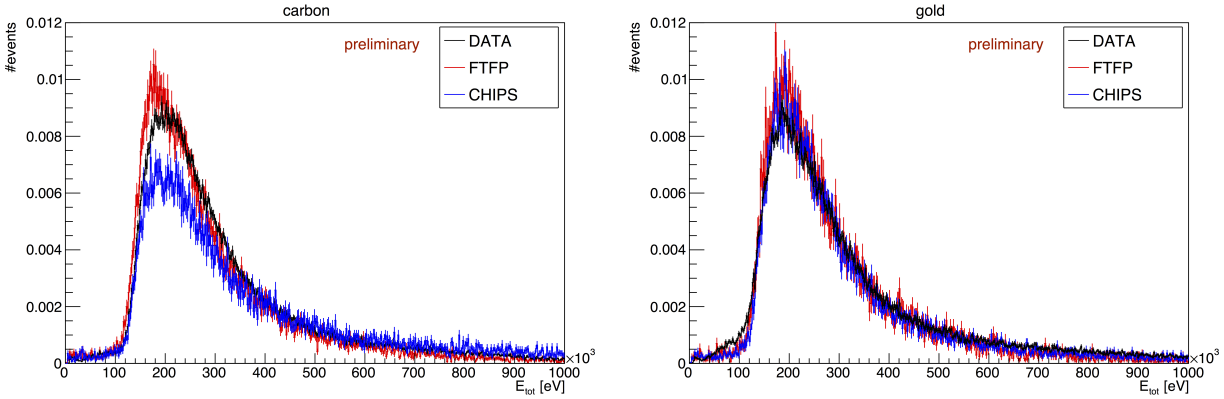

Figure 54 – The same energy distribution as in figure 53, after digitization.

the clusters both in the data and in the digitized simulations. The FLUKA simulations are still in progress.

Figure 53 shows the distributions of the energy deposited by individual MIPs (pions) in $\overline{\mathrm{p}}$+^{12}C and in $\overline{\mathrm{p}}$+^{197}Au (the only stable isotope for gold) annihilation at rest, measured with Timepix3 and compared with the two Geant4 models. In both cases there is a very good agreement between data and the Monte Carlo simulations, with CHIPS agreeing somewhat less in the case of carbon. The same distributions are showed after the digitization with AllPix^2 and the most probable value in both cases is $\sim$180 keV.

If we assume approximately uniform dE/dx over the silicon sensor and consider the minimum track length of 500 μm, this value would correspond to pions with energy of $\sim$450 MeV/c. In reality, most of the tracks are of course longer than the detector thickness, so analysis on 3D reconstruction of the tracks (using the Time-of-Arrival information from Timepix3) [169] to reveal their true length are ongoing.

The pion tracking algorithm applied on the hodoscope data is able to identify track candidates from the combination of all hit coordinates, fitting all possible track combinations, retaining the ones with the best fits and calculating the coordinates of the annihilation vertices [170]. Figure 55 shows the number of tracks (which corresponds to the number of charged pions) per annihilation for different target foils. For carbon, FTFP underestimates the measured number of pions by 5.7%,

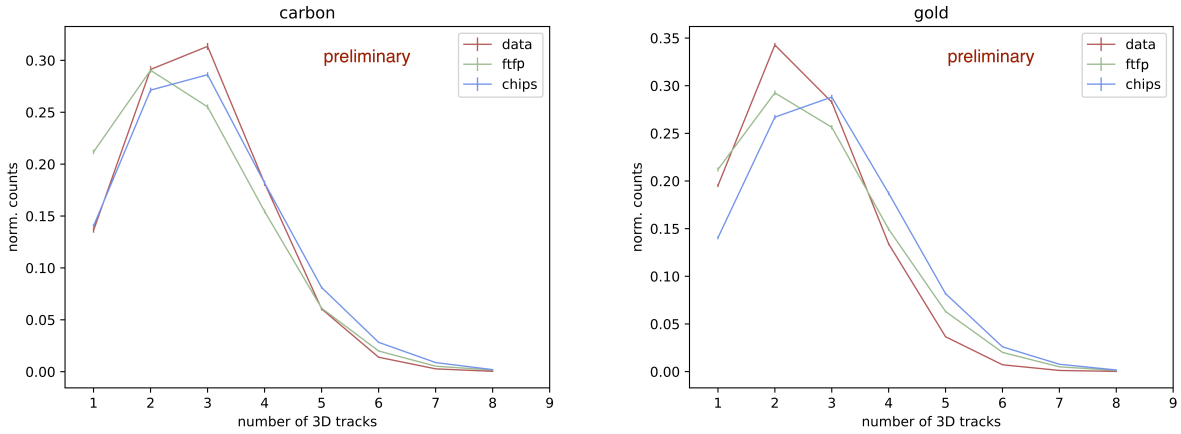

Figure 55 – Pion multiplicity distributions for $\overline{\mathrm{p}}$ annihilations at rest in C and Au as recorded by the hodoscope and comparison with the Geant4 models (CHIPS and FTFP).

while CHIPS overestimates it by 3.8%. For gold, the measured value is overestimated by FTFP by 5%, while CHIPS predicts 13.8% more pions than the average measured. The measurements are in agreement with [171], where starting from a nucleus mass number A = 2, the multiplicity decreases quickly as A increases for A $<$ 80 and is almost constant above. This is because the produced pions are absorbed with higher probability by nucleons close to the annihilation point, as the nucleons far from this point are in the shadow of the former ones and the flux of the pions decreases with the distance. Therefore, the addition of a nucleon to a big nucleus increases the absorption only negligibly.

References

[1] V. Chohan *et al.*, "Extra Low ENergy Antiproton ring (ELENA) and its transfer lines, design report," CERN-2014-002 (CERN, Geneva), 2014.

[2] M. Hori and V. I. Korobov, *Phys. Rev. A*, vol. 81, p. 062508, 2010.

[3] M. Hori *et al.*, *Nature*, vol. 475, p. 484, 2011.

[4] V. I. Korobov, L. Hilico, and J.-P. Karr, *Phys. Rev. Lett.*, vol. 112, p. 103003, 2014.

[5] V. I. Korobov, L. Hilico, and J. -P. Karr, *Phys. Rev. A*, vol. 89, p. 032511, 2014.

[6] M.-H. Hu *et al.*, *Chem. Phys. Lett.*, vol. 654, p. 114, 2016.

[7] F. Ficek *et al.*, *Phys. Rev. Lett.*, vol. 120, p. 183002, 2018.

[8] D. Baye, J. Dohet-Eraly, and P. Schoofs, *Phys. Rev. A*, vol. 99, p. 022508, 2019.

[9] T. P. Grozdanov and E. A. Solov'ev, *Eur. Phys. J. D*, vol. 74, no. 3, p. 50, 2020.

[10] Z.-D. Bai, Z.-X. Zhong, Z.-C. Yan, and T.-Y. Shi, "Complex coordinate rotation method based on gradient optimization," *Chin. Phys. B*, 2021.

[11] A. Bibikov, G. Y. Korenman, and S. Yudin, *Moscow University Physics Bulletin*, vol. 75, no. 3, p. 213, 2020.

[12] G. Ya. Korenman and S. N. Yudin, "Neutralization of excited antiprotonic helium ion in collisions with helium atoms," *Eur. Phys. J. D*, 2021.

[13] S. Friedreich *et al.*, *Phys. Lett. B*, vol. 700, p. 1, 2011.

[14] S. Friedreich *et al.*, *J. Phys. B*, vol. 46, p. 125003, 2013.

[15] T. Kobayashi *et al.*, *J. Phys. B*, vol. 46, p. 245004, 2013.

[16] M. Hori *et al.*, *Science*, vol. 354, p. 610, 2016.

[17] M. Hori *et al.*, *Phys. Rev. Lett.*, vol. 96, p. 243401, 2006.

[18] S. Alighanbari, G. S. Giri, F. L. Constantin, V. I. Korobov, and S. Schiller, *Nature*, vol. 581, p. 152, 2020.

[19] S. Patra *et al.*, *Science*, vol. 369, no. 6508, p. 1238, 2020.

[20] V. I. Korobov, J.-P. Karr, M. Haidar, and Z.-X. Zhong, *Phys. Rev. A*, vol. 102, no. 2, p. 022804, 2020.

[21] M. Hori and A. Dax, *Opt. Lett.*, vol. 34, p. 1273, 2009.

[22] V. Sonnenschein *et al.*, *Laser Phys.*, vol. 27, no. 8, p. 085701, 2017.

[23] G. Gabrielse *et al.*, *Opt. Lett.*, vol. 43, no. 12, p. 2905, 2018.

[24] P. Lottigier, A. Jucha, L. Cabaret, C. Blondel, and C. Drag, *Appl. Phys. B*, vol. 125, no. 1, p. 14, 2019.

[25] J. Hussels, C. Cheng, E. Salumbides, and W. Ubachs, *Opt. Lett.*, vol. 45, no. 21, p. 5909, 2020.

[26] S. Fu, X. Zhu, J. Wang, J. Zong, M. Li, A. Chavez-Pirson, R. A. Norwood, and N. Peyghambarian, *IEEE Photonics Technology Letters*, vol. 32, no. 18, p. 1179, 2020.

[27] M. Hori, *Science*, vol. 369, no. 6508, p. 1160, 2020.

[28] S. Sturm *et al.*, *Nature*, vol. 506, p. 467, 2014.

[29] F. Heiße *et al.*, *Phys. Rev. Lett.*, vol. 119, p. 033001, 2017.

[30] S. Rau *et al.*, *Nature*, vol. 585, p. 43, 2020.

[31] D. J. Fink and E. G. Myers, *Phys. Rev. Lett.*, vol. 124, no. 1, p. 013001, 2020.

[32] R. Pohl *et al.*, *Science*, vol. 353, no. 6300, p. 669, 2016.

[33] H. Fleurbaey *et al.*, *Phys. Rev. Lett.*, vol. 120, p. 183001, 2018.

[34] W. Xiong *et al.*, *Nature*, vol. 575, p. 147, 2019.

[35] N. Bezginov *et al.*, *Science*, vol. 365, no. 6457, p. 1007, 2019.

[36] A. Grinin *et al.*, *Science*, vol. 370, no. 6520, p. 1061, 2020.

[37] J. DiSciacca *et al.*, *Phys. Rev. Lett.*, vol. 110, no. 13, p. 130801, 2013.

[38] S. Ulmer *et al.*, *Nature*, vol. 524, p. 196, 2015.

[39] M. Ahmadi *et al.*, *Nature*, vol. 557, p. 71, 2018.

[40] R. S. Brusa *et al.*, "The AEgIS experiment at CERN: measuring antihydrogen free-fall in earth's gravitational field to test WEP with antimatter," in *J. Phys.: Conference Series*, vol. 791, no. 1. IOP Publishing, 2017, p. 012014.

[41] D. P. Van Der Werf and GBAR collaboration, "The GBAR experiment," in *International Journal of Modern Physics: Conference Series*, vol. 30. World Scientific, 2014, p. 1460263.

[42] M. Hori and J. Walz, *Prog. Part. Nucl. Phys.*, vol. 72, p. 206, 2013.

[43] E. J. Salumbides, W. Ubachs, and V. I. Korobov, *J. Mol. Spectrosc.*, vol. 300, p. 65, 2014.

[44] J. Murata and S. Tanaka, *Class Quantum Gravity*, vol. 32, p. 033001, 2015.

[45] M. S. Safronova *et al.*, *Rev. Mod. Phys.*, vol. 90, p. 025008, 2018.

[46] A. S. Lemos, G. C. Luna, E. Maciel, and F. Dahia, *Class. Quantum Gravity*, vol. 36, p. 245021, 2019.

[47] J. Ding *et al.*, *Phys. Rev. Lett.*, vol. 124, no. 16, p. 161801, 2020.

[48] Y. J. Kim, P.-H. Chu, and I. Savukov, *Phys. Rev. Lett.*, vol. 121, p. 091802, 2018.

[49] P. Fadeev *et al.*, *Phys. Rev. A*, vol. 99, no. 2, p. 022113, 2019.

[50] M. Hori *et al.*, *Phys. Rev. Lett.*, vol. 87, p. 093401, 2001.

[51] H. Yamaguchi *et al.*, *Phys. Rev. A*, vol. 66, p. 022504, 2002.

[52] M. Hori *et al.*, *Phys. Rev. Lett.*, vol. 89, p. 093401, 2002.

[53] H. Yamaguchi *et al,*, *Phys. Rev. A*, vol. 70, p. 012501, 2004.

[54] M. Hori *et al.*, *Phys. Rev. A*, vol. 70, p. 012504, 2004.

[55] A. Adamczak and D. Bakalov, *Phys. Rev. A*, vol. 88, p. 042505, 2013.

[56] A. Adamczak and D. Bakalov, *Phys. Rev. A*, vol. 90, p. 054501, 2014.

[57] K. Sakimoto, *Phys. Rev. A*, vol. 91, p. 042502, 2015.

[58] V. I. Korobov, Z.-X. Zhong, and Q.-L. Tian, *Phys. Rev. A*, vol. 92, p. 052517, 2015.

[59] J. G. Fetkovich and E. G. Pewitt, *Phys. Rev. Lett.*, vol. 11, p. 290, 1963.

[60] M. M. Block *et al.*, *Phys. Rev. Lett.*, vol. 11, p. 301, 1963.

[61] M. M. Block, J. B. Kopelman, and C. R. Sun, *Phys. Rev.*, vol. 140, p. B143, 1965.

[62] G. T. Condo, *Phys. Lett.*, vol. 9, p. 65, 1964.

[63] J. E. Russell, *Phys. Rev. Lett.*, vol. 23, p. 63, 1969.

[64] M. Hori, A. Sótér, and V. I. Korobov, *Phys. Rev. A*, vol. 89, p. 042515, 2014.

[65] V. I. Korobov, A. K. Bekbaev, D. T. Aznabayev, and S. A. Zhaugasheva, *J. Phys. B*, vol. 48, p. 245006, 2015.

[66] B. Obreshkov and D. Bakalov, *Phys. Rev. A*, vol. 93, p. 062505, 2016.

[67] M. Hori, H. Aghai-Khozani, A. Sótér, A. Dax, and D. Barna, *Nature*, vol. 581, p. 37, 2020.

[68] J. Koch and F. Scheck, *Nucl. Phys. A*, vol. 340, no. 2, p. 221, 1980.

[69] M. Trassinelli and P. Indelicato, *Phys. Rev. A*, vol. 76, no. 1, p. 012510, 2007.

[70] S. Lenz *et al.*, *Phys. Lett. B*, vol. 416, p. 50, 1998.

[71] M. Trassinelli *et al.*, *Phys. Lett. B*, vol. 759, p. 583, 2016.

[72] M. Daum, R. Frosch, and P.-R. Kettle, *Phys. Lett. B*, vol. 796, p. 11, 2019.

[73] K. Assamagan *et al.*, *Phys. Rev. D*, vol. 53, p. 6065, 1996.

[74] O. A. Zaĭmidoroga, R. M. Sulyaev, and V. M. Tsupko-Sitnikov, *Sov. Phys. JETP*, vol. 25, p. 63, 1967.

[75] S. N. Nakamura *et al.*, *Phys. Rev. A*, vol. 45, p. 6202, 1992.

[76] H. L. Anderson, J. Marshall, L. Kornblith Jr, L. Schwarcz, and R. Miller, *Rev. Sci. Instrum.*, vol. 23, no. 12, p. 707, 1952.

[77] J. Ashkin, J. P. Blaser, F. Feiner, J. G. Gorman, and M. O. Stern, *Phys. Rev.*, vol. 96, no. 4, p. 1104, 1954.

[78] R. J. Walker *et al.*, *Rev. Sci. Instrum.*, vol. 39, no. 10, p. 1407, 1968.

[79] J. E. Russell, *Phys. Rev.*, vol. A1, p. 721, 1970.

[80] G. Backenstoss *et al.*, *Nucl. Phys.*, vol. A232, p. 519, 1974.

[81] R. Landua and E. Klempt, *Phys. Rev. Lett.*, vol. 48, p. 1722, 1982.

[82] D. Gotta, *Prog. Part. Nucl. Phys.*, vol. 52, p. 133, 2004.

[83] M. Hori *et al.*, *Phys. Rev. Lett.*, vol. 94, p. 063401, 2005.

[84] R. Abela, F. Foroughi, and D. Renker, *Z. Phys. C*, vol. 56, p. S240, 1992.

[85] E. Daum *et al.*, *Nucl. Phys. A*, vol. 589, p. 553, 1995.

[86] C. Cernigoi *et al.*, *Nucl. Phys.*, vol. A352, p. 343, 1981.

[87] A. Sótér *et al.*, *Rev. Sci. Instrum.*, vol. 85, p. 023302, 2014.

[88] K. Todoroki *et al.*, *Nucl. Instrum. Meth. A*, vol. 835, p. 110, 2016.

[89] Y. Murakami, H. Aghai-Khozani, and M. Hori, *Nucl. Instrum. Meth. A*, vol. 933, p. 75, 2019.

[90] S. Ritt, R. Dinapoli, and U. Hartmann, *Nucl. Instrum. and Meth. A*, vol. 623, no. 1, p. 486, 2010.

[91] H. Friederich *et al.*, *IEEE Trans. Nucl. Sci.*, vol. 58, no. 4, p. 1652, 2011.

[92] H. Aghai-Khozani *et al.*, *Eur. Phys. J. Plus*, vol. 127, p. 125, 2012.

[93] A. Bianconi *et al.*, *Phys. Lett. B*, vol. 704, p. 461, 2011.

[94] H. Aghai-Khozani *et al.*, *Nucl. Phys. A*, vol. 970, p. 366, 2018.

[95] M. Hori *et al.*, *Phys. Rev. Lett.*, vol. 91, p. 123401, 2003.

[96] D. Bakalov, B. Jeziorski, T. Korona, K. Szalewicz, and E. Tchoukova, *Phys. Rev. Lett.*, vol. 84, p. 2350, 2000.

[97] R. Pohl *et al.*, *Nature*, vol. 466, p. 213, 2010.

[98] J.-P. Karr, M. Haidar, L. Hilico, Z.-X. Zhong, and V. I. Korobov, *Phys. Rev. A*, vol. 102, no. 5, p. 052827, 2020.

[99] M. Corradini *et al.*, *Nucl. Instrum. Meth. A*, vol. 711, p. 12, 2013.

[100] M. Hori, K. Yamashita, R. S. Hayano, and T. Yamazaki, *Nucl. Instrum. Methods in Phys. Research A*, vol. 496, p. 102, 2003.

[101] V. I. Korobov, *Phys. Rev. A*, vol. 89, p. 014501, 2014.

[102] V. I. Korobov, L. Hilico, and J.-P. Karr, *Hyperfine Int.*, vol. 233, p. 75, 2015.

[103] M. Hori, *Rev. Sci. Instrum.*, vol. 76, p. 113303, 2005.

[104] M. Hori, *Nucl. Instrum. Meth. A*, vol. 522, no. 3, p. 420, 2004.

[105] A. Jallageas *et al.*, *Metrologia*, vol. 55, p. 366, 2018.

[106] C. Malbrunot, C. Amsler, S. Arguedas Cuendis, H. Breuker, P. Dupre, M. Fleck, H. Higaki, Y. Kanai, B. Kolbinger, N. Kuroda, M. Leali, V. Mäckel, V. Mascagna, O. Massiczek, Y. Matsuda, Y. Nagata, M. C. Simon, H. Spitzer, M. Tajima, S. Ulmer, L. Venturelli, E. Widmann, M. Wiesinger, Y. Yamazaki, and J. Zmeskal, "The asacusa antihydrogen and hydrogen program: results and prospects," *Philosophical Transactions of the Royal Society of London A: Mathematical, Physical and Engineering Sciences*, vol. 376, no. 2116, p. 20170273, 2018. [Online]. Available: http://rsta.royalsocietypublishing.org/content/376/2116/20170273

[107] E. Widmann *et al.*, "Hyperfine spectroscopy of hydrogen and antihydrogen in ASACUSA," *Hyperfine Interact*, vol. 240, p. 5, 2019. [Online]. Available: https://doi.org/10.1007/s10751-018-1536-9

[108] C. Amsler *et al.*, "ASACUSA proposal for ELENA," CERN-SPSC-2019-035 / SPSC-P-307-ADD-2. [Online]. Available: https://cds.cern.ch/record/2691506

[109] A. Mohri and Y. Yamazaki, "A possible new scheme to synthesize antihydrogen and to prepare a polarised antihydrogen beam," *Europhysics Letters*, vol. 63, p. 207, 2003.

[110] Y. Nagata, N. Kuroda, P. Dupre, B. Radics, M. Tajima, A. A. Capon, M. Diermaier, C. Kaga, B. Kolbinger, M. Leali, E. L. Rizzini, C. Malbrunot, V. Mascagna, O. Massiczek, T. Matsudate, C. Sauerzopf, M. C. Simon, K. Suzuki, J. Zmeskal, H. Breuker, H. Higaki, Y. Kanai, Y. Matsuda, S. Ulmer, L. Venturelli, E. Widmann, and Y. Yamazaki, "Progress of antihydrogen beam production using a double cusp trap," *JPS Conf. Proc.*, vol. 18, p. 011007, 2017.

[111] A. Mohri, T. Yuyama, Y. Kiwamoto, Y. Yamazawa, and T. Michishita, *Jap. J. Appl. Phys.*, vol. 37, p. L1553, 1998, a. Mohri, private communication.

[112] C. Malbrunot, M. Diermaier, M. Simon, C. Amsler, S. A. Cuendis, H. Breuker, C. Evans, M. Fleck, B. Kolbinger, A. Lanz, M. Leali, V. Maeckel, V. Mascagna, O. Massiczek, Y. Matsuda, Y. Nagata, C. Sauerzopf, L. Venturelli, E. Widmann, M. Wiesinger, Y. Yamazaki, and J. Zmeskal, "A hydrogen beam to characterize the asacusa antihydrogen hyperfine spectrometer," *Nuclear Instruments and Methods in Physics Research Section A: Accelerators, Spectrometers, Detectors and Associated Equipment*, vol. 935, pp. 110 – 120, 2019. [Online]. Available: http://www.sciencedirect.com/science/article/pii/S0168900219305315

[113] E. Widmann and M. Hori, "ASACUSA STATUS REPORT Recent progress and plans for LS2," CERN, Geneva, Tech. Rep. CERN-SPSC-2019-006. SPSC-SR-245, Jan 2019. [Online]. Available: https://cds.cern.ch/record/2654222

[114] B. Kolbinger, C. Amsler, S. A. Cuendis, H. Breuker, A. Capon, G. Costantini, P. Dupré, M. Fleck, A. Gligorova, H. Higaki, Y. Kanai, V. Kletzl, N. Kuroda, A. Lanz, M. Leali, V. Mäckel, C. Malbrunot, V. Mascagna, O. Massiczek, Y. Matsuda, D. J. Murtagh, Y. Nagata, A. Nanda, L. Nowak, B. Radics, C. Sauerzopf, M. C. Simon, M. Tajima, H. A. Torii, U. Uggerhøj, S. Ulmer, L. Venturelli, A. Weiser, M. Wiesinger, E. Widmann, T. Wolz, Y. Yamazaki, and J. Zmeskal, "Measurement of the principal quantum number distribution in a beam of antihydrogen atoms," arxiv:2008.04246, EPJ D, in print, 2020.

[115] E. Hunter, "Cavity and microwave experiments on electron plasma," Ph.D. dissertation, UC Berkeley, 2019.

[116] M. Tinkle, R. Greaves, C. Surko, R. Spencer, and G. Mason, "Low-order modes as diagnostics of spheroidal non-neutral plasmas," *Physical review letters*, vol. 72, no. 3, p. 352, 1994.

[117] F. Anderegg, N. Shiga, D. Dubin, C. Driscoll, and R. Gould, "Thermally excited trivelpiece–gould modes as a pure electron plasma temperature diagnostic," *Physics of Plasmas*, vol. 10, no. 5, pp. 1556–1562, 2003.

[118] B. R. Beck, "Measurement of the magnetic and temperature dependence of the electron-electron anisotropic temperature relaxation rate," Ph.D. dissertation, University of California, San Diego, Department of Physics, 1990.

[119] D. Eggleston, C. Driscoll, B. Beck, A. Hyatt, and J. Malmberg, "Parallel energy analyzer for pure electron plasma devices," *Physics of Fluids B: Plasma Physics*, vol. 4, no. 10, pp. 3432–3439, 1992.

[120] E. Hunter, J. Fajans, N. Lewis, A. Povilus, C. Sierra, C. So, and D. Zimmer, "Plasma temperature measurement with a silicon photomultiplier (sipm)," *Review of Scientific Instruments*, vol. 91, no. 10, 2020.

[121] J. Danielson, D. Dubin, R. Greaves, and C. Surko, "Plasma and trap-based techniques for science with positrons," *Reviews of Modern Physics*, vol. 87, no. 1, p. 247, 2015.

[122] M. Diermaier, C. Jepsen, B. Kolbinger, C. Malbrunot, O. Massiczek, C. Sauerzopf, M. Simon, J. Zmeskal, and E. Widmann, "In-beam measurement of the hydrogen hyperfine splitting and prospects for antihydrogen spectroscopy," *Nature communications*, vol. 8, no. 1, pp. 1–9, 2017.

[123] M. Ahmadi, B. Alves, C. Baker, W. Bertsche, E. Butler, A. Capra, C. Carruth, C. Cesar, M. Charlton, S. Cohen *et al.*, "Antihydrogen accumulation for fundamental symmetry tests," *Nature communications*, vol. 8, no. 1, pp. 1–6, 2017.

[124] M. Ahmadi, B. Alves, C. Baker, W. Bertsche, A. Capra, C. Carruth, C. Cesar, M. Charlton, S. Cohen, R. Collister *et al.*, "Enhanced control and reproducibility of non-neutral plasmas," *Physical review letters*, vol. 120, no. 2, p. 025001, 2018.

[125] J. Danielson, C. Surko, and T. O'Neil, "High-density fixed point for radially compressed single-component plasmas," *Physical review letters*, vol. 99, no. 13, p. 135005, 2007.

[126] G. Andresen, M. Ashkezari, M. Baquero-Ruiz, W. Bertsche, P. D. Bowe, E. Butler, C. Cesar, S. Chapman, M. Charlton, J. Fajans *et al.*, "Evaporative cooling of antiprotons to cryogenic temperatures," *Physical review letters*, vol. 105, no. 1, p. 013003, 2010.

[127] A. Chaney and R. Sundararajan, "Simple mosfet-based high-voltage nanosecond pulse circuit," *Plasma Science, IEEE Transactions on*, vol. 32, pp. 1919 – 1924, 11 2004.

[128] C. Amole, M. Ashkezari, M. Baquero-Ruiz, W. Bertsche, E. Butler, A. Capra, C. Cesar, S. Chapman, M. Charlton, S. Eriksson *et al.*, "Autoresonant-spectrometric determination of the residual gas composition in the alpha experiment apparatus," *Review of Scientific Instruments*, vol. 84, no. 6, p. 065110, 2013.

[129] P. Atkins and J. De Paula, *Physical chemistry for the life sciences.* Oxford University Press, USA, 2011.

[130] M. Hori and E. Widmann, "ASACUSA status report - recent progress and plans for 2020," CERN, Geneva, Tech. Rep. CERN-SPSC-2020-001. SPSC-SR-264, Jan 2020. [Online]. Available: https://cds.cern.ch/record/2706194

[131] A. Weiser, "A low energy proton source for ASACUSA's matter studies," Dec 2020, presented 22 12 2020. [Online]. Available: https://cds.cern.ch/record/2748624

[132] N. Ekanayake, M. Nairat, B. Kaderiya, P. Feizollah, B. Jochim, T. Severt, B. Berry, K. R. Pandiri, K. D. Carnes, S. Pathak *et al.*, "Mechanisms and time-resolved dynamics for trihydrogen cation (H3+) formation from organic molecules in strong laser fields," *Scientific reports*, vol. 7, no. 1, pp. 1–12, 2017.

[133] Straub, Renault, Lindsay, J. Smith, and Stebbings, "Absolute partial cross sections for electron-impact ionization of H2, N2, and O2 from threshold to 1000 eV." *Physical review. A, Atomic, molecular, and optical physics*, vol. 54 3, pp. 2146–2153, 1996.

[134] F. Ames, G. Bollen, P. Delahaye, O. Forstner, G. Huber, O. Kester, K. Reisinger, and P. Schmidt, "Cooling of radioactive ions with the penning trap REXTRAP," *Nuclear Instruments and Methods in Physics Research Section A: Accelerators, Spectrometers, Detectors and Associated Equipment*, vol. 538, no. 1, pp. 17 – 32, 2005. [Online]. Available: http://www.sciencedirect.com/science/article/pii/S0168900204020169

[135] M. Shibata, A. Mohri, Y. Kanai, Y. Enomoto, and Y. Yamazaki, "Compact cryogenic system with mechanical cryocoolers for antihydrogen synthesis," *Review of Scientific Instruments*, vol. 79, no. 1, p. 015112, 2008.

[136] R. G. Greaves and J. Moxom, "Design and performance of a trap-based positron beam source," *AIP Conference Proceedings*, vol. 692, no. 1, pp. 140–148, 2003.

[137] S. L. Andersen, R. R. Johansen, J. B. Overgaard, J. K. Mortensen, K. K. Andersen, H. D. Thomsen, M. D. Lund, J. Chevallier, H. Knudsen, and U. I. Uggerhøj, "Positronium formation from porous silica in backscattering and transmission geometries," *The European Physical Journal D*, vol. 68, no. 5, p. 124, May 2014. [Online]. Available: https://doi.org/10.1140/epjd/e2014-40762-x

[138] N. Kuroda, H. A. Torii, Y. Nagata, M. Shibata, Y. Enomoto, H. Imao, Y. Kanai, M. Hori, H. Saitoh, H. Higaki, A. Mohri, K. Fujii, C. H. Kim, Y. Matsuda, K. Michishio, Y. Nagashima, M. Ohtsuka, K. Tanaka, and Y. Yamazaki, "Development of a monoenergetic ultraslow antiproton beam source for high-precision investigation," *Phys. Rev. ST Accel. Beams*, vol. 15, p. 024702, Feb 2012. [Online]. Available: https://link.aps.org/doi/10.1103/PhysRevSTAB.15.024702

[139] S. Möller, E. Uggerhøj, H. Bluhme, H. Knudsen, U. Mikkelsen, K. Paludan, and E. Morenzoni, "Direct measurements of the stopping power for antiprotons of light and heavy targets," *Phys. Rev. A*, vol. 56, no. 4, p. 2930, October 1997.

[140] S. Möller, A. Ceste, T. Ichioka, H. Knudsen, U. I. Uggerhøj, and H. Andersen, "Antiproton Stopping at Low Energies: Confirmation of Velocity-Proportional Stopping Power," *Phys. Rev. Lett.*, vol. 88, no. 19, p. 193201, May 2002.

[141] S. P. Møller, A. Csete, T. Ichioka, H. Knudsen, U. I. Uggerhøj, and H. H. Andersen, "Stopping power in insulators and metals without charge exchange," *Phys. Rev. Lett.*, vol. 93, p. 042502, Jul 2004. [Online]. Available: https://link.aps.org/doi/10.1103/PhysRevLett.93.042502

[142] S. P. Møller, A. Csete, T. Ichioka, H. Knudsen, H.-P. Kristiansen, U. I. Uggerhøj, H. H. Andersen, P. Sigmund, and A. Schinner, "Antiproton and proton energy loss straggling at kev energies," *The European Physical Journal D*, vol. 46, no. 1, pp. 89–92, 2008. [Online]. Available: https://doi.org/10.1140/epjd/e2007-00314-3

[143] K. Nordlund, D. Sundholm, P. Pyykkö, D. M. Zambrano, and F. Djurabekova, "Nuclear stopping power of antiprotons," *Phys. Rev. A*, vol. 96, p. 042717, Oct 2017. [Online]. Available: https://link.aps.org/doi/10.1103/PhysRevA.96.042717

[144] M. Corradini, M. Leali, E. Rizzini, V. Mascagna, M. Prest, E. Vallazza, and L. Venturelli, "Scintillating bar detector for antiproton annihilations measurements," *Hyperfine Interactions*, vol. 233, no. 1-3, pp. 53–58, 2015. [Online]. Available: https://link.springer.com/article/10.1007/s10751-015-1181-5

[145] T. Wolz, C. Malbrunot, M. Vieille-Grosjean, and D. Comparat, "Stimulated decay and formation of antihydrogen atoms," *Phys. Rev. A*, vol. 101, p. 043412, Apr 2020. [Online]. Available: https://link.aps.org/doi/10.1103/PhysRevA.101.043412

[146] R. Lundmark, C. Malbrunot, Y. Nagata, B. Radics, C. Sauerzopf, and E. Widmann, *J. Phys. B: At. Mol. Opt. Phys.*, vol. 48, no. 18, p. 184001, 2015.

[147] S. Jonsell and M. Charlton, "Formation of antihydrogen beams from positron antiproton interactions," *New Journal of Physics*, vol. 21, no. 7, p. 073020, Jul. 2019.

[148] M. Vieille-Grosjean, E. Dimova, Z. Mazzotta, D. Comparat, T. Wolz, and C. Malbrunot, "Induced THz transitions in Rydberg caesium atoms for application in antihydrogen experiments," arXiv:2101.01047, EPJ D, in print, 2020.

[149] D. Wünderlich, M. Giacomin, R. Ritz, and U. Fantz, "Yacora on the web: Online collisional radiative models for plasmas containing h, h2 or he," *Journal of Quantitative Spectroscopy and Radiative Transfer*, vol. 240, p. 106695, 2020. [Online]. Available: http://www.sciencedirect.com/science/article/pii/S0022407319305163

[150] M. Diermaier, C. B. Jepsen, B. Kolbinger, C. Malbrunot, O. Massiczek, C. Sauerzopf, M. C. Simon, J. Zmeskal, and E. Widmann, "In-beam measurement of the hydrogen hyperfine splitting and prospects for antihydrogen spectroscopy," *Nat Commun*, vol. 8, Jun. 2017.

[151] M. Ahmadi, B. X. R. Alves, C. J. Baker, W. Bertsche, E. Butler, A. Capra, C. Carruth, C. L. Cesar, M. Charlton, S. Cohen, R. Collister, S. Eriksson, A. Evans, N. Evetts, J. Fajans, T. Friesen, M. C. Fujiwara, D. R. Gill, A. Gutierrez, J. S. Hangst, W. N. Hardy, M. E. Hayden, C. A. Isaac, A. Ishida, M. A. Johnson, S. A. Jones, S. Jonsell, L. Kurchaninov, N. Madsen, M. Mathers, D. Maxwell, J. T. K. McKenna, S. Menary, J. M. Michan, T. Momose, J. J. Munich, P. Nolan, K. Olchanski, A. Olin, P. Pusa, C. O. Rasmussen, F. Robicheaux, R. L. Sacramento, M. Sameed, E. Sarid, D. M. Silveira, S. Stracka, G. Stutter, C. So, T. D. Tharp, J. E. Thompson, R. I. Thompson, D. P. van der Werf, and J. S. Wurtele, "Observation of the hyperfine spectrum of antihydrogen," *Nature*, vol. 548, p. 66, aug 2017. [Online]. Available: http://dx.doi.org/10.1038/nature23446

[152] V. A. Kostelecký and A. J. Vargas, *Phys. Rev. D*, vol. 92, no. 5, p. 056002, Sep. 2015.

[153] J. E. Nafe and E. B. Nelson, *Phys. Rev.*, vol. 73, p. 718, 1948.

[154] P. V. Degtyarenko, M. V. Kossov, and H.-P. Wellisch, "Chiral invariant phase space event generator," *The European Physical Journal A*, vol. 8, no. 2, pp. 217–222, Jul 2000. [Online]. Available: https://doi.org/10.1007/s100500070108

[155] A. Galoyan, A. Ribon, and V. Uzhinsky, "Dynamics of Anti-Proton–Protons and Anti-Proton–Nucleus Reactions," *Nucl. Theor.*, vol. 35, pp. 194–202, 2016.

[156] T. Böhlen, F. Cerutti, M. Chin, A. Fassò, A. Ferrari, P. Ortega, A. Mairani, P. Sala, G. Smirnov, and V. Vlachoudis, "The fluka code: Developments and challenges for high energy and medical applications," *Nuclear Data Sheets*, vol. 120, pp. 211 – 214, 2014. [Online]. Available: https://doi.org/10.1016/j.nds.2014.07.049

[157] G. Andresen, M. Ashkezari, W. Bertsche, P. Bowe, E. Butler, C. Cesar, S. Chapman, M. Charlton, A. Deller, S. Eriksson, J. Fajans, T. Friesen, M. Fujiwara, D. Gill, A. Gutierrez, J. Hangst, W. Hardy, M. Hayden, R. Hayano, A. Humphries, R. Hydomako, S. Jonsell, L. Jørgensen, L. Kurchaninov, N. Madsen, S. Menary, P. Nolan, K. Olchanski, A. Olin, A. Povilus, P. Pusa, E. Sarid, S. S. el Nasr], D. Silveira, C. So, J. Storey, R. Thompson, D. [van der Werf], and Y. Yamazaki, "Antihydrogen annihilation reconstruction with the alpha silicon detector," *Nucl. Instrum. Meth. A*, vol. 684, pp. 73 – 81, 2012. [Online]. Available: https://doi.org/10.1016/j.nima.2012.04.082

[158] C. Sauerzopf *et al.*, "Annihilation detector for an in-beam spectroscopy apparatus to measure the ground state hyperfine splitting of antihydrogen." [Online]. Available: https://doi.org/10.1016/j.nima.2016.06.023

[159] J. Storey *et al.*, "Particle tracking at 4K: The Fast Annihilation Cryogenic Tracking (FACT) detector for the AEgIS antimatter gravity experiment," *Nucl. Instrum. Meth. A*, vol. 732, pp. 437–441, 2013. [Online]. Available: https://doi.org/10.1016/j.nima.2013.05.130

[160] A. Capra *et al.*, "Design of a Radial TPC for Antihydrogen Gravity Measurement with ALPHA-g," *JPS Conf. Proc.*, vol. 18, p. 011015, 2017. [Online]. Available: https://doi.org/10.7566/JPSCP.18.011015

[161] T. Poikela, J. Plosila, T. Westerlund, M. Campbell, M. D. Gaspari, X. Llopart, V. Gromov, R. Kluit, M. van Beuzekom, F. Zappon, V. Zivkovic, C. Brezina, K. Desch, Y. Fu, and A. Kruth, "Timepix3: a 65k channel hybrid pixel readout chip with simultaneous ToA/ToT and sparse readout," *Journal of Instrumentation*, vol. 9, no. 05, p. C05013, 2014. [Online]. Available: https://doi.org/10.1088/1748-0221/9/05/C05013

[162] E. Widmann, "Asacusa status report recent progress and plans for 2018," CERN, Geneva, Tech. Rep. CERN-SPSC-2018-003. SPSC-SR-226, Jan 2018. [Online]. Available: http://cds.cern.ch/record/2300138

[163] P. Hofmann, F. Hartmann, H. Daniel, T. Von Egidy, W. Kanert, W. Markiel, H. Plendl, H. Machner, G. Riepe, D. Protić, K. Ziock, R. Marshall, and J. Reidy, "Charged-particle spectra from antiproton annihilation at rest in a = 12–238 nuclei," *Nuclear Physics A*, vol. 512, no. 4, pp. 669 – 683, 1990. [Online]. Available: https://doi.org/10.1016/0375-9474(90)90229-F

[164] M. Cahay, J. Cugnon, and J. Vandermeulen, "Low-energy antiproton annihilation in nuclei," *Nuclear Physics A*, vol. 393, no. 3, pp. 237 – 251, 1983. [Online]. Available: https://doi.org/10.1016/0375-9474(83)90141-0

[165] S. Hoang, R. Vilalta, L. Pinsky, M. Kroupa, N. Stoffle, and J. Idarraga, "Data analysis of tracks of heavy ion particles in timepix detector," *Journal of Physics: Conference Series*, vol. 523, p. 012026, jun 2014. [Online]. Available: https://doi.org/10.10882F1742-65962F5232F12F012026

[166] C. Granja, J. Jakubek, S. Polansky, V. Zach, P. Krist, D. Chvatil, J. Stursa, M. Sommer, O. Ploc, S. Kodaira, and M. Martisikova, "Resolving power of pixel detector timepix for wide-range electron, proton and ion detection," *Nucl. Instrum. Meth. A*, vol. 908, pp. 60 – 71, 2018. [Online]. Available: https://doi.org/10.1016/j.nima.2018.08.014

[167] S. Spannagel, K. Wolters, D. Hynds, N. Alipour Tehrani, M. Benoit, D. Dannheim, N. Gauvin, and A. N "Allpix2: A modular simulation framework for silicon detectors," *Nucl. Instrum. Meth. A*, vol. 901, pp. 164 – 172, 2018. [Online]. Available: https://doi.org/10.1016/j.nima.2018.06.020

[168] T. Campbell-Ricketts, M. Kroupa, and L. Pinsky, "Spectroscopy of high-energy ions with timepix3," *Journal of Instrumentation*, vol. 11, no. 11, pp. P11 007–P11 007, nov 2016. [Online]. Available: https://doi.org/10.10882F1748-02212F112F112Fp11007

[169] B. Bergmann, M. Pichotka, S. Pospisil, J. Vycpalek, P. Burian, P. Broulim, and J. Jakubek, "3d track reconstruction capability of a silicon hybrid active pixel detector," *The European Physical Journal C*, vol. 77, no. 6, p. 421, Jun 2017. [Online]. Available: https://doi.org/10.1140/epjc/s10052-017-4993-4

[170] B. Kolbinger, "Machine Learning for Antihydrogen Detection in ASACUSA," Ph.D. dissertation, 2018. [Online]. Available: http://cds.cern.ch/record/2670395

[171] G. Bendiscioli and D. Kharzeev, "Antinucleon-nucleon and antinucleon-nucleus interaction. a review of experimental data," *La Rivista Del Nuovo Cimento Series 3*, vol. 17, no. 6, pp. 1–142, 1994. [Online]. Available: http://dx.doi.org/10.1007/BF02724447